Fabrication of Two-Dimensional Graphene-Based Heterostructures for Photodetection Applications

Tongxin Chen

Supervised by Professor Jamie H. Warner

St. Cross College

Department of Materials

University of Oxford

Submitted in conformity with the requirements

for the degree of DPhil in Materials Science

Sept 2019

Declaration

The material contained within this thesis has not previously been submitted for a degree at the University of Oxford and ant other university. The research reported within this thesis has been conducted by the author unless indicated otherwise.

Copyright Notice

Abstract

Fabrication of Two-Dimensional Graphene-Based Heterostructures for Photodetection Applications

Tongxin Chen

Supervised by Professor Jamie H. Warner

The discovery of graphene has so far drawn significant attentions since 2004 when isolation of single layer graphene was first achieved. Over the past few years, the interest in graphene has also expanded into other two-dimensional (2D) materials, including transition metal dichalcogenides (TMDs), such as Molybdenum disulfide (MoS_2) and WS_2, metal chalcogenides, such as gallium sulfide (GaS), and heterostructures base on these materials. Numerous studies have been done on fabrication and characterization of 2D heterostructures with various functionalities in electronics and optoelectronics. However, in most studies the 2D heterostructures were constructed using exfoliation and transfer approach, which possesses the disadvantages of low efficiency and low yield. It is necessary to develop new fabrication processes for large-scale production of 2D heterostructure nanodevices. This DPhil project aims to exploit the possibility to assembly 2D heterostructures by chemical vapor deposition (CVD) growth of 2D semiconductors (e.g. MoS_2, WS_2 and GaS) using pre-patterned graphene as growth template, which enables large-scale fabrication of graphene based nanodevices in photodetection applications.

In the first part of fabrication of MoS_2:graphene vertical heterostructure, a new ambient pressure CVD process was developed via control of chemistry of graphene and MoS_2 by hydrogen addition, which enables the direct growth of centimeter-scale continuous films of vertically stacked MoS_2 monolayer on graphene. Hydrogen addition enables longer CVD growth times at high temperature by reducing oxidation effects on monolayer graphene. By careful control of nucleation density and growth time, high quality monolayer MoS_2 films could be formed on graphene, realizing all CVD grown vertical stacked monolayer semimetal-semiconductor interface. The photodetectors fabricated using this vertical heterostructure show photoresponsivity reaching 2.4A/W under 135μW 532nm illumination.

In the second part of fabrication of WS_2:graphene lateral heterostructure, a new controlled CVD process was developed to directly grow WS_2 in pre-patterned graphene gaps, creating better interfaces. By lowing the effective Schottky barrier height via improved contact between graphene and WS_2, Direct CVD grown graphene:WS_2:graphene lateral photodetecting transistors exhibit high

photoresponsivity reaching 121 A/W under 2.7×10^5 mW/cm^2 532 nm illumination, which is around two orders of magnitude higher than similar devices made by the layer-by layer transfer method.

Lastly, mass production of GaS:graphene lateral heterostructure was achieved by directly growing layered GaS in the gap of pre-patterned graphene electrode pairs on Si wafer via a selective CVD process. Due to the large band gap of GaS, the CVD grown GaS:graphene lateral photodetecting transistors is sensitive to UV light only. The detection limit could reach down to 2.61 μW/cm^2 with a photoresponsivity of 11.7 A/W and a photo gain of 53.7. The devices also show long-term stable and reproducible ON-OFF switching behavior, with a response time lower than 60 ms, which is comparable to other high-quality photodetectors made by 2D materials.

Acknowledgements

It would not have been possible to complete my DPhil journey without the guidance, contribution and support of my supervisors, colleagues, friends and family. First of all, I would like to express sincere appreciation and profound thanks to my supervisor Prof. Jamie Warner for providing me with supervision and motivation throughout this project. This Ph.D. project cannot be accomplished without his unconditional support and valuable suggestions. His patience, enthusiasm and immense knowledge have inspired me to become an independent researcher.

Besides, I would like to express my deep gratitude to Dr. Yuewen Sheng, Dr. Xiaochen Wang, Dr. Ren-Jie Chang and Mr. Yang Lu for their ideas and advices in synthesis of 2D materials. The frequent discursions, brainstorming and collaboration with them improved my research and sharpen my skills. I would also like to express my earnest gratitude to Dr. Yinqiu Zhou, Dr. Hefu Huang, as well as Mr. Yutian Wen and Dr. Xinya Bian in Professor Andrew Briggs group for generously sharing their knowledge on nano fabrication skills, which broaden the aspects in this project.

There are several works in this project that I could hardly accomplish without the assistance from my colleagues and collaborators. I acknowledge Dr Benjamin Porter and Ms. Yu Shu in Professor Harish Bhaskaran group for their help of AFM measurement. I also appreciate Ms. Xuan Li on her experience sharing about the measurement of photoresponse time.

I would also like to express my gratitude to the rest of my colleagues, Dr. Ye Fan, Dr.

Shanshan Wang, Dr. Haijie Tan, Dr. Wenshuo Xu, Dr. Thomas Samuels, Dr. Qu Chen, Dr. Martin Tweedie, Dr. Sha Li, Dr. Jakyung Lee, Dr. Gyeonghee Ryu, Ms. Sapna Sinha, Ms. Yi Wen, Ms. Linlin Hou, Ms. Qianyang Zhang, and Mr. Peng Tang for their constructive advices and opinions during the discussion, which broadened my horizon.

I am also grateful to my friends in Oxford and UK, Zhangcan Ding, Wei Xiong, Xiaoqing, Chen, Kun Liang, Qize Ding, Youxin Kong, Tao Ni, Xiulian Yu, Yinyu Nie, Lai Zhou and Xiao Yuan for bring me an unforgettable memory during my DPhil study in Oxford.

Last but not least, I would like to express my deepest gratitude to my parents for their support and love throughout my 4-year stay in UK.

Publication list:

First and co-first author:

(1) **Chen, T**., Zhou, Y., Sheng, Y., Wang, X., Zhou, S., & Warner, J. H. (2018). Hydrogen-Assisted Growth of Large-Area Continuous Films of MoS_2 on Monolayer Graphene. *ACS applied materials & interfaces*, *10*(8), 7304-7314.

(2) **Chen, T.**, Sheng, Y., Zhou, Y., Chang, R. J., Wang, X., Huang, H., Zhang, Q., Hou, L. & Warner, J. H. (2019). High photoresponsivity in ultrathin 2D lateral graphene: WS_2: graphene photodetectors using direct CVD growth. *ACS applied materials & interfaces*, *11*(6), 6421-6430.

(3) Sheng, Y., **Chen, T.,** Lu, Y., Chang, R. J., Sinha, S., & Warner, J. H. (2019). High-Performance WS_2 Monolayer Light-Emitting Tunneling Devices Using 2D Materials Grown by Chemical Vapor Deposition. *ACS nano*, *13*(4), 4530-4537.

Publications under peer review:

(1) **Chen. T.**, Lu, Y., Sheng, Y., Shu, Y., Li, X., Chang, R., Bhaskaran, H., & Warner, J. H. Ultrathin All-2D Lateral Graphene:GaS:Graphene UV Photodetectors by Direct CVD Growth

Co-author:

(1) Chang, R. J., Tan, H., Wang, X., Porter, B., **Chen, T.,** Sheng, Y., Zhou, Y., Huang, H., Bhaskaran, H. & Warner, J. H. (2018). High-performance all 2D-layered tin disulfide: graphene photodetecting transistors with thickness-controlled interface dynamics. *ACS applied materials & interfaces*, *10*(15), 13002-13010.

(2) Wang, X., Sheng, Y., Chang, R. J., Lee, J. K., Zhou, Y., Li, S., **Chen, T.**, Huang, H., Porter, B. F., Bhaskaran, H. & Warner, J. H. (2018). Chemical Vapor Deposition Growth of Two-Dimensional Monolayer Gallium Sulfide Crystals Using Hydrogen Reduction of Ga_2S_3. *ACS omega*, *3*(7), 7897-7903.

(3) Huang, H., Xu, W., **Chen, T.,** Chang, R. J., Sheng, Y., Zhang, Q., Hou, L. & Warner, J. H. (2018). High-Performance Two-Dimensional Schottky Diodes Utilizing Chemical Vapour Deposition-Grown Graphene–MoS2 Heterojunctions. *ACS applied materials & interfaces*, *10*(43), 37258-37266.

(4) Huang, H., Sheng, Y., Zhou, Y., Zhang, Q., Hou, L., **Chen, T**., Chang R. & Warner, J. H. (2018). 2D-Layer-Dependent Behavior in Lateral

Au/WS_2/Graphene Photodiode Devices with Optical Modulation of Schottky Barriers. *ACS Applied Nano Materials*, *1*(12), 6874-6881.

(5) Lu, Y., **Chen, T.,** Ryu, G. H., Huang, H., Sheng, Y., Chang, R. J., & Warner, J. H. (2018). Self-Limiting Growth of High-Quality 2D Monolayer MoS_2 by Direct Sulfurization Using Precursor-Soluble Substrates for Advanced Field-Effect Transistors and Photodetectors. *ACS Applied Nano Materials*, *2*(1), 369-378.

(6) Yang, J., Choi, M. K., Sheng, Y., Jung, J., Bustillo, K., **Chen, T.**, Lee, S., Ercius, P., Kim, J., Warner, J.H. & Chan, E. M. (2019). MoS_2 Liquid Cell Electron Microscopy Through Clean and Fast Polymer-Free MoS_2 Transfer. *Nano letters*, *19*(3), 1788-1795.

(7) Chang, R. J., Sheng, Y., **Chen, T.,** Mkhize, N., Lu, Y., Bhaskaran, H., & Warner, J. H. (2019). Morphology Control of Two-Dimensional Tin Disulfide on Transition Metal Dichalcogenides Using Chemical Vapor Deposition for Nanoelectronic Applications. *ACS Applied Nano Materials*, *2*(7), 4222-4231.

(8) Chang, R. J., Sheng, Y., Ryu, G. H., Mkhize, N., **Chen, T.,** Lu, Y., Chen, J., Lee, J., Bhaskaran, H. & Warner, J. H. (2019). Postgrowth Substitutional Tin Doping of 2D WS_2 Crystals Using Chemical Vapor Deposition. *ACS applied materials & interfaces*, *11*(27), 24279-24288.

Table of Contents

Chapter 1

Introduction

1.1 Project Aims

The object of this doctoral project is to develop and optimize the processes for large-scale fabrication of two-dimensional heterostructures using direct chemical vapor deposition (CVD) technique. Continuous graphene film and patterned graphene ribbons were used as growth template for the growth of other 2D materials, including molybdenum disulfide (MoS_2), tungsten disulfide (WS_2) and gallium sulfide (GaS), directly forming the vertical or lateral heterostructures. These heterojunctions were then fabricated into photodetectors. A range of characterization techniques were carried out to investigate the physical and electronic properties of the products.

1.2 The Scope of this Thesis

The thesis covers the research that has been done during the four years' UK DPhil degree at the Department of Materials, University of Oxford. It starts with a literature review (Chapter 2) that summarizes the recent progress on the properties, characterization techniques and synthesis methods of 2D materials including graphene, MoS_2, WS_2 and GaS, followed by a brief introduction of the applications of 2D materials in optoelectronics and the fabrication of 2D heterostructures. In Chapter 3, the CVD setups for the growth of graphene and other 2D materials, nanofabrication of ultrathin 2D devices and a series of characterization techniques employed in this project are briefly introduced.

The first work was to synthesis continuous MoS_2 film on graphene substrate. The purpose of this work was to look for an easy and efficient method to fabricate vertical MoS_2/graphene heterojunction. Hydrogen gas was introduced to the CVD system, allowing the control of chemistry of MoS_2 and graphene to achieve the growth of centimeter-scale continuous MoS_2 film on graphene. Photodetectors were fabricated based on the as synthesized heterojunction by depositing metal bond pads, whose performance was characterized and explained in Chapter 4.

Subsequently, the focus of the study shifted to the fabrication of graphene/TMDs/graphene lateral heterostructures, which are considered the basic form of 2D phototransistors. The first attempt was to directly grow WS_2 in the gap of prepatterned graphene electrode pairs. By controlling the nucleation of WS_2, WS_2 could be selectively deposited in the gap of two graphene electrode pairs, naturally forming the graphene/WS_2/graphene heterojunction. The as fabricated phototransistors exhibited excellent photoresponsivity, owing to the lowering of Schottky barrier by improved contact. (Chapter 5). Following this, a large band gap 2D semiconductor GaS was studied as a promising candidate for 2D UV photodetector. Thanks to the previous works on the CVD growth of GaS, a modified CVD process was developed to directly deposited GaS in the channel between graphene electrode pairs, forming the graphene/GaS/graphene lateral heterojunction. By directly applying source-drain bias onto the graphene electrodes, the as fabricated devices shew photodetection behavior for UV light only. (Chapter 6)

The final chapter summarizes the whole thesis and envisions a potential future research

as extension to this thesis.

Chapter 2

Literature Review

2.1 Introduction

Since 2004 when Graphene was first discovered, remarkable success of graphene research has sparked enormous interest in a wide range of 2D materials, especially on semiconducting transition metal dichalcogenides (e.g. MoS_2 and WS_2) and metal chalcogenides (e.g. GaS) owing to their chemical stability and complementary electronic properties. Due to their unique mechanical and physical properties, 2D materials and their heterostructures are considered as one of the potential build blocks with promising features to replace Si in next generation ultrathin and flexible electronic and optoelectronic devices. This chapter is devoted to review the recent advances in synthesis and applications of 2D materials. Based on the subject of this thesis, it starts with introduction of the properties and synthesis of graphene, MoS_2, WS_2 and GaS. This is then followed by a review of optoelectronics based on 2D semiconductors with a specific focus on photodetectors, and the fabrication of vertical and lateral heterostructures based on 2D materials.

2.2 Graphene

2.2.1 What is graphene

Graphene is a carbon material which is fundamentally a two-dimensional (2D) sheet of honeycomb network composed of sp2 hybridized carbon. The 2D honeycomb network is regarded as the basic building block of other carbon materials; it can be curl up to

form zero-dimensional (0D) fullerenes, rolled to form one-dimensional (1D) carbon nanotubes, and vertically stacked and held together by Van der Waals force to form three-dimensional (3D) graphite, as shown in **Figure 2.1**.[1] The long-range π-conjugation in graphene is supposed to have extraordinary thermal, mechanical and electrical properties that have long been the focus of many theoretical studies. [2-4]

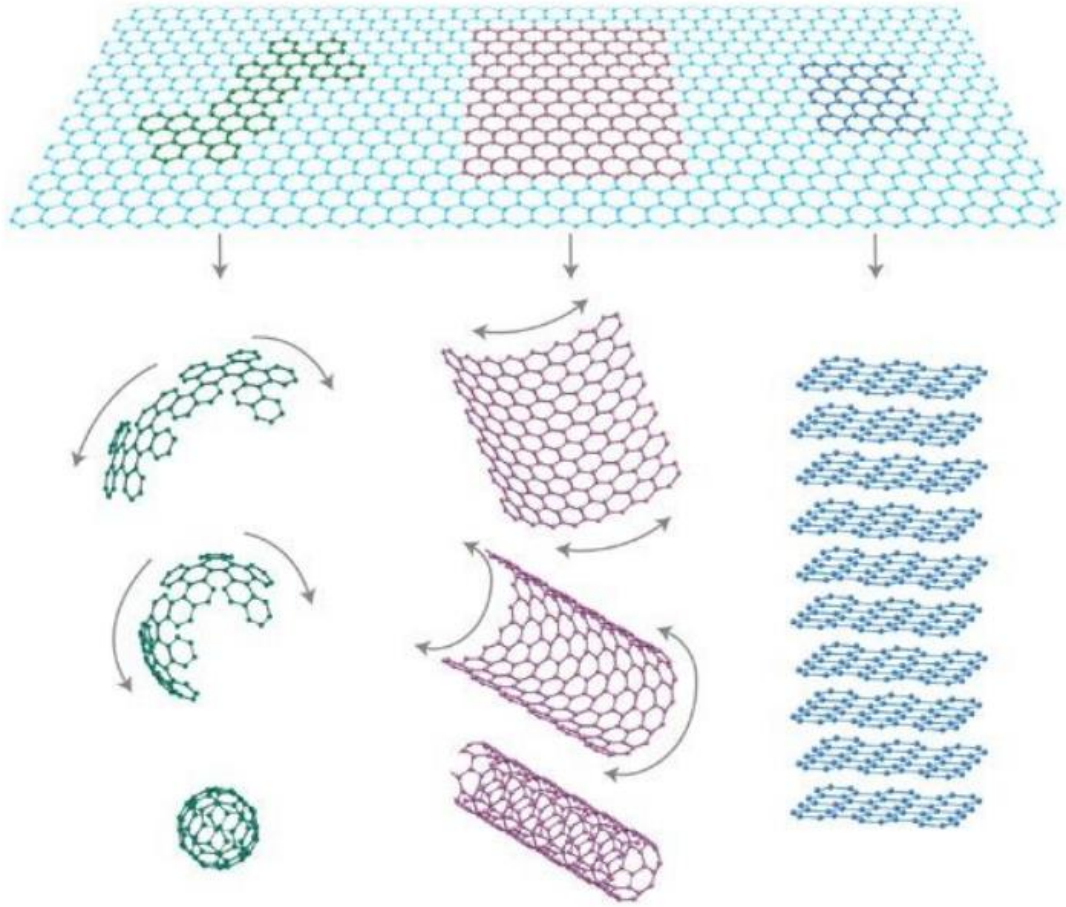

Figure 2.1. Graphene as the building block for other carbon materials in various dimensions. Graphene can be curl up to become 0D fullerenes, rolled to become 1D carbon nanotubes or stacked to become 3D graphite. Reprinted with permission from ref. [1]. **© 2007 Nature Publishing Group**

Although the history of graphene could date back to 1859 when British chemist Benjamin Brodie exposed graphite to strong acid and obtained a suspension of graphene oxide,[5] it was not until 2004 that the study in graphene leapt to prominence. In that year, the successful separation of graphene from highly oriented pyrolytic graphite (HOPG) was first achieved using mechanical exfoliation method by Prof. Andre Geim and Prof. Konstantin Noveselov.[6] The experimental isolation of single-layer graphene enabled measurement and quantification of graphene's unique properties for the first time. A large amount of interesting physics were observed shortly afterwards, including graphene's ambipolar field effect,[5] the quantum Hall effect at room temperature,[7-9] high carrier mobility,[10-13] and the first ever detection of single molecule adsorption.[14-15] Prof. Geim and Prof. Novoselov were awarded the Nobel Prize in Physics in 2010 for their pioneering work in 2D materials.

Besides the all these new physics mentioned above, the unique physical and electrical properties of graphene also generated huge interest in the possible implementation of graphene in a selection of applications, including reinforcement composites,[16] corrosion protection,[17-18] display and touch screen,[20] infrared sensors,[21-22] solar cells,[23-24] etc. [25-27]

2.2.2 Properties of Graphene

In this section, some of the characteristic properties of graphene will be discussed. Since the first isolation of graphene in 2004, the majority of graphene-related research interest has been on graphene's excellent mechanical properties, thermal and vibrational properties and novel electrical properties, such as high carrier mobility and existence of

a massless Dirac fermion system, which are very important in various applications and characterization of graphene.

2.2.2.1 Mechanical Properties of Graphene

The theoretical studies predicted that graphene would have extraordinarily mechanical properties.[28] The first experimental measurement of graphene's mechanical properties was performed with help of atomic force microscope (AFM).[29] A graphene sheet was suspended over a substrate embedded with an array of micrometer scale perforation. The elastic and inelastic breaking strength could be measured by applying force using an AFM tip on the surface of suspended graphene. It was discovered that graphene has an intrinsic strength of 130 ± 10 GPa and a Young's modulus of 1.0 ± 0.1 TPa. However, the extraordinarily high experimental value was not only ascribed to the nature of graphene, but also to the fact that the measurement was performed on relatively defect-free regions, as the experimental value was very close to ab initio calculations based on single layer, defect-free graphene.[30-31] The experimental strength of a relatively more defective graphene sheet could vary a lot, owing to different type, size and density of defects in the target area under the tip.

Other mechanical properties of graphene, such as flexibility, elasticity and mechanical stability have been quantified by transferring as prepared graphene film on PET substrate.[19] It was discovered that the graphene is perfectly elastic until 18.7% strain applied. The further experiments indicated that graphene has outstanding transparency and flexibility, which shows great potential to replace ITO in applications such as optoelectronic devices.[19]

2.2.2.2 Thermal properties

Thermal conductivity is a critical figure of merit for materials used in nanoelectronics, as the needs for heat dissipation rise along with increased miniaturization. The experimental measurements have proved that free-standing monolayer graphene has an excellent thermal conductivity of ~ 5,000 W m^{-1} K^{-1} at room temperature, matching with theoretical predictions.[32-33] This was measured on a suspended single layer graphene by extracting graphene's characteristic Raman signal, using a non-contact confocal Raman spectroscopy technique. (see section 2.2.2.3) The principle is that the position of G peak in Raman spectrum of graphene is dependent on the excitation laser power and temperature.

Nevertheless, graphene mostly requires it to stay on a substrate in practical. Comparing to ideally suspended graphene, the phonon coupling with the substrate could likely reduce graphene's thermal conductivity. For example, using similar measurement method mentioned above, the thermal conductivity of graphene on SiO_2/Si substrate at room temperature could reduce to 600 W m^{-1} K^{-1}.[34]

2.2.2.3 Vibrational properties

Raman spectroscopy, a non-destructive technique that relies on inelastic scattering, is commonly used to determine the vibrational properties of graphene.[35-37] The Raman spectroscopy is usually measured by illuminating a monochromatic light source on the sample. The majority of the incident light can be scattered elastically by the sample, in a process called Rayleigh scattering, while the rest of light is scattered inelastically due to the vibrational phonons in the lattice of target sample. The principle of Raman

spectroscopy is to detect the frequency variations of the excitation source caused by inelastic scattering, illustrated by Raman peaks in Raman spectrum whose X axis is the frequency shift and Y axis describes the intensity of inelastically scattered light. It is an important technique to identify the quality and quantify the thickness of graphene.

There are two predominant peaks in Raman spectra of graphene and graphite: G peak at ~1580 cm^{-1} and 2D peak at ~2700 cm^{-1}. G peak is a signature of carbon-carbon in-plane vibration mode, related to doubly degenerate E_{2g} mode at the Brillouin zone center. In other words, it is caused by the bond stretching of all sp^2 carbon atom pairs. On the other hand, 2D peak is the overtone of D peak, which relates to transverse optical phonons at the edge of the Brillouin zone, also known as the breathing mode to sp^2 aromatic ring. However, D peak only presents in defective graphite or graphene samples while 2D peak is always detectable. This is because that the activation of D peak follows a double resonance activation (DR) mechanism that needs defects for initiation, contrary to 2D peak whose activation does not require defects. Similar mechanism also applies to D' peak, locating at ~1600 cm^{-1}, which is only detectable in strongly disordered graphene. The presence of D and D' peak and their relative intensity to G peak provides an effective identification of the defect level in graphene samples. [36]

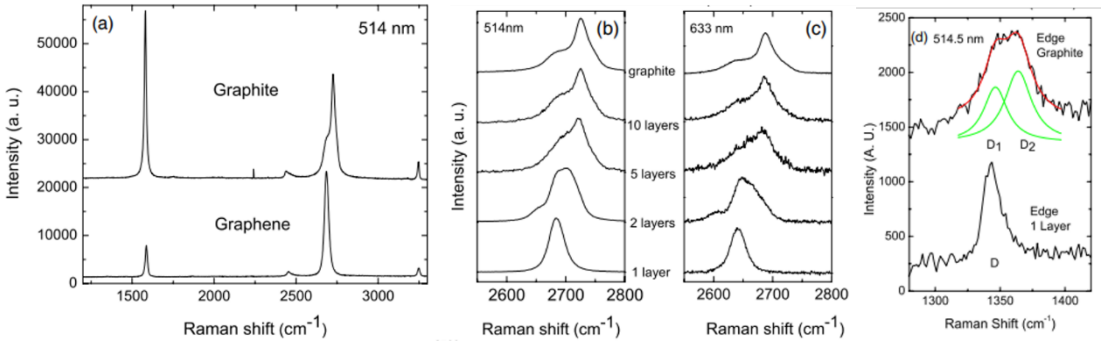

Figure 2.2. The vibration properties of graphene. (a) Raman spectra of graphite and graphene. (b-c) Evolution of 2D peak as a function of layer number under 514 nm (b) and 633 nm (c) excitation wavelength. (d) D peak of graphite edge (top) and graphene edge (bottom). Reprint with permission from ref. [36]. © **2006 American Physical Society**

Figure 2.2 shows the Raman spectra of graphite and monolayer graphene. They can be easily distinguished by the shape of 2D peak, its position and its relative intensity to G peak. As the layer number increases, the position of G peak slightly red shifted. The 2D peak of monolayer graphene could be fitted into one Lorentzian peak. When the number of layers increases, the 2D peak gradually blue shifts and the shape evolves into a broaden peak made up of several Lorentzian peaks. The intensity of lower frequency Lorentzian subpeak in the 2D peak decreases along with increasing thickness, eventually turning to the shape observed in the Raman spectrum of bulk graphite. [36]

When incident excitation light interacts with different graphene samples, their Raman spectrum could exhibit different peak positions and peak shapes. Comparing to optically identification by contrast or AFM measurement, Raman spectroscopy is an efficient, effective and non-invasive technique to give a quantitative evaluation of

thickness and identification of defect level in graphene sheets.

2.2.2.4 Electronic Properties

In the planar structure of graphene, the carbon-carbon σ-bond spread out to 120° separation, yielding a hexagonal symmetry. The valence and conduction bands of graphene meet at K and K' points across k-space, which makes graphene a so-called zero-bandgap semiconductor or semimetal. The K and K' point originate from two unique lattice vectors of graphene lattice, as illustrated in **Figure 2.3(a)**. There are altogether six of these so-called Dirac points across the Brillouin zone. (**Figure 2.3(b)**) Ideally, the conduction band is empty while the valence band is filled in pristine graphene. The relationship between energy and momentum is linear near the Dirac points, making the charge carriers in graphene so-called massless Dirac fermions.[38] In other words, they can be regarded as relativistic particles that travel at speed of light with an effective mass of zero.[11]

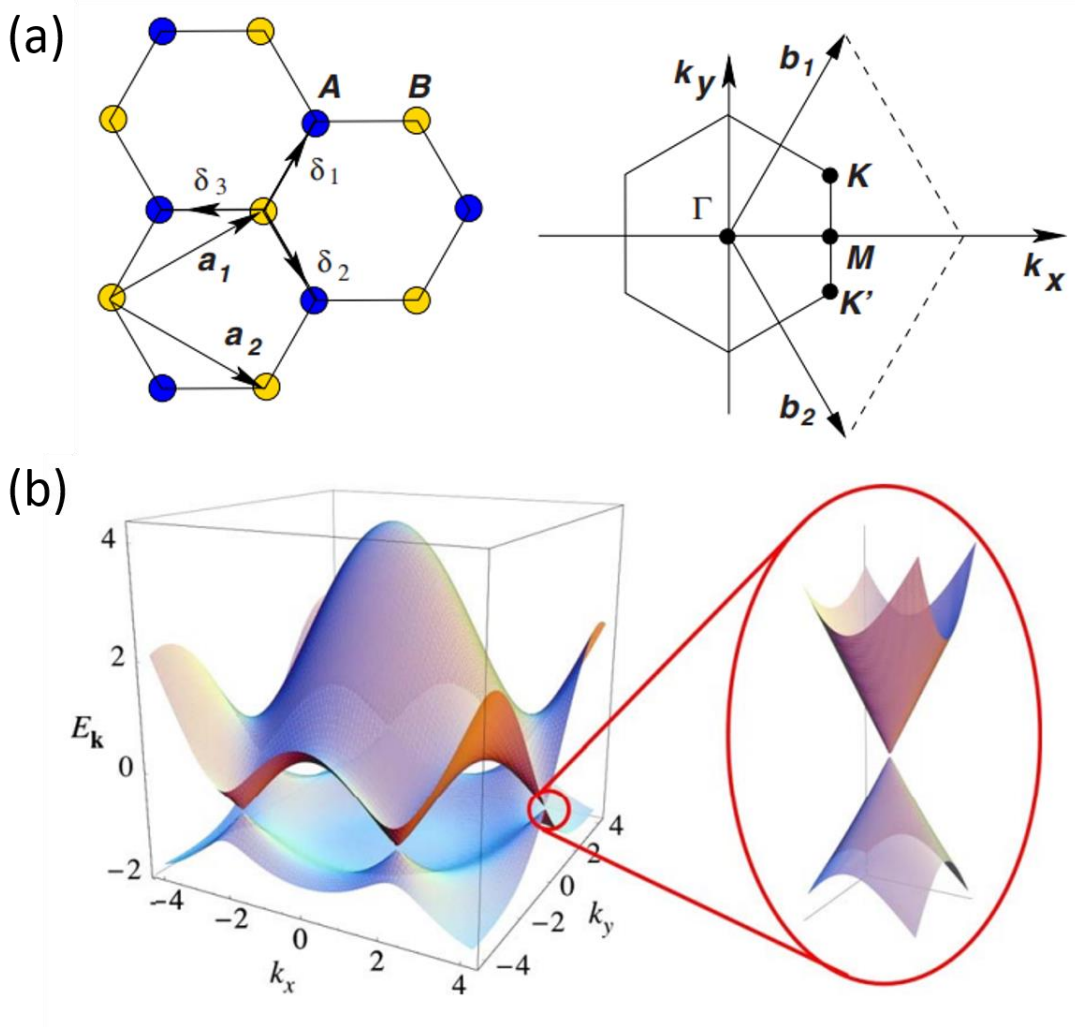

Figure 2.3. The lattice structure of monolayer graphene and its band structure. (a) Planar structure of monolayer graphene composed of sp^2 hybrid carbon atoms(left) and Brillouin zone of graphene (right). (b) Energy spectrum of graphene with a zoom-in image of Dirac cone at K and K' points. Reprinted with permission from ref. [38]. © **2007 Nature Publishing Group**

Additionally, graphene exhibits an ambipolar field effect due to the linear dispersion relation. By tuning the Fermi level via a gate voltage or doping, either holes or electrons can be the majority type of charge carriers in graphene, resulting in an intrinsic carrier

mobility of free-standing graphene as high as ~200,000 $cm^2V^{-1}s^{-1}$ at room temperature.[10] The mobility of graphene is superior than any other well-studied conventional semiconductors, such as silicon (~1,400 $cm^2V^{-1}s^{-1}$),[39] carbon nanotubes (~100,000 $cm^2V^{-1}s^{-1}$),[40] gallium arsenide (GaAs) (~4,600 $cm^2V^{-1}s^{-1}$).[41] and indium antimonide (InSb) (~77,000 $cm^2V^{-1}s^{-1}$).[42] This unique property makes ultra-thin graphene films possible candidates in high speed nanoelectronics applications, including high frequency devices and field effect transistors (FETs).[43]

However, in practice the mobility of graphene can be lowered by various factors, such as grain boundaries, defects, surface impurities and phonon interactions at the interface, which cause the scattering of charge carrier.[44-45] For example, the mobility of monolayer graphene transferred on silicon wafer(SiO_2/Si) was measured to be 16,000 $cm^2V^{-1}s^{-1}$,[1] and 35,000-60,000 $cm^2V^{-1}s^{-1}$ on hexagonal boron nitride (hBN).[46-47]

2.2.2.5 Transparency

Graphene is regarded as a potential candidate for transparent conductor owing to its good transparency. According to the theoretical calculation, the transmittance (T) of monolayer graphene could be estimated by the following equations:

$$\alpha = \frac{e^2}{hc} \approx \frac{1}{137}$$

$$T = (1 + \frac{\pi\alpha}{2})^{-2} \approx 1 - \pi\alpha \approx 97.7\ \%$$

where e is the elementary charge, h is the Planck's constant, c is the speed of light and α is the fine structure constant describing the coupling between photons and electrons.[48] The experimental results matched well with the theoretical calculation, exhibiting a 2.3 % absorption of normal incident light per layer, which is much better than ITO coatings

(50 nm -200 nm) whose transparency is around 70-90% in white light spectrum region.[49]

2.2.3 Preparation of graphene

The unique properties of graphene have attracted great research interest since its discovery. Along with the "graphene boom", the need to produce high quality graphene rose. If one can develop an efficient synthesis method to produce large-scale, high-quality graphene, one big problem that hinders the implementation of graphene in industrialized productions can be resolved. Up to now, there are primarily two types of synthesis strategy: top-down route and bottom-up route. The top-down method aims to separate graphite layers by breaking the van der Waals force between them, such as mechanical exfoliation and chemical exfoliation. The bottom-up approach aims to synthesize graphene using alternative carbon sources, such as oriented growth on silicon carbide (SiC) and chemical vapor deposition (CVD).

2.2.3.1 Mechanical exfoliation

Mechanical exfoliation was first developed by Geim et al. in 2004, which is well-known as the "Scotch tape" method.[6] (**Figure 2.4**) It is a remarkably simple method to isolate graphene. Briefly speaking, an adhesive tape is used to remove flakes of graphite from highly order pyrolytic graphite (HOPG). Graphene flakes with varying thickness and size could be obtained by several peeling iterations. Subsequently, after transferring the graphene flakes from the sticky tape to a silicon substrate (300 nm SiO_2/Si), the layer number could be identified by contrast under an optical microscope.

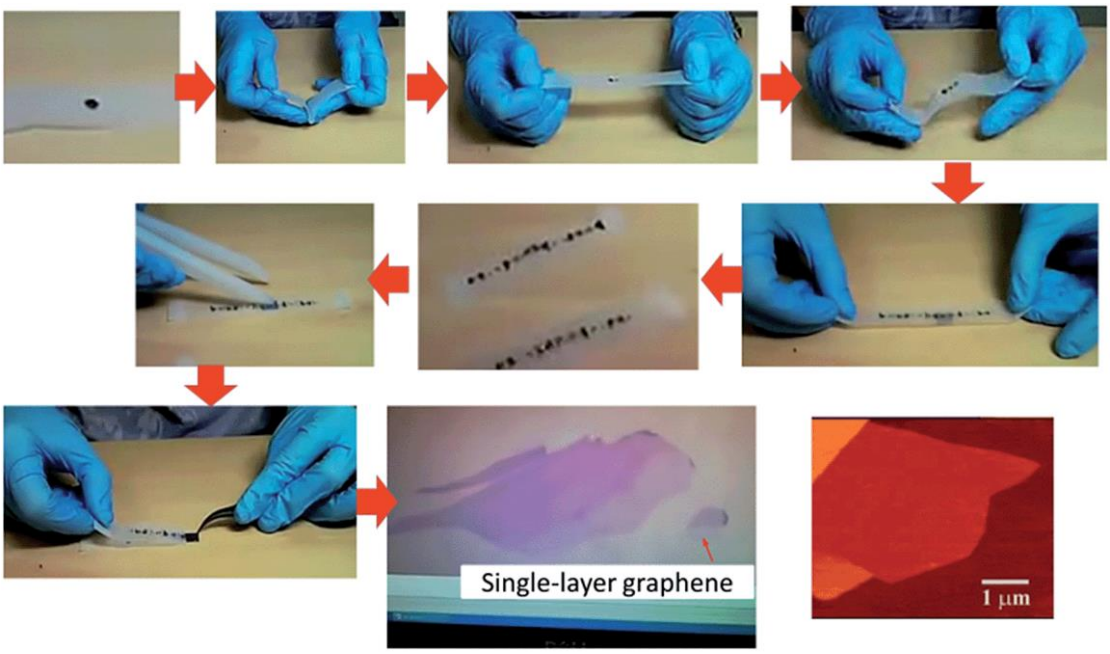

Figure 2.4. An illustration of the Scotch-tape method to isolate graphene flakes from HOPG. Reprinted with permission from ref. [50]. **© 2015 The Royal Society of Chemistry**

This breakthrough enables easily isolation of graphene flakes large enough to perform all sorts of measurements to quantify the basic properties of graphene. However, despite that this method is straightforward and accessible to everyone, there are still several drawbacks on this method. It is time-consuming to locate the exfoliated graphene flakes and the size of these flakes is usually limited to sub-micron scale, which is only suitable for fundamental studies, but not for mass production.

2.2.3.2 Chemical Exfoliation

The wet chemical exfoliation of graphene can be achieved by two methods: liquid-phase exfoliation (LPE) and the reduction from graphene oxide (GO) to graphene.

In a typical liquid-phase exfoliation process, graphite flakes are dispersed in a solvent

followed by an exfoliation process to isolate individual layers. To successfully isolate graphene layers, the van der Waals interaction between adjacent layers of graphite should be overcome. Solvents that have a similar surface tension with graphene (46.7 mN/m) would be suitable for exfoliation.[51] N-Methylpyrrolidone (NMP, 40 mN/m),[52] N,N'-dimethylformamide (DMF, 37.1 mN/m)[53] and *ortho*-dichlorobenzene (o-DCB, 37 mN/m),[54] are popular solvents used to exfoliate graphene layers.

The reduction of graphite oxide or graphene oxide to graphene is another low-cost technique for large-scale production of graphene. The Hummers method is the most well-developed and widely used chemical process to prepare GO sheets. The oxidation of GO is achieved through the addition of potassium permanganate ($KMnO_4$) into a mixed solution of graphite, sodium nitrate ($NaNO_3$) and sulfuric acid (H_2SO_4).[55] The GO sheets are then chemically reduced to graphene sheets by reducing agents, including hydrazine (N_2H_4),[56] hydriodic acid (HI),[57] sodium borohydride ($NaBH_4$),[58]and dimethyl hydrazine.[59]

The chemical exfoliation methods provide a possible solution to mass produce graphene sheets. However, the exfoliated products are usually of extremely poor quality and inhomogeneity in structure and size, which is not suitable for applications in nanoelectronics.

2.2.3.3 Oriented Growth on Silicon Carbide

In 2004, Berger et al.[60] first reported the formation of oriented graphene film on the single-crystal silicon carbide (SiC) surface by heat treatment in an ultra-high vacuum (UHV). The reaction started with thermal decomposition of SiC, which silicon atoms

evaporate from the SiC surface. Remaining carbon atoms then rearranged and re-bonded to form oriented graphene layers on the substrate. Generally, the thickness of oriented graphene films prepared by this method ranges from one to three layers, varying with the decomposition temperature of SiC.[61] **Figure 2.5** illustrates four low energy electron diffraction (LEED) patterns captured *in situ* during the oriented growth of a graphene film about 2.5-layer thick.

Although this method has potential for the production of graphene films with relatively high yield, the domain size of graphene is usually limited to micro scale, leading to a mobility as low as ~2.5 $cm^2V^{-1}s^{-1}$.[61] To improve the quality of graphene, Emtsev et al.[62] optimized the process by heating the SiC in an argon atmosphere (900 mbar), aiming to reduce the surface roughness of SiC. Continuous graphene films about 50 μm in length could be synthesized with improved single domains size. The mobility was measured to be around 2,000 $cm^2V^{-1}s^{-1}$ at ~27K. However, it is very challenging to transfer graphene from SiC to other substrates, which unfortunately limits the versatility of this method in industrialized production of electronic and opto-electronic.

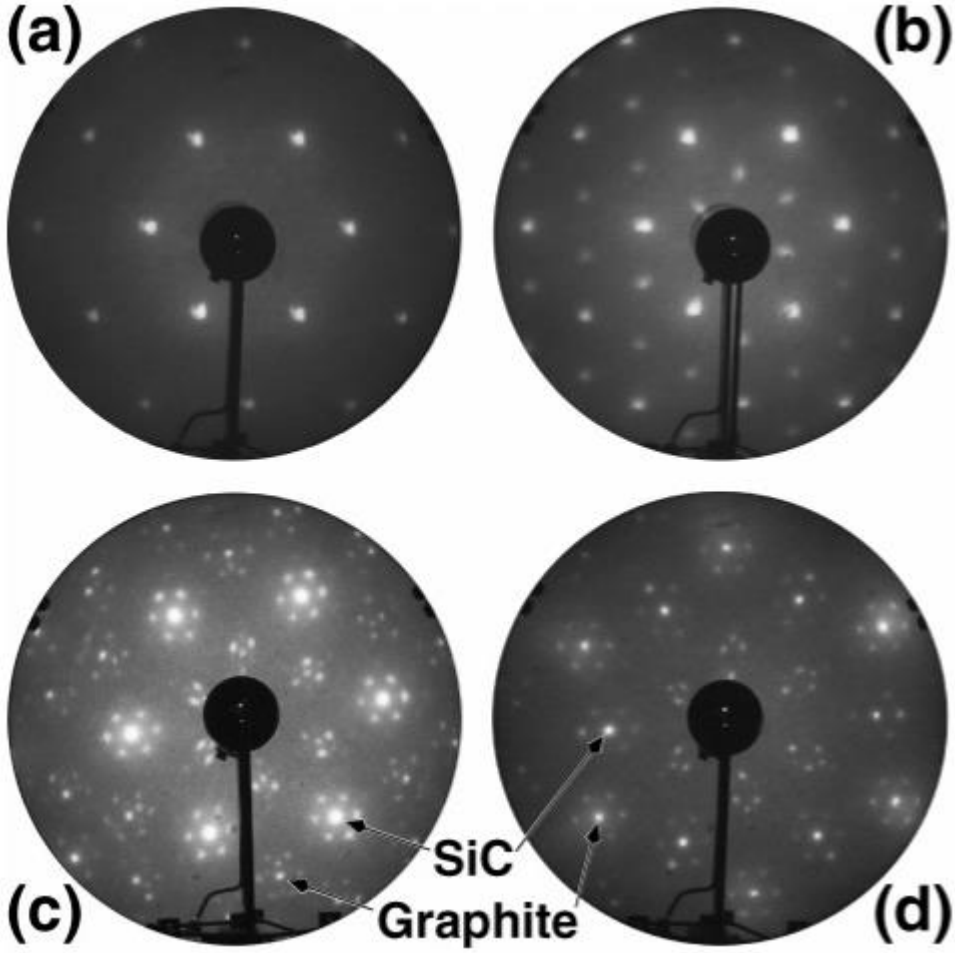

Figure 2.5. Oriented Growth on Silicon Carbide. (a-d) LEED patterns from graphite/SiC(0001) during successive heating process. (a) 1050 °C. (b) 1100 °C. (c) 1250 °C (d) 1400°C**.** Reprinted with permission from ref. [60]. **© 2004 American Chemical Society.**

2.2.3.4 Chemical Vapor Deposition

Among all the methods to synthesize graphene sheets, CVD is widely considered as one of the most promising methods to meet the industrial requirements. Using gaseous carbon source as precursor and metal as substrate, continuous, high-quality graphene films can be synthesized, whose area is only limited to the size of the substrate itself.

In a typical CVD process to grow graphene, gaseous carbon sources, such as methane (CH_4), first decompose on the catalytic metal surface at high temperature to generate hydrocarbon intermediate species (CH_x), which then react on metal surface to form graphene layers. The first attempt to grow thin graphitic film using CVD method can date back to 1969.[63] Since then, CVD growth of graphene has been performed on a variety of metal substrates, including Ni,[64] Cu,[19] Fe,[65] Ru,[66] Co,[67] Pt[68] and Au.[69] Among them, Ni, Cu and their alloy are the most attractive substrates due to their high catalytic efficiency and relatively low cost.

At early stage of graphene study, Ni was believed to be an ideal substrate to grow graphene since the lattice constant of Ni(111) plane is similar to that of graphene.[70] As is illustrated in **Figure 2.6(a)**, the growth of graphene on Ni is a surface segregation process. Carbon has a high solubility in Ni film at high temperature. Therefore, when the Ni film is cooled down, carbon atoms precipitate on the surface of metal and formed graphene layers.[70] However, as graphene is formed during the cooling process, the thickness and quality of the graphene sheets are primarily determined by cooling rate, which it is difficult to control.

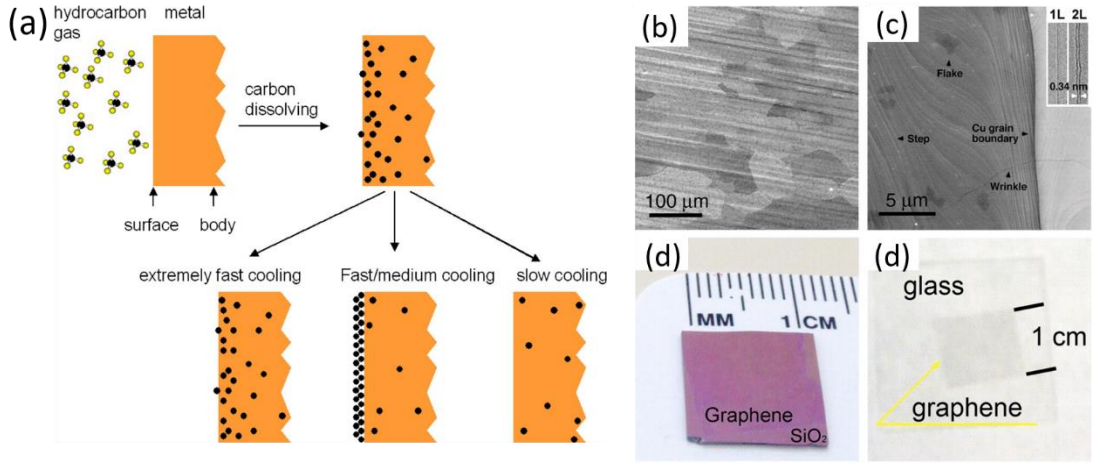

Figure 2.6. CVD growth of graphene on metal substrate. (a) Schematics of carbon segregation process at metal surface with different cooling rates. Reprinted with permission from ref. [70]. **© 2008 American Institute of Physics.** (b-c) SEM images of as grown graphene on copper substrate. (d-e) Optical images of graphene transferred on SiO_2/Si and glass. Reprinted with permission from ref. [71]. **© 2009 American Association for the Advancement of Science**

On the other hand, Cu has a relatively low carbon solubility, which limits the diffusion of carbon to metal surface. In 2009, Li et al.[71] used copper foil as substrate to synthesize large scale monolayer graphene by CVD process. **Figure 2.6(b)** shows the SEM images of graphene on the copper substrate and as-transferred graphene on SiO_2/Si and glass substrate. The wrinkles on the copper surface in the SEM image were a clear identification of the presence of graphene film. Raman characterization confirmed that the as synthesized graphene film was mostly single layer with only a small percentage of multilayer graphene. The carrier mobility can reach up to 4,050 $cm^2V^{-1}s^{-1}$.[71] This method was further improved by Sony who demonstrated low pressure chemical vapor

deposition (LPCVD) process to produce a 100-meter-long continuous graphene film with a comparable quality to other conventional graphene produced by CVD.[72]

Despite the good scalability to produce graphene on Cu substrate, the quality is still beyond the requirement for commercial electronics. During the CVD process, grain boundaries in graphene film can be formed as misaligned graphene islands with different orientations join together, which dramatically influences the physical and electrical properties. This is overcome by a recent study done by Ming et al.[73] using a single crystal Cu/Ni(111) alloy foil as growth substrate. Thanks to the formation of Cu_6Ni_1 superstructure on the top layers of Cu/Ni substrate, oriented graphene domains could nucleate on the alloy surface very quickly and merge together to form continuous film without grain boundaries. It was reported that very high-quality graphene, either single crystal or mostly single crystal graphene film, over large area, can be formed within 5 min. This is perfect for the future commercial production of large-scale transparent electrodes.

2.2.4 Transfer of Graphene

Graphene directly grown on metal surfaces, such as Ni, Cu and their alloy, has limited applications in industry. In most cases, graphene films are required to be on non-metallic substrate such as SiO_2/Si or polymers. Various transfer methods have yet been developed to fulfill this need, among which wet transfer and dry transfer methods are two most widely studied and used techniques

2.2.4.1 Wet Transfer

Up to now, the most widely used transfer method in laboratories is the wet transfer

method. A typical wet transfer process starts with coating of poly(methyl methacrylate) (PMMA) in anisole solution as a polymer buffer layer. The PMMA layer helps to maintain the integrity of graphene during the transfer process.[19] The metal substrate can be subsequently removed using proper etchants, for example iron (III) chloride or ammonium persulfate (APS) solution, without damaging the graphene. The PMMA/graphene film is then rinsed by floating on deionized (DI) water to wash away chemical residues from etchant solution. Upon transfer, the PMMA scaffold can be removed by organic solvent like acetone.[74]

Despite that this technique is easy to process, there are several drawbacks. Due to the fragile nature of polymer scaffold, it is difficult to use this technique to transfer large area graphene films. The contaminations from polymer residues and the etchant solution are usually inevitable. Besides, both organic and inorganic chemical waste are generated during this process, which is not eco-friendly.[75]

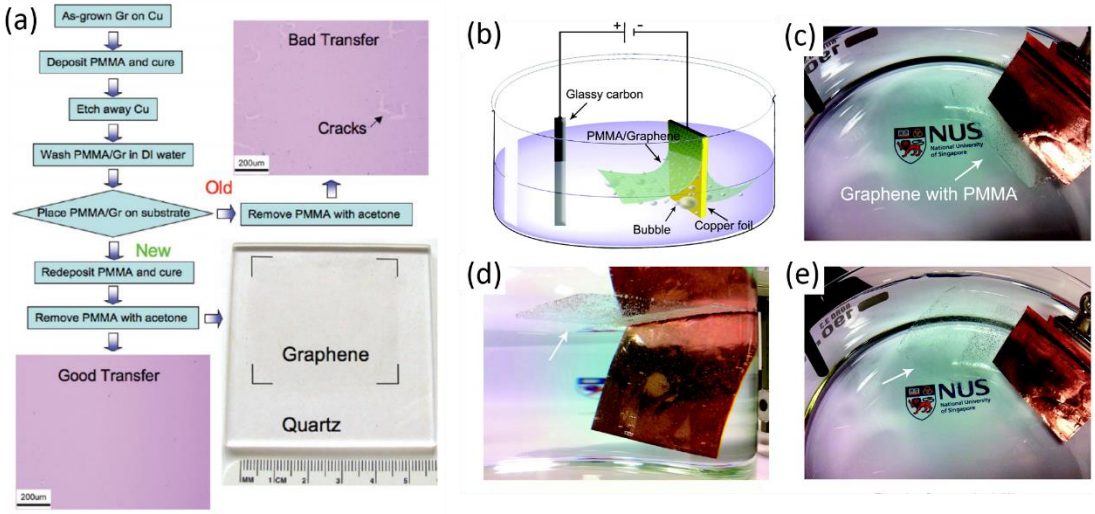

Figure 2.7. Wet transfer of graphene (a) Schematic illustration of processes for wet transfer of graphene films. The top-right and bottom-left images are the optical images of as transferred graphene on SiO_2/Si substrate using "old" and "new" transfer method, respectively. Reprinted with permission from Ref. [74]. **© 2009 American Chemical Society.** (b) Schematic of electrochemical cell used for the "bubbling" method. (c-e) Photographs illustrating the peeling process of PMMA/graphene film from copper foil. ref. [76]. **© 2011 American Chemical Society**

Another technique, known as "bubbling transfer" method, is also widely used to separate graphene from Cu substrate via an electrochemical process.[76] Using glassy carbon as anode and Gr/Cu as cathode, graphene can be separated from Cu by electrolysis of water which generates hydrogen bubbles between graphene and Cu. This technique can significantly lower the pollution and cost by recycling Cu substrate, but the PMMA/graphene film is more likely to fracture during this process.

2.2.4.2 Dry transfer

Instead of PMMA, the dry transfer methods utilize polydimethylsiloxane (PDMS)

stamp or thermal release tape (TRT) as polymer support. After the metal etching and cleaning processes, graphene on the polymer supporting layer can be stamped, pressed or rolled to a target substrate. Lee et al. [77] reported transfer of wafer-scale graphene onto arbitrary substrates using polymer assisted dry transfer method, followed by batch fabrication of FET arrays, as shown in **Figure 2.8**. Shortly afterwards, Bae et al.[72] introduced a transfer system that combines adhesion of polymer buffer layer, metal etching, rinsing, and dry transfer in a roll process, which can efficiently transfer and stack graphene layers onto a target substrate. Kim et al.[78] developed a transfer process using the pressure-sensitive adhesive film (PSAF) as supporting polymer scaffold, taking advantage of the difference in wettability and adhesion energy of graphene between PSAF and target substrate. After etching away metal substrate, the PSAF/graphene film can be attached to target substrate by weak pressing or rolling, followed by peel-off of PSAF scaffold. The surface of graphene transferred by this method was claimed to be cleaner than conventional transfer processes using PMMA or TRT.

In conclusion, the dry transfer method is suitable to transfer wafer-scale graphene films. However, polymer residues and the problem of integrity of graphene usually accompany this method.

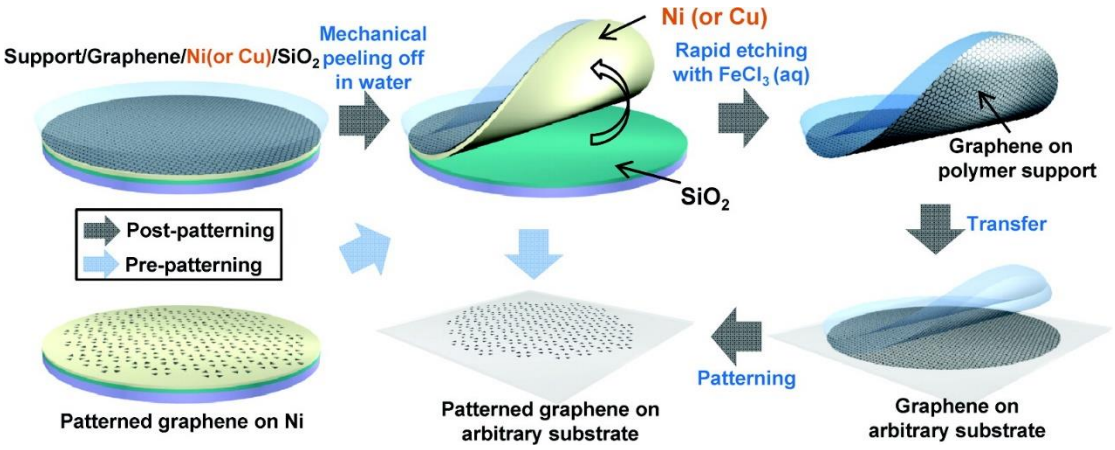

Figure 2.8. Dry transfer of graphene on copper. Schematics of preparation, etching and transfer of wafer-scale graphene films to arbitrary substrate using dry transfer method. Reprinted with permission from ref. [77]. **© 2009 American Chemical Society.**

2.3 Transition Metal Dichalcogenides (TMD)

Since the discovery of unique physical properties of graphene triggered an explosion of research in 2004, a wide variety of other 2D materials have also receive great attention. In particular, transition metal dichalcogenides (TMDs) has become the one of the biggest research interests in 2D materials thanks to their intriguing properties.

TMDs are a class of materials with the chemical composition of MX_2, where M stands for a transition metal element from group IV (e.g. Ti, Zr, Hf), group V (e.g. V, Nb, Ta) or group VI (e.g. Mo, W), and X stands for a chalcogen (S, Se, Te).[79] These materials have a layered structure in the form of X-M-X, with a plane of metal atoms sandwiched by the chalcogen atoms in two hexagonal planes, as shown in **Figure 2.9(a)**. The sandwich layers are held together by weak van der Waals force.[80] These materials present diverse electrical properties, including metallic (e.g. VSe_2, NbS_2,), semi-metallic (e.g. WTe_2, $TiSe_2$), semiconducting (e.g. MoS_2, WS_2) and insulating (e.g.

HfS_2).[81]

These TMDs usually have various polytypes and polymorphs, also known as stacking order and metal coordination geometry, respectively. There are three most common polytypes for TMDs: 1T, 2H and 3R. The numbers represent the number of layers in the unit cell and the letters stand for different crystal symmetry systems: trigonal (T), hexagonal (H) and rhombohedral (R), respectively.[81] (**Figure 2.9(b)**). Among these polytypes, 2H phase TMD semiconductors from group VI (e.g. MoS_2, WS_2, WSe_2) are considered as promising candidates in areas including flexible and transparent electronics and opto-electronics due to excellent thermodynamic stability.[82]

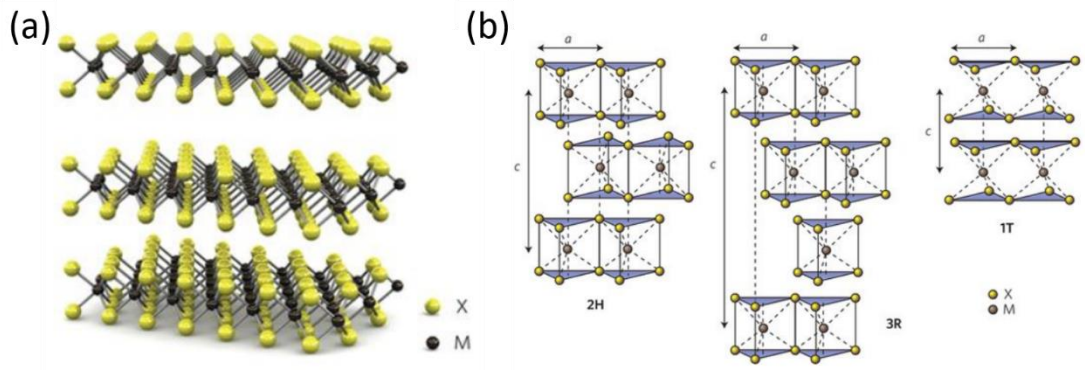

Figure 2.9. Structure of TMDs. (a) Schematic illustration of layered TMDs, with X representing chalcogen atoms and M representing metal atoms. (b) Illustration of 2H, 3R and 1T structural polytypes. Reprinted with permission from ref. [81].

MoS_2 was the first semiconducting TMD isolated in the single layer form. Monolayer MoS_2 has a direct bandgap of 1.8 eV.[83] Thus far, MoS_2 has achieved major breakthroughs in a selection of fields, including energy conversion,[84] energy storage,[85]

hydrogen evolution reaction (HER),[86] stretchable electronics,[87] field-effect transistors (FETs),[88] memory devices,[89] and photodetectors.[90] Shortly after MoS_2, WS_2 was successfully isolated and gained its popularity. Monolayer WS_2 has a direct bandgap around 2.1 eV.[91] The photoluminescence (PL) yield of monolayer WS_2 is several tens of times higher than monolayer MoS_2.[91] Theoretical simulations suggested that monolayer WS_2 has a reduced effective mass comparing to other 2D semiconducting TMDs, leading to its highest mobility among them. [92] Since the melting point of bulk WS_2 is much higher than that of bulk MoS_2, WS_2 is expected to be more thermodynamically stable than MoS_2. Thanks to its exotic properties, WS_2 has become the popular member of TMDs family in various applications, including laser,[93] LED,[94] FETs,[95] and solar cells[96]

2.3.1 Molybdenum Disulfide (MoS_2)

2.3.1.1 Properties of MoS_2

2.3.1.1.1 Mechanical Properties

Like graphene, the 2D MoS_2 sheet has extraordinary flexibility which is essential in applications of bendable devices. The elastic modulus of suspended monolayer MoS_2 could be measured with AFM tip, using the similar method mentioned in section 2.2.2.1. [29] The 2D elastic modulus of single layer MoS_2 is ~ 170 N/m, nearly half the value of grapehene (~340N/m).[97]

2.3.1.1.2 Electronic Properties

Bulk 2H-MoS_2 is a well-known semiconductor with an indirect bandgap of 1.29 eV. However, when the layer number is reduced to single layer, a transition from indirect

to direct bandgap occurs.[98] Theoretical band structures simulated with first principles density functional theory (DFT) can give an insight into the influence of low-dimension quantum confinement.

Figure 2.10(b-d) shows the calculated band structure of bulk, bilayer and single layer MoS_2. In bulk MoS_2, the smallest gap between conduction band and valence band is from Γ to Σ which locates between the K and Γ point of the Brillouin zone. As the thickness reduces to two layers, the valence band maximum (VBM) remains at Γ point whereas the conduction band at Σ shifts upwards and surpasses the K point, which consequently become the CBM. When the layer number further decreases to monolayer, the valence band at K point shifts upwards and become the new VBM, enabling the transition from indirect to direct bandgap of ~ 1.9 eV.[99]

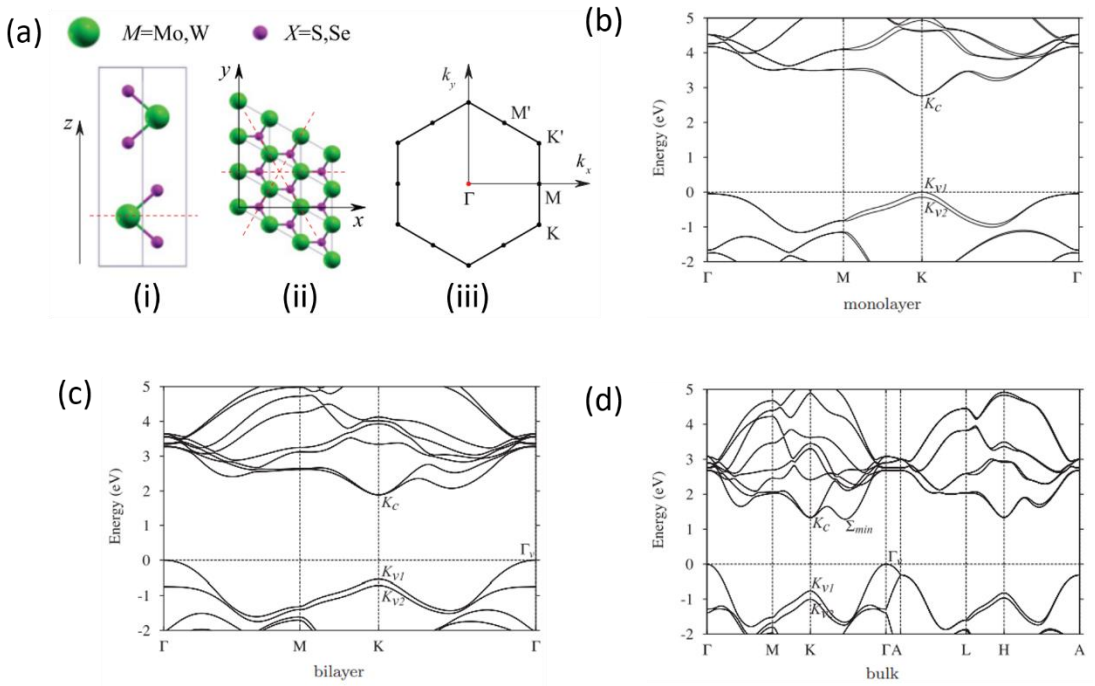

Figure 2.10. Electronic properties of MoS_2. (a) Brillouin zone for 2H-MX_2 TMDs, in which (i) Side view of the unit cell, containing two monolayers. (ii) Top view. (iii) First Brillouin zone of the MX_2 TMDs. Dashed lines indicate mirror planes. Reprinted with permission from ref. [98]. **©2011 American Physical Society** (b-d) Electronic band structures of monolayer (b), bilayer (c) and bulk (d) MoS_2. Reprinted with permission from ref. [99]. **©2012 American Physical Society**.

Another interesting phenomenon in the band structure of MoS_2 is the sizable spin-orbit (SO) splitting at the edge of both valence band and conduction band, owing to the absence of inversion symmetry.[100] The SO splitting exists in both monolayer and bilayer MoS_2,[99] leading to two so-called A and B exciton peak in photoluminescence (PL) spectrum of MoS_2, which will be further discussed in section 2.3.1.1.4.

The large direct bandgap of monolayer MoS_2 makes it a promising candidate in nanoelectronics. In transistors fabricated with single layer MoS_2, the electron mobility

of monolayer MoS_2 turned out to be ~200 cm^2 $V^{-1}s^{-1}$ at room temperature with a hafnium oxide (HfO_2) dielectric gate. The on-off ratio could reach up to 1×10^8.[101]

2.3.1.1.3 Vibration Properties

Like graphene, Raman spectroscopy is a convenient and non-invasive characterization method to identify the evolution of structural parameters in layered MoS_2 samples. Generally, there are two predominant peaks, E_{2g}^1 and A_{1g}, in the Raman spectra of MoS_2. In specific, E_{2g}^1 and A_{1g} are two peaks indicating in-plane and out-of-plane vibration mode of S atoms, respectively, as illustrated in **Figure 2.11(a)**. After systematical studies of these vibration modes, three changing rules can be concluded as the thickness increases from monolayer to bulk MoS_2. For monolayer MoS_2, E_{2g}^1 and A_{1g} peak locate at ~384 cm^{-1} and ~405 cm^{-1}, respectively. As the layer number of MoS_2 increases, the E_{2g}^1 mode exhibits a red shift while the A_{1g} mode exhibits an opposite blue shift. Second, the frequency spacing between E_{2g}^1 and A_{1g} peaks increase as layer number increases, from ~19 cm^{-1} for monolayer sample to ~25 cm^{-1} for bulk sample. Third, the intensities of both E_{2g}^1 and A_{1g} peak increase up to four layers and then decrease as MoS_2 becomes thicker.[102]

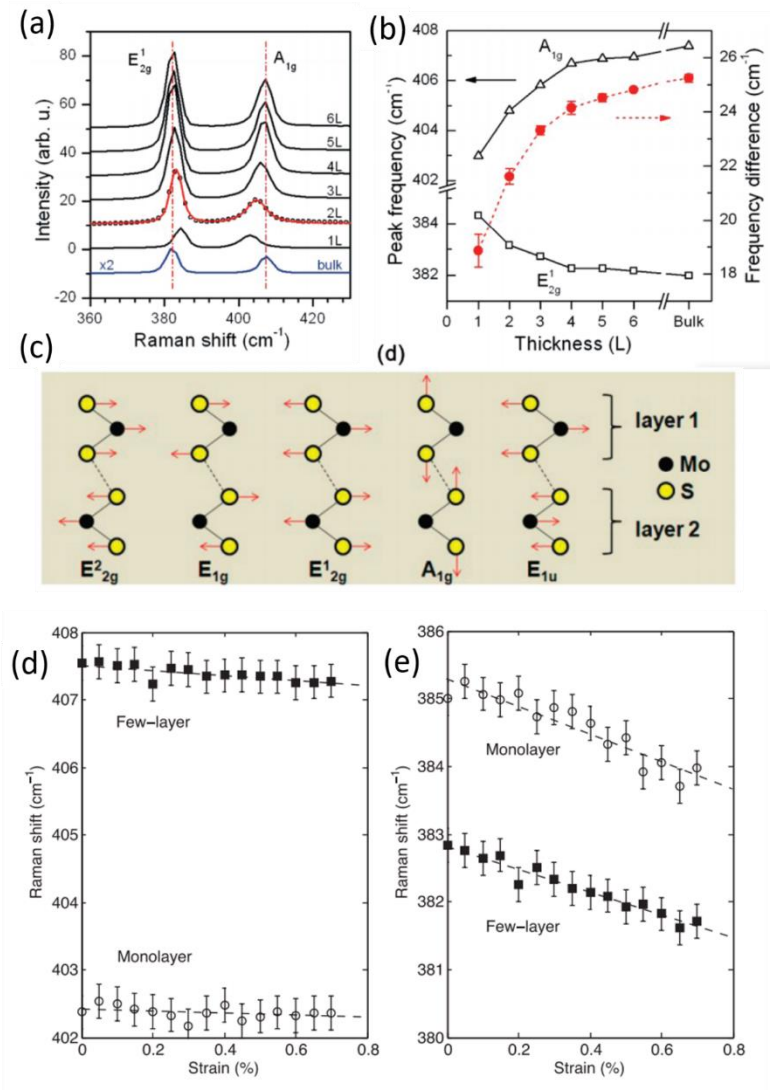

Figure 2.11. Vibration properties of MoS_2. (a) Raman spectra of MoS_2 with thickness from 1L to 6L. (b) Frequencies of E^1_{2g} and A_{1g} Raman modes and their differences as the function of thickness (c) Schematics of five possible atomic displacements in the unit cell of bulk MoS_2 crystal, including four Raman-active modes and one IR-active mode (E_{1u}). Reprinted with permission from ref. [102]. **© 2010 American Chemical Society.** (d-e) Position of the A_{1g} (d) and E^1_{2g} (e) vibration mode of monolayer (open circles) and few-layer (filled squares) MoS_2 as a function of strain. Reprinted with permission from ref. [103]. **© 2013 American Physics Society.**

Raman spectra could also indicate the level of strain in MoS_2. By applying a uniaxial strain on MoS_2, Rice et al.[103] discovered a small red shift of A_{1g} peak at a rate of 0.4 cm^{-1} per % strain for both monolayer and multilayer MoS_2. The $E_{2g}{}^1$ peak, on the other hand, exhibits a more significant red shift at a rate of 2.1 cm^{-1} per % strain for monolayer MoS_2 and 1.7 cm^{-1} per % strain for few layer MoS_2.[103]

2.3.1.1.4 Photoluminescence Emission Characteristics

In photoluminescence (PL) measurement, a semiconducting material is excited by a monochromatic light source that provides photons with energy larger than the bandgap of the semiconducting material. Once the photons are absorbed, the electrons and holes are formed with finite momenta k in the conduction and valence band, respectively. Finally, the electrons and holes recombine and emit photons. The PL peak energy of a direct bandgap semiconductors is usually called the optical bandgap. The value of optical band gap equals to the electrical band gap minus the energy required to separate the Coulomb interactions between the electrons and holes in excitons or trions.[98,104]

In the case of MoS_2, two major peaks appear in the PL spectra of MoS_2, at approximately 1.85 eV (A) and 2.05 eV (B). The A peak and B peak correspond to the direct gap transitions at K or K' point. The energy difference between A peak and B peak is caused by valence band splitting due to the strong SO interaction. When the layer number increases to two layers, a weak peak I rises. (**Figure 2.12(a)**) This is associated with the indirect bandgap transition as the structure evolves from direct bandgap (monolayer MoS_2) to indirect bandgap structure (multilayer MoS_2). As the layer number further increases, the intensity of A peak decreases, also owing to the

evolution of band structure.[105]

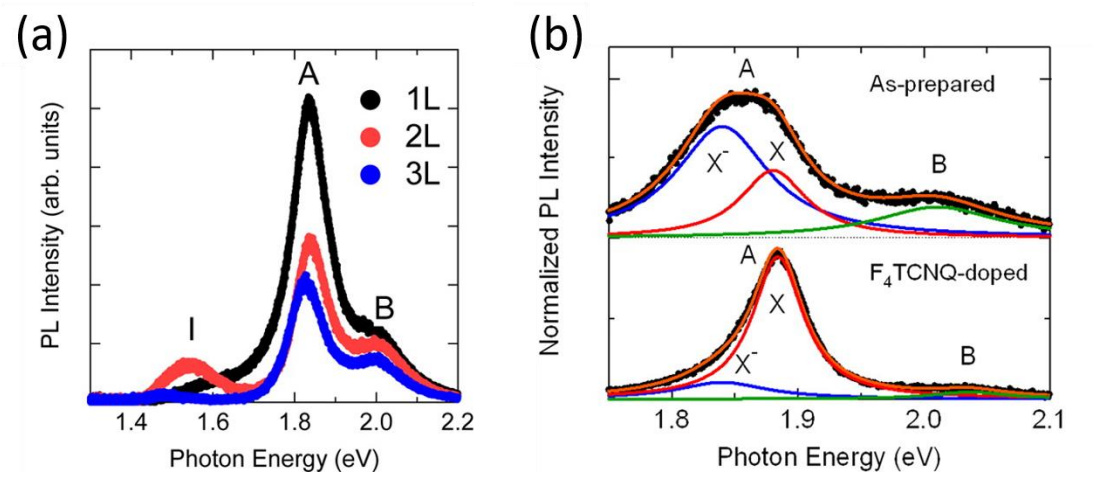

Figure 2.12. Photoluminescence spectra of MoS_2. (a) PL spectra of 1L, 2L and 3L MoS_2. (b) Analysis of the PL spectral shapes for as-prepared and F_4TCNQ-doped (p-doped) 1L-MoS_2. The A peaks in the PL spectra were multi peak fitted into two Lorentzian peaks, corresponding to trion (X^-) and exciton (X) peaks. Reprinted with permission from ref. [105]. **© 2010 American Chemical Society.**

By further analyzing the intensity ratio of subpeaks, the PL spectrum can give an insight to the doping level of single layer MoS_2. The A peak can be regarded as a combination of two subpeaks, exciton peak A (~1.88 eV) and negative trion peak A- (~1.84 eV), by multi peak fitting. The negative trion is defined as a quasiparticle made up of two electrons and a hole, which can be created optically.[105] (**Figure 2.12 (b)**) In most cases, MoS_2 samples are unintentionally electron-doped (n-doped) during sample preparation. Therefore, in the PL spectra of as-prepared MoS_2 samples, the trion peak A- is usually dominant. In contrast, when MoS_2 is p-doped, the PL spectra of MoS_2 are dominated by A peak due to decreased density of excess electrons in p-doped MoS_2 samples.[105-106]

2.3.1.2 Synthesis of MoS_2

2.3.1.2.1 Exfoliation

Like graphene, the simple "Scotch tape" method can mechanically exfoliate thin MoS_2 flakes from bulk material. This technique is suitable to isolate high quality monolayers used for intrinsic sheet production and fundamental researches but is also known for poor control of sheet size and layer number, as well as relatively low yield, which is not suitable for large scale production in practical applications.[107]

Another type of exfoliation process is through liquid phase approach, which can be further divided into two subsections: ion intercalation and solvent-based exfoliation.[83] In 2011, Zeng et al.[108] reported a highly controllable electrochemical lithiation discharge process to exfoliate MoS_2 nanosheet from bulk MoS_2. The yield of monolayer MoS_2 sheets could reach to 92%. However, the product was dominated by 1T phase metallic MoS_2. Also, in 2011, solvent-based exfoliation process known as the Coleman method was first introduced. High yield 2H-MoS_2 nanosheets could be obtained from exfoliation of bulk MoS_2 flakes using organic solvents, followed by sonication.[109] Chemical exfoliation methods could significantly increase yield comparing to mechanical exfoliation methods. Nevertheless, the sonication process involved would inevitably introduce defects and reduce flake size, which is not suitable for applications such as large-scale electronics and optoelectronics.[107]

2.3.1.2.2 Chemical Vapor Deposition

Recently, CVD approach has attracted researcher's attention because of its capability to synthesis continuous 2D MoS_2 film on a wafer-scale, which shows great potential in practical applications like large-scale integrated electronics. Currently, most works use

solid Mo based compound powders as Mo source and sulfur powder or H_2S gas as sulfur source to produce MoS_2 film.

In 2012, Lee et al.[110] reported an ambient pressure CVD (APCVD) process to grow large-area, single layer MoS_2 films on SiO_2/Si substrate for the first time. Molybdenum trioxide (MoO_3) powder and sulfur (S) powder were used as solid precursors. Before deposition, the SiO_2 substrate was pretreated by graphene-like molecules that acts as seeds for nucleation. The thickness of CVD grown monolayer MoS_2 was about 0.72 nm, measured by AFM. The result matches well with that of mechanically exfoliated monolayer MoS_2. Later, Yu et al.[111] reported a self-limiting low-pressure CVD (LPCVD) process at ~ 2 Torr pressure. By replacing the MoO_3 powder with molybdenum chloride ($MoCl_5$) as Mo source, centimeter-scale MoS_2 film with high uniformity could be produced at lower temperature. However, the $MoCl_5$ is very moisture sensitive, which is hard to preserve and process.

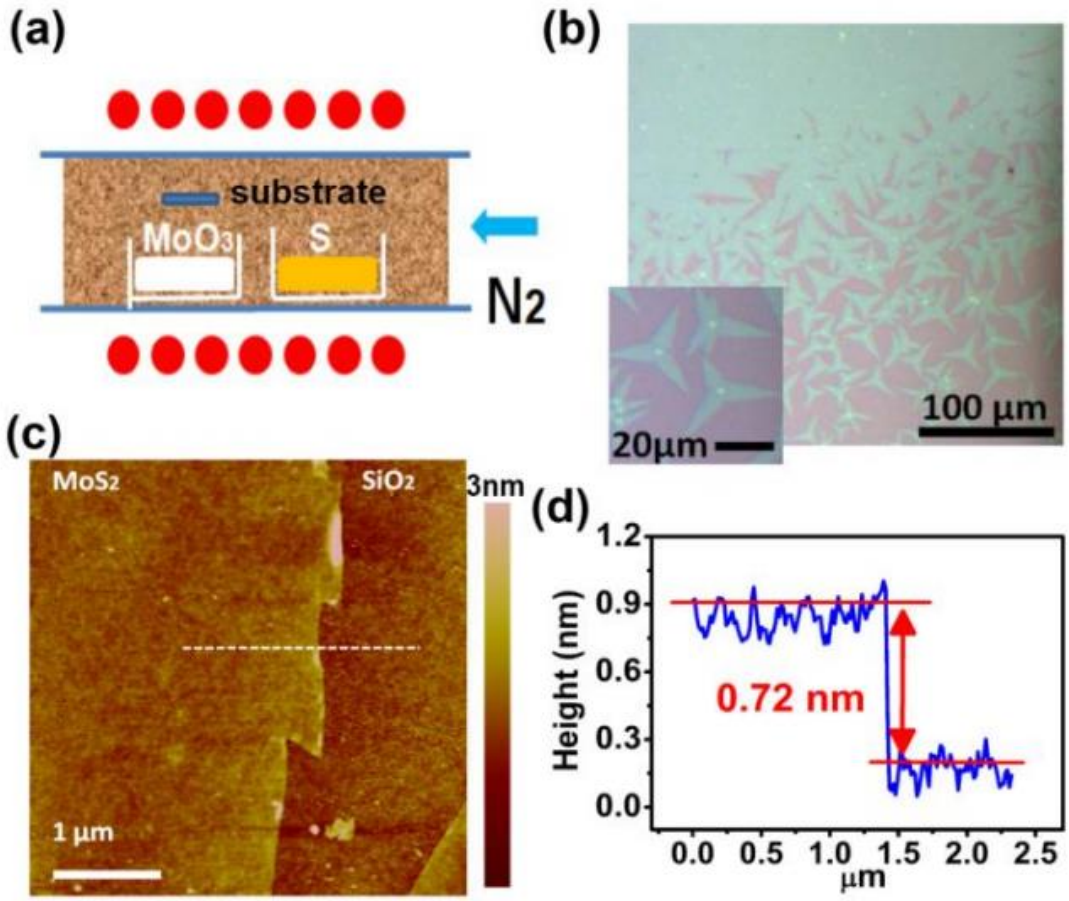

Figure 2.13. CVD growth of MoS_2. (a)Schematic illustration of one hot zone CVD setup to grow 2D MoS_2. (b)The optical image of the MoS_2 layers grown on the substrate treated with rGO solution. The inset is the magnified optical image of the MoS_2 films, showing that there is a seed located at the center of each star-shaped domain. (c) AFM image of a monolayer MoS_2 film on a SiO_2/ Si substrate (d) The AFM cross-sectional profile along the line indicated in (c) proves that the thickness of single layer MoS_2 is 0.72 nm. Reprinted with permission from ref. [110]. © 2012 **WILEY-VCH Verlag GmbH & Co. KGaA, Weinheim**

Metal-organic CVD (MOCVD) is a special case of CVD where gaseous organometallic precursors are used as metal source. In 2015, Kang et al.[112] reported a 4-inch wafer-

scale monolayer MoS_2 film deposited on SiO_2 substrate. Molybdenum hexacarbonyl ($Mo(CO)_6$) was used as Mo source and diethyl thioether ($(C_2H_5)_2S$) was used as S source. Full coverage of monolayer MoS_2 film on the substrate, without second layer nucleation, could be achieved within 26 hours. They also discovered that a low concentration H_2 addition into Ar carrier gas could be beneficial for the growth as H_2 aids the decomposition of $(C_2H_5)_2S$, while a higher H_2 concentration may etch MoS_2.[112] This method is promising to produce large scale monolayer MoS_2 film in modern semiconductor industry, but it should also be noticed that $Mo(CO)_6$ is very toxic, which needs extra attention in the laboratory.

2.3.1.2.3 Atomic Layer Deposition

Atomic layer deposition (ALD) could be regarded as a subclass of CVD.[107] Different from CVD techniques, in ALD processes the ultrathin film is formed by exposing the substrate surface to alternating gas reactants. Different precursors never present in the chamber simultaneously. Instead, they are transported into the reaction chamber as non-overlapping and sequential pulses with purge stages in between. In each pulse, the deposition and reaction of molecules have a self-limiting behavior, which enables precise thickness control via layer-by-layer deposition.[107] Successful ALD of MoS_2 has been reported using $MoCl_5$ with H_2S,[113] and $Mo(CO)_6$ with H_2S[114-116] or dimethyl disulfide.[117-118]

2.3.1.2.4 Transfer of MoS_2

Like graphene, the as synthesized MoS_2 samples are expected to be transferred onto other substrates for further characterization and device fabrication. Due to the nature of

2D materials, the transfer method developed for MoS_2 is quite similar to that of graphene. A polymer supporting layer is usually required to maintain the integrity of MoS_2 samples during the transfer process. For wet transfer route, PMMA is usually used as buffer layer. The substrate is etched away by proper etchant solution. For instance, NaOH/NaF or NaOH solution are generally used for sapphire substrate[119-120] and KOH are widely used for SiO_2/Si.[121-122] The PMMA/MoS_2 stack is subsequently scooped out and transferred onto a new substrate. For dry transfer method, PDMS or TRT is used as the polymer scaffold. Followed by etching and cleaning process, the polymer/MoS_2 stack is stamped to a new substrate.

2.3.2 Tungsten Disulfide (WS_2)

2.3.2.1 Properties of WS_2

2.3.2.1.1 Mechanical Properties

For applications like flexible and stretchable electronics and optoelectronics, elastic modulus is an important figure of merit. Like MoS_2, 2D WS_2 exhibits outstanding mechanical properties, which has been measured by the AFM method mentioned above. The CVD-grown monolayer WS_2 was reported to have a 2D elastic modulus as high as 177 ± 12 Nm^{-1}, almost half of that of graphene (~ 340 Nm^{-1}).[97] This makes 2D WS_2 a potential candidate in flexible devices applications.

2.3.2.1.2 Electronic Properties

The fundamental band structure physics of WS_2 is very similar to MoS_2.[123] **Figure 2.14(a)** and **(b)** are the theoretical band structures of bulk WS_2 and monolayer WS_2, calculated by DFT. In bulk WS_2, the smallest indirect bandgap is from the VBM at the

Γ point of Brillouin zone to the CBM at T symmetry point, halfway between Γ and K. As the layer number of WS_2 decreases, the conduction band at K point almost remains still, while the conduction band at T point gradually shifts upwards. When the thickness further reduces to single layer, the energy required for indirect transition exceeds the direct transition, which results in the transition from indirect bandgap structure to direct bandgap at K point. The optical indirect bandgap of bulk WS_2 is ~ 1.3 eV and the direct bandgap of monolayer WS_2 is about 2.1 eV.[91]

In bulk WS_2, the valence band splits at K point, leading to two direct transition at K point. This derives from the interlayer coupling between WS_2 monolayers, which has been proved by observation of so-called A excitons at 1.95 eV and B excitons at 2.36 eV.[124] As interlayer coupling is absent in monolayer WS_2, this feature cannot be observed in monolayer WS_2.

Numerous studies have been done on measuring the electron mobility of exfoliated WS_2 samples, as illustrated in **Figure 2.14 (c)**. It has also been reported that by transferring onto hexagonal boron nitride (h-BN) substrate the electron mobility of WS_2 could significantly enhance.[95,126-127]

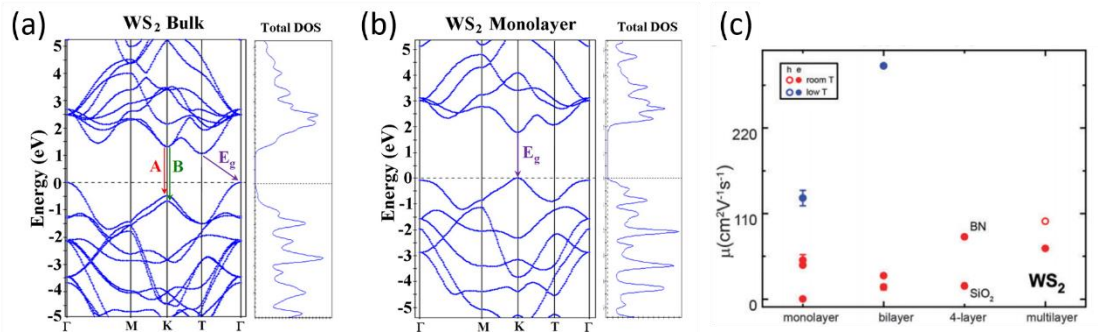

Figure 2.14. Electronic properties of WS_2. (a-b) Simulated band structure and total density of states (DOS) of bulk WS_2 (a) and monolayer WS_2 (b). Reprinted with permission from ref. [91]. **© 2012 American Chemical Society. All rights reserved.** (c) Reported carrier mobility values of monolayer and multilayer WS_2 at room temperature or low temperature. Reprinted with permission from ref. [95]. **© 2015 The Royal Society of Chemistry. All rights reserved.**

2.3.2.1.3 Vibration Properties

Same as MoS_2, there are two prominent first-order vibration modes in the Raman spectra of WS_2: E_{2g}^1 and A_{1g}, corresponding to in-plane vibration and out-of-plane vibration, respectively.[128-129] **Figure 2.15(a)** and **(b)** show two Raman spectra of single layer WS_2 obtained using 514.5 nm and 488 nm laser excitation. In the Raman spectrum with 488 nm excitation, the first order and second-order longitudinal acoustic modes at the M point of the Brillouin Zone, known as the LA(M) and 2LA(M) peak, can be detected in addition to E_{2g}^1 and A_{1g} peaks. In the Raman spectrum using 514.4 nm laser excitation, numerous other second-order peaks could be observed. It should be noticed that the intensity of 2LA(M) becomes very strong under 514.5 nm excitation, owing to a double-resonant Raman process that only occurs in monolayer WS_2.[128] As a result, it

is easy to distinguish monolayer WS_2 from few-layer WS_2 by the intensity ratio of 2LA(M) and A_{1g} at 514.5 nm excitation.

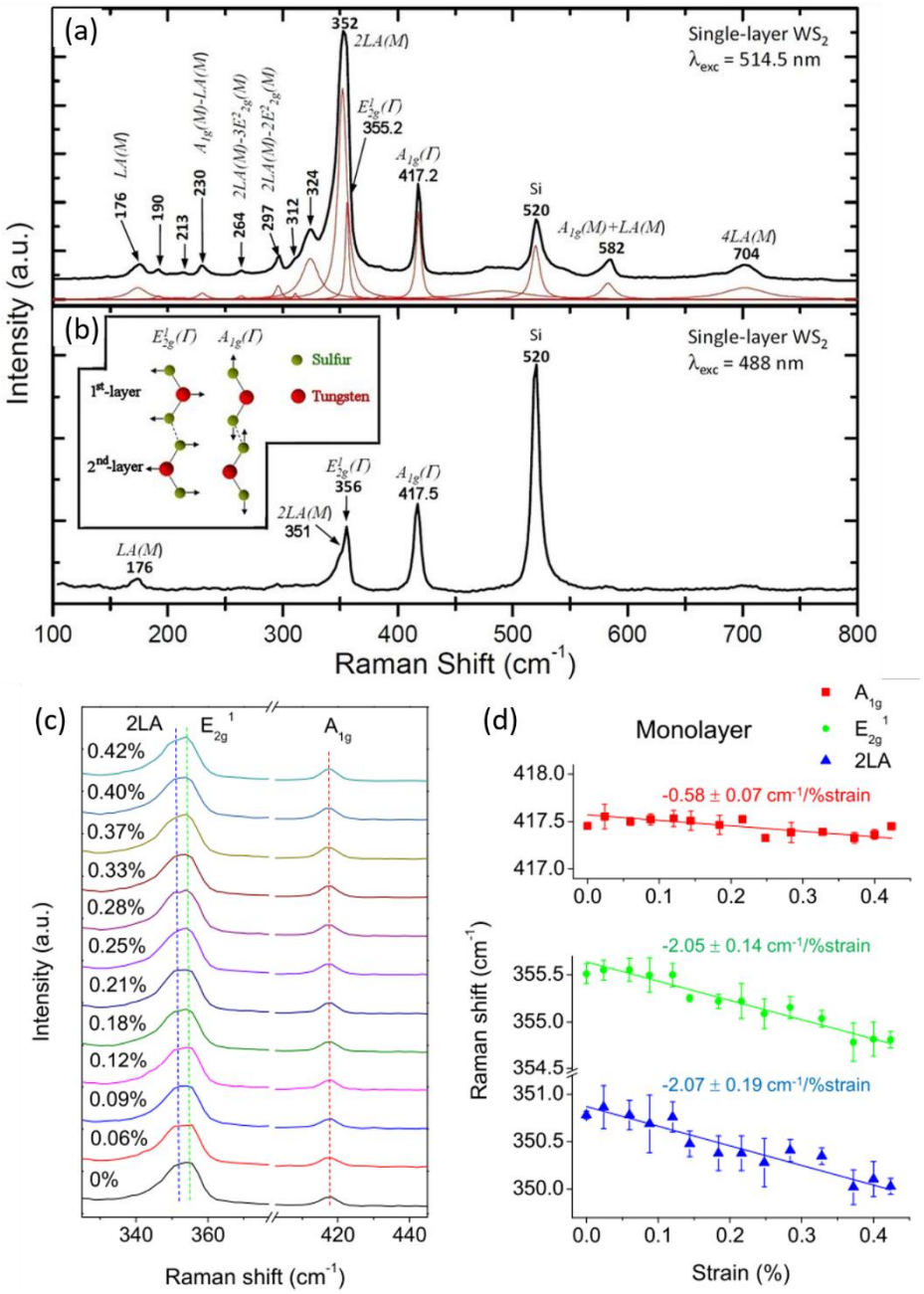

Figure 2.15. Vibrational properties of TMDs. (a-b) Raman spectra of single layer WS_2 under 514.5 nm (a) and 488 nm (b) excitation. ref. [128]. Reprinted with permission from © **2013 Macmillan Publishers Limited.** All rights reserved. (c) Evolution of the A_{1g}, $E_{2g}{}^1$ and 2LA Raman modes during the deformation of a WS_2 monolayer. (d) Raman frequencies of A_{1g}, $E_{2g}{}^1$ and 2LA bands as a function of strain. ref. [130]. Reprinted with permission from © **2016 IOP Publishing Ltd.**

The interlayer interactions can easily influence the position of A_{1g} peak. As the layer number increases, the A_{1g} peak blue-shifts while E_{2g}^1 and 2LA (M) peak almost remain unchanged. On the other hand, the E_{2g}^1 and 2LA peak are sensitive to lattice strain in monolayer WS_2. The position of E_{2g}^1 and 2LA modes exhibit a red/blue shift enacted under a tensile/compressive strain, as illustrated in **Figure 2.15(c)** and **(d)**.[130]

2.3.2.1.4 Photoluminescence Emission Properties

Similar to MoS_2, the as prepared 2D WS_2 flakes are usually negatively doped, which suggests that there are three possible quasiparticles, A exciton, B exciton and A- trion, in the PL spectra of WS_2. However, as is mentioned in section 2.3.2.1.2, B exciton is absent in monolayer WS_2. Therefore, there is only one predominant A peak locating at ~1.98 eV in the PL spectrum of monolayer WS_2, with a A- trion peak, which can be distinguished by multi peak fitting, locating at the lower energy side of A exciton peak.[120,131-133] (**Figure 2.16(c)**) The binding energy of trion in monolayer WS_2 is around 20-45 meV.[134] In experimental measurements, the binding energy can vary a lot as it is sensitive to a variety of factors including dielectric environment, laser excitation power and doping level.[135-137] Comparing to monolayer WS_2, the PL intensity of bilayer WS_2 is much weaker due to its indirect bandgap nature, making it possible to distinguish the thickness of WS_2. Besides, the experimental measurements suggest that monolayer WS_2 has a PL quantum yield of ~ 6%, highest among 2D semiconducting TMDs. This is due to its relatively high thermodynamic stability and low defect density.

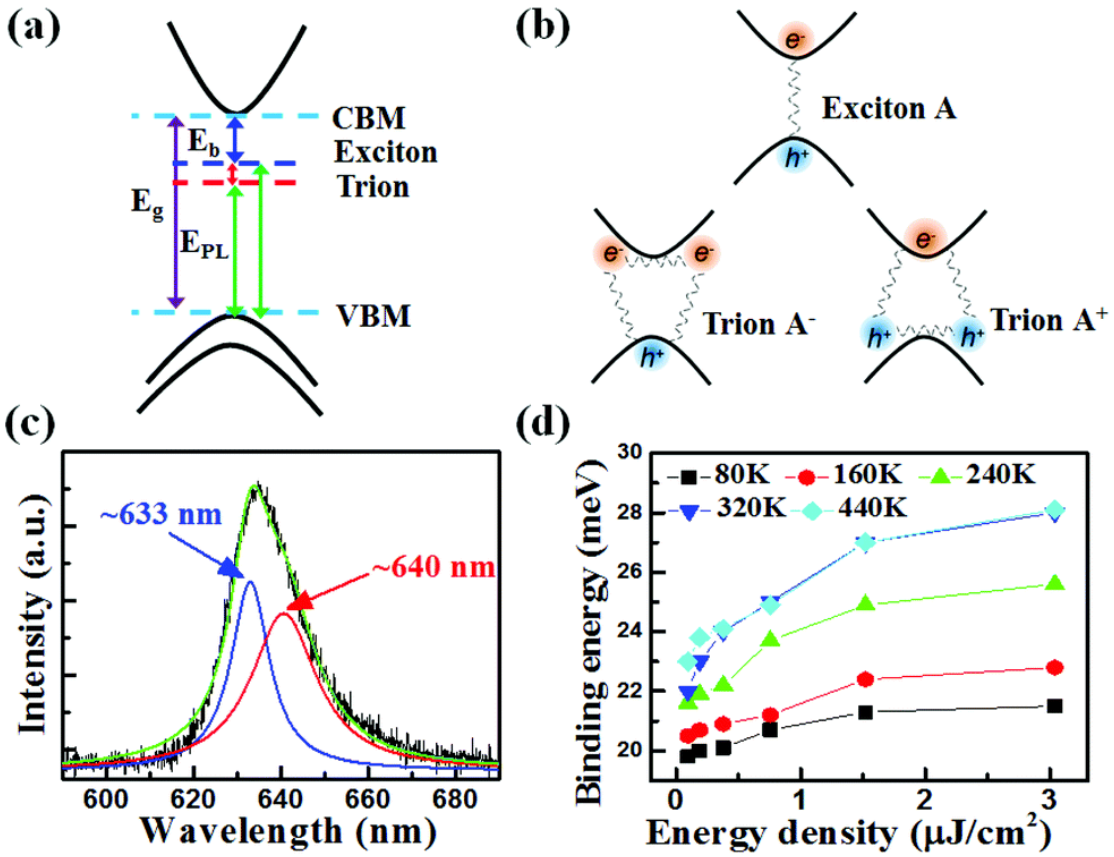

Figure 2.16. Photoluminescence properties of WS2. (a-b) Schematics for the energy level and the model of excitons and trions in 2D WS_2. (c) PL spectrum of the monolayer WS_2 measured at room temperature, fitted with two Lorentzian peaks that attribute to excitons (633 nm) and trions (640 nm). (d) the energy difference between exciton peak and trion peak at different excitation energies and different temperatures are presented in (d). ref. [135]. Reprinted with permission from © **2017 The Royal Society of Chemistry**

2.3.2.2 Synthesis of WS_2

2.3.2.2.1 Exfoliation

The "Scotch tape" method can also apply to mechanically isolate atomically thin WS_2 flakes from bulk WS_2 crystals. The bulk crystals are commonly synthesized using

chemical vapor transport (CVT) technique.[138] A typical CVT process involves vaporization and recrystallization under new equilibrium conditions, which would likely to take days or weeks to complete. The advantage of CVT is that it can produce high purity, single-crystalline pristine crystals, which could reduce the number of defects and impurities in exfoliated 2D materials. Mechanical exfoliation technique enables the study of intrinsic properties of monolayer WS_2,[139] but the low-yield nature of mechanical exfoliation process makes it not suitable for scalable production.

Like other TMDs, 2D layered WS_2 can be chemically exfoliated by organic solvents,[109] and aqueous surfactant solutions. [140] It is possible to generate large quantity of exfoliated sheets with liquid-phase exfoliation method but the random thickness and limited flake size (sub-micron) hinders its viability for large scale device fabrication. To overcome this drawback, researchers introduced the intercalation-based exfoliation method. The principle is to insert species between layers, which weakens the interlayer interaction and thus reduces the energy barrier required to exfoliate.[141-143] Using lithium ion as intercalation species, sub micrometer-sized monolayer WS_2 flakes can be produced. However, the resulting products may have changed phases (e.g. from 2H to 1T phase), which is not ideal for applications in electronic devices.[144-145]

2.3.2.2.2 Chemical Vapor Deposition

Unlike exfoliation methods, the CVD approaches show great potential to meet the industrial requirement for mass production of large area, high quality WS_2. There are basically three routes: sulfurization of metal or metal oxide, powder vaporization and MOCVD.

The sulfurization method contains two steps. First, the W-based precursors, usually WO_3, are coated on the substrate. Then, the transformation into WS_2 is achieved through exposure to sulfur vapor at high temperature.[146] WO_3 thin film can be deposited using various technique, including thermal evaporation,[147] RF-sputtering,[148] and ALD.[149] By controlling the thickness of WO_3 film, the thickness of WS_2 can be precisely controlled.[148] The sulfurization routes are appropriate for growing continuous wafer-scale WS_2 film, but the grain size is generally limited to sub micro scale, which hinders its applications in the devices due to poor electrical performance.

The powder vaporization processes are typically achieved via chemical vapor reaction. A typical setup involves a quartz tube placed in a horizontal furnace, with the WO_3 powder positioned at the hot zone of the furnace and S powder placed at the low temperature upstream of WO_3. The substrates can either be placed face down above the WO_3 precursor or at the downstream of WO_3 powder. [150] The first successful attempt on the chemical vapor reaction growth of monolayer WS_2 was an APCVD process. Perylene-3,4,9,10-tetracarboxylic acid tetrapotassium salt (PTAS) was used as seeding to improve the nucleation of WS_2 domains. The size of as-grown WS_2 domains was measured to be ~ 10 μm.[150] Later, Zhang et al.[120] reported a LPCVD process to grow WS_2 monolayer domains on sapphire substrate. The domain size could be improved to 50 μm. To further increase the domain size, Cong et al.[151] proposed a one hot zone APCVD setup, as is illustrated in **Figure 2.17(a)**. Before the reaction, WO_3 powders were deposited onto one of the SiO_2/Si chips and while the other SiO_2/Si chip was placed face down on top of it, as the substrate. The size of single WS_2 domain could

reach up to 178 μm. In addition, introduction of hydrogen in the system could help to form continuous films of WS_2 instead of separate single domains. Kang et al.[152] and Sheng et al.[153] reported H_2 addition in LPCVD and APCVD process, respectively. The H_2 addition would reduce the size of single WS_2 domains but dramatically increases the nucleation density. Continuous polycrystalline monolayer WS_2 film up to cm^2 size could be achieved with these methods.

Generally, CVD process is very promising in synthesis of large WS_2 domains and continuous WS_2 film for device fabrication. However, this method often suffers from poor control of the vaporization rate of solid precursors, which may cause a morphology gradient in the product. For instance, more WS_2 domains tend to deposit in the upper stream region of the substrate than in the downstream region.

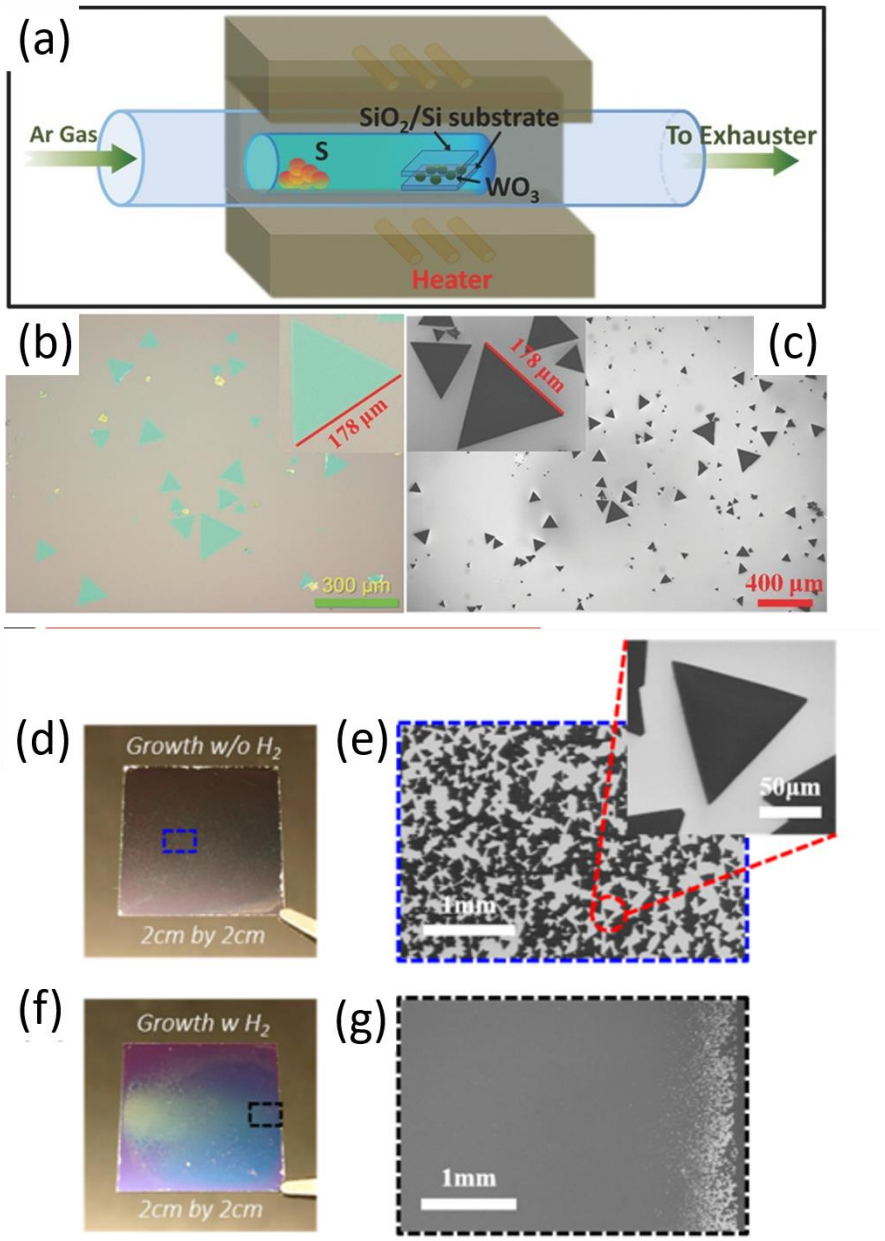

Figure 2.17. CVD synthesis of WS_2. (a) Schematic illustration of CVD setup with two stacked substrates. (b) Optical and (c) SEM image of as-grown WS_2 domains on SiO_2/Si substrate. ref. [151]. Reprinted with permission from © **2013 WILEY-VCH Verlag GmbH & Co. KGaA, Weinheim.** (d) Optical image and (e) SEM image of as-grown WS_2 using Ar as carrier gas. (f) Optical image and (g) SEM image of as-grown WS_2 with addition of H_2 into the system. ref. [153]. Reprinted with permission from **© 2017 American Chemical Society**

By controlled introduction of chemical or molecular precursors into the hot zone of the furnace, the MOCVD technique shows great potential for an industrialized scalable synthesis of WS_2. Using $W(CO)_6$ and $(C_2H_5)_2S$ as gaseous precursors, Kang et al. [112] reported a MOCVD growth, with addition of H_2, to produce high quality WS_2 film on 4-inch SiO_2/Si wafer. The monolayer WS_2 film exhibited high uniformity over the entire 4-inch wafer. The electron mobility of WS_2 FETs fabricated by the WS_2 film could reach up to 18 $cm^2 V^{-1}s^{-1}$ with an on/off ratio up to 10^6.

2.3.2.2.3 Atomic Layer Deposition

Like MoS_2, high quality WS_2 can also be synthesized by ALD. Groven et al.[154] reported successful synthesis of 2D WS_2 with plasma enhanced ALD (PEALD) on SiO_2 or Al_2O_3 substrate, using WF_6, H_2 plasma and H_2S as precursors. The PEALD has a two-step reaction cycle, composed of H_2 plasma exposure and H_2S exposure with presence of WF_6. The reduction and oxidation of the W happened during H_2 plasma and H_2S reaction process, respectively.[154] Although PEALD can synthesize large area continuous WS_2 film, the domain size of WS_2 is usually very small (<200 nm), which hinders its application in electronics and optoelectronics.

2.3.2.3 Transfer of WS_2

The transfer method for WS_2 is very similar to MoS_2 and other TMDs, which has been discussed in section 2.3.1.3.

2.4 Gallium Sulfide (GaS)

Monolayer transition metal dichalcogenides have attracted great interest over the past

decade, thanks to their unique mechanical and physical properties. The post-transition metals of group III and V have monochalcogenide form of MX, where M stands for Indium (In), gallium (Ga) and X stands for S, Se. Similar to TMDs, these monochalcogenides also have layer-by-layer structures and can be exfoliated into 2D form.[154] These 2D monochalcogenides present unique physical properties that shows potentials in various applications such as transistors,[155] photodetectors,[156] energy storage,[157] gas sensing,[158] and application as hydrogen evolution catalysts.[159]

Gallium sulfide (GaS) is one of the 2D monochalcogenides that has been investigated recently. Bulk GaS crystal consists of vertically stacked single layer GaS, held together by van der Waals interaction. The thickness of single layer is ~7.5 Å. In single layer GaS, two bonded gallium atoms are sandwiched by two layers of sulfur atoms. The unit cell of GaS is a hexagonal crystal structure composed of two layers of GaS.[160] Unlike other widely studied 2D materials, 2D layered GaS has an indirect bandgap ranging from 2.6 eV for monolayer GaS to 1.8 eV for bulk GaS, according to first principle calculations.[161] This bandgap of 2D GaS corresponds to emission wavelength of blue light. The large bandgap of GaS is unique in other most widely studied 2D materials, which is either smaller, including MoS_2 and WS_2, or much larger such as insulating hexagonal boron nitride (hBN).[162-163] Therefore, GaS is considered as a promising building block in ultrathin electronics and optoelectronics, especially in applications like blue LEDs and UV photodetectors, which other 2D materials cannot competent.

2.4.1 Properties of GaS

2.4.1.1 Electronic Properties

The bulk GaS crystal has an indirect bandgap shown in **Figure 2.18(a)**. The CBM and VBM locate at the M and Γ, respectively. The theoretical bandgap of bulk GaS is about 1.8 eV. When the thickness reduces to monolayer, the CBM of 2D GaS remains at the M point, while the valence band dramatically changes. Two symmetrically split VBM could be observed.[156] (**Figure 2.18(a)**) The indirect bandgap of monolayer GaS is calculated to be 2.61 eV, significantly larger than the indirect bandgap of bulk GaS. The value is slightly smaller than the optical bandgap of 3.05 eV, probably from the gap underestimation by DFT.

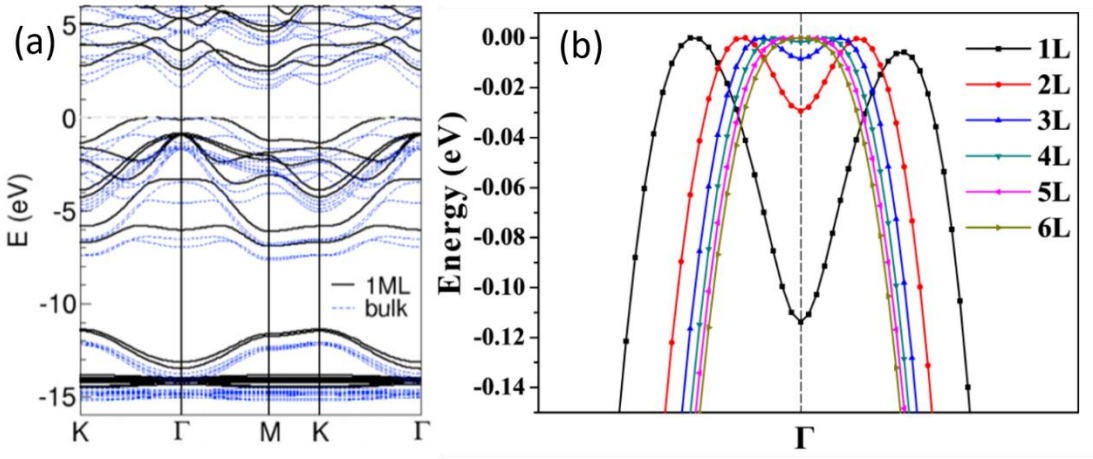

Figure 2.18. Electronic band structure of GaS. (a) Simulated band structure of monolayer and bulk GaS. ref. [156]. Reprinted with permission from **© 2013 American Chemical Society** (b) The evolution of valence band maxima (VBM) of layered GaS near the Γ point (dashed line) as a function of layer number. ref. [161]. **Reprinted with permission from © Tsinghua University Press 2015**

Figure 2.18(b) illustrates the effect of layer numbers on the VBM, from monolayer to 6 layers. The monolayer GaS exhibits the largest VBM split of 6.1 meV. When the layer

number increases, the two VBM shifts towards to Γ point. At the thickness of 5 layers, the VBM splitting is negligible and the band structure is very similar to bulk GaS.[161]

2.4.1.2 Vibration Properties

Like TMDs, the Raman spectroscopy is an effective technique to characterize the structural evolution of layered GaS. In the Raman spectra of layered GaS, there are three first-order phonon modes, one in-plane mode known as E_{2g}^1 and two out-of-plane modes known as A_{1g}^1 and A_{1g}^2, respectively. When using 532 nm laser as excitation light source, the E_{2g}^1 mode locates at ~ 300 cm^{-1}. However, when GaS is deposited on SiO_2/Si substrate, the E_{2g}^1 mode is nearly undetectable, owing to strong SiO_2/Si peak at 303 cm^{-1}. The A_{1g}^1 and A_{1g}^2 peak, on the other hand, can be easily distinguished, which could help to identify the evolution of layered GaS as a function of thickness. For monolayer GaS, the intensities of A_{1g}^1 and A_{1g}^2 peak are very weak and locates at 182 cm^{-1} and 360 cm^{-1}, respectively. As the thickness increases, the A_{1g}^1 gradually shifts to larger wavenumber until 188 cm^{-1} for bulk GaS, whereas the A_{1g}^2 mode remains at 360 cm^{-1}. The intensities of A_{1g}^1 and A_{1g}^2 peak both increase significantly as the layer number increases. The Raman spectroscopy provides an easy technique to determine the thickness of layered GaS.[156,162,164]

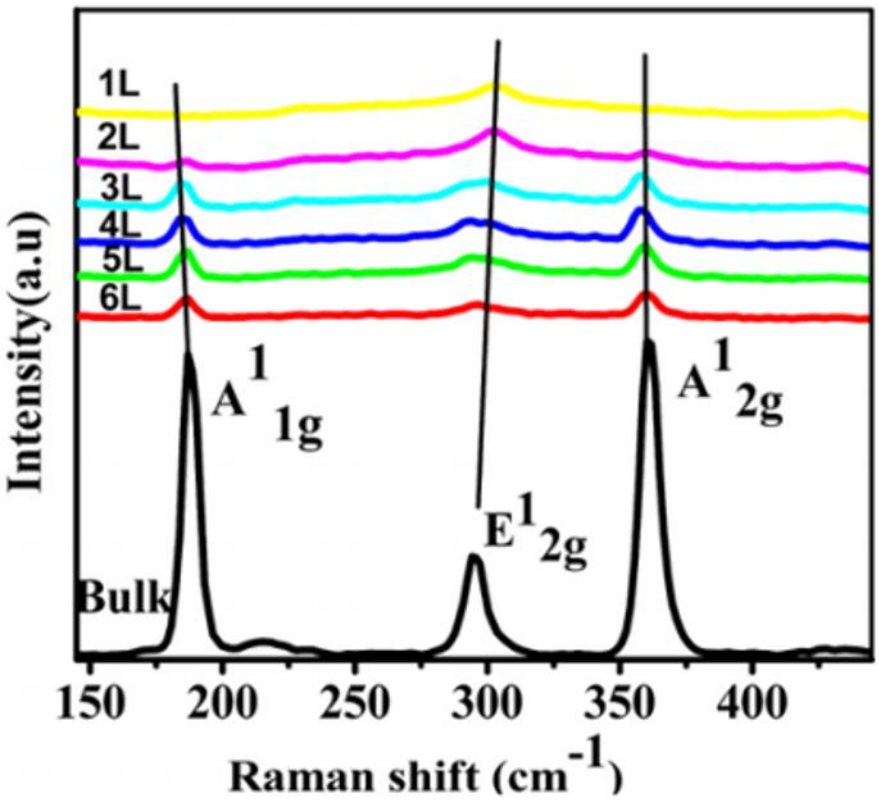

Figure 2.19. Vibrational properties of GaS. The Raman spectra of bulk GaS and 2D GaS with layer number from 1L to 6L. ref. [156]. Reprinted with permission from © **2013 American Chemical Society**

2.4.2 Synthesis of GaS

The crystals of bulk GaS are composed of 2D single layer GaS. They can be easily mechanically or chemically exfoliated like other layered materials. In 2014, Yang et al.[158] presented isolation of few layer GaS by micromechanical cleavage technique. The bulk GaS crystal was repeatedly peeled and eventually transferred on SiO_2/Si substrate. The thickness of the exfoliated GaS nanosheets was measured to be 4.5 nm, corresponding to ~6 layers. A single sheet of GaS was fabricated into a photodetector via depositing two metal bond pads on it. The electron mobility was measured to be ~

0.1 cm^2 $V^{-1}s^{-1}$ with an on/off ratio in the range of ~10^4 to 10^5. Hu et al.[156] reported a similar study on exfoliated GaS nanosheets. The bulk GaS laminar precursor was first synthesized using a two hot-zone horizontal setup with a fused silica tube. Sulfur powder and gallium powder were used as reactants. The few layer GaS nanosheets were then exfoliated using solvent exfoliation or mechanical cleavage method. The photoresponsivity and external quantum efficiency (EQE) of the as exfoliated GaS nanosheet were measured at various wavelength excitation, maximizing to 19.2 AW^{-1} and 9373%, respectively, at 254 nm. Although mechanical and chemical exfoliation can easily and quickly produce highly crystalline single and few layer GaS nanosheets, scalable manufacture of high-quality uniform GaS for device fabrication is still difficult to achieve by exfoliation techniques.

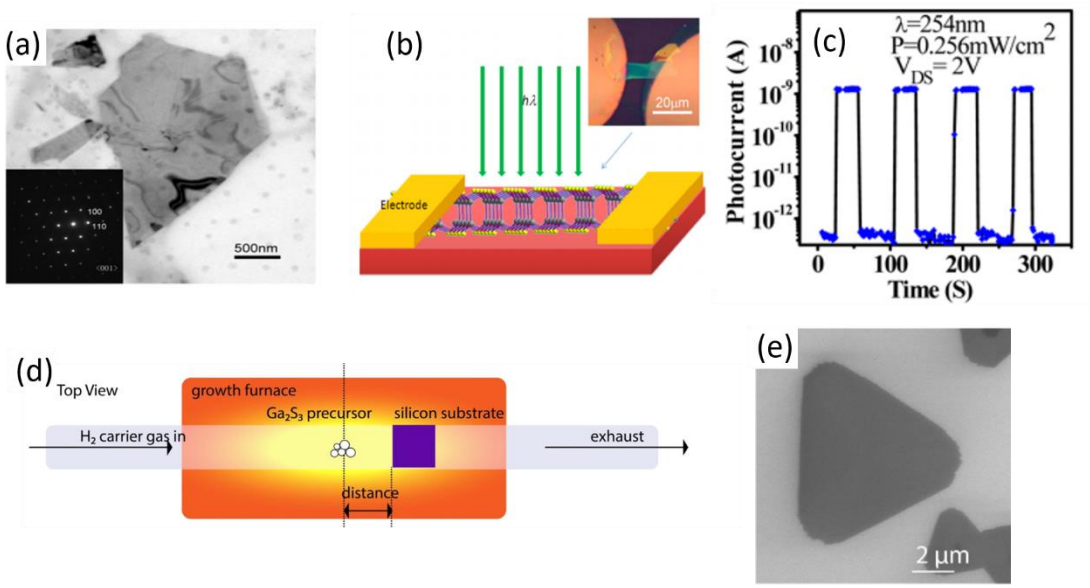

Figure 2.20. Synthesis of GaS. (a) Low-resolution TEM image of exfoliated layered GaS nanosheets. (b) Schematic of a typical GaS photodetector. The inset image is the optical image of an actual device; (c) Time resolved photocurrent under pulse 254 nm excitation at bias voltage of 2 V. ref. [156]. Reprinted with permission from **© 2013 American Chemical Society**. (d) Schematic of one hot zone setup for CVD growth of GaS. (e) SEM image of a single GaS domain on SiO_2/Si substrate. ref. [167]. Reprinted with permission from **© 2018 American Chemical Society**

Comparing to exfoliation methods, CVD is generally regarded as a more promising technique to produce large-area and high-quality 2D GaS. Researchers have developed several CVD processes using a variety of precursors to synthesize ultrathin GaS. Date back to 1992, Barron et al.[165] first reported CVD synthesis of polycrystalline GaS thin film with gallium chalcogenide cubane $[(t\text{-Bu})GaS]_4$ as the single-source precursor. Later in 2009, Zhou et al.[166] demonstrated successful synthesis of GaS nanostructures with a variety of morphologies, including nanowires, nanobelts, hexagonal microplates,

etc. GaN and Bi_2S_3 were used as gallium source and sulfur source. The reaction used a vapor-solid method, performed at 1170 °C. Recently, Wang et al.[167] reported CVD synthesis of large area, continuous monolayer GaS film on SiO_2/Si substrate by hydrogen reduction of Ga_2S_3 powder precursor. The region of uniform film could reach sub-centimeter level, which shown possibility to fabricate high quality GaS based devices and potential in large scale implementation.

2.5 Optoelectronics Based On 2D materials

Photodetector is regarded as one of the most important fundamental building blocks in optoelectronics. Being capable of converting light signals into electrical signals, photodetectors has wide applications in novel technologies including environmental monitoring, remote sensing, video imaging and night vision devices, etc.[168-170] Until now, the commercial photodetector market has been dominated by traditional semiconductor materials, for example Si, InGaAs and HgCdTe, owing to their scalable production, mature integration technologies and excellent performance.[171-172] However, these materials are not suitable for flexible devices. On the other hand, after decade's research the family of 2D materials has been expanded significantly. 2D semiconductors with various bandgap have been successfully isolated and studied.[173] (**Figure 2.21**) Due to their unique physical properties like atomically thickness, high flexibility and excellent transparency, these 2D semiconductors have great potential in next generation flexible and transparent optoelectronics devices.

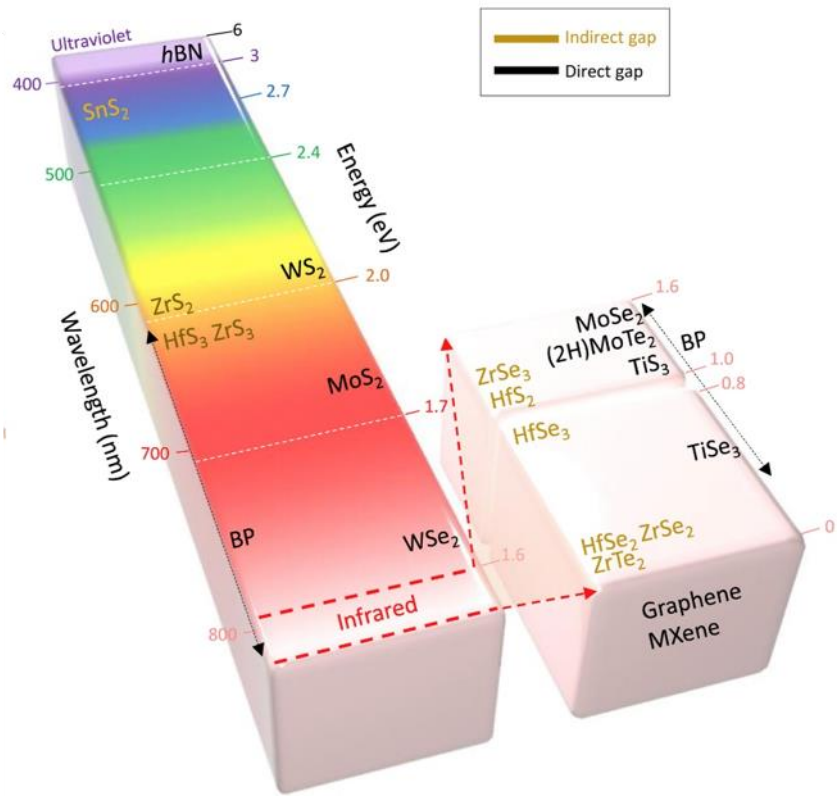

Figure 2.21. Bandgaps of 2D materials. Electromagnetic spectrum illustrating the bandgaps of 2D materials, ranging from infrared to UV region. ref. [173]. Reprinted with permission from **© 2016 Elsevier Ltd.**

2.5.1 Phototransistor- Photoconductive effect

Phototransistor is regarded as the simplest form of photodetector.[90] For 2D materials, a typical phototransistor is composed of a 2D semiconducting material channel and two contacts attached to the opposite ends of the channel. The contacts are generally conductive, serving as source and drain electrodes. When the channel is in dark state, only a small current flow can pass the channel. On the other hand, when the channel is illuminated, the current flow increases. This phenomenon is known as the photoconductive effect. When photons are absorbed by the semiconducting 2D material,

excess free carriers, both electrons and holes, are generated, increasing the effective charge carrier density and reducing the resistance of semiconductor channel. Usually, the output current under a constant bias increases with raising excitation power, as shown in **Figure 2.22(b)**.[90]

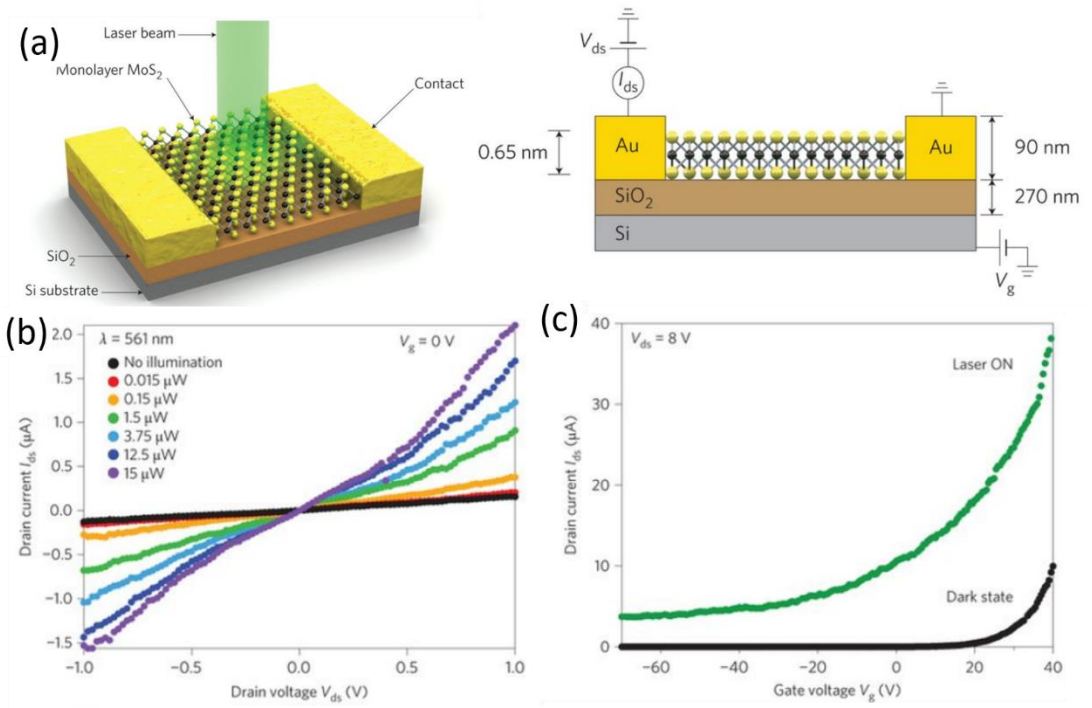

Figure 2.22. Photoconductive effect in phototransistors. (a) Schematics of the top view (left) and side view (right) of a typical metal/MoS_2/metal phototransistor. (b) I-V characteristics of single layer MoS_2 phototransistor in dark and under 561nm excitation with different intensities. (c) I-V_g characteristics of MoS_2 phototransistor in dark and under illumination. ref. [90]. Reprinted with permission from **© 2013 Macmillan Publishers Limited. All rights reserved**

To characterize the detection performance of phototransistors, photoresponsivity (R) is introduced to describe how the photodetector responds to illumination. The

photoresponsivity is defined as the photocurrent divided by the incident illumination power., shown as the following equation:

$$R = \frac{I_{photo}}{P_{light}}$$

Different from the photocurrent, which increases with incident excitation power, the photoresponsivity usually decreases with increasing incident excitation power. This can be explained that as the density of electrons holes increases under stronger illumination, the possibility of carrier recombination and trap state saturation also rises.[174]

Photogating effect is another example of the photoconductive effect, which both effects could occur simultaneously on the same device. The photogating effect is related to the presence of localized trap states like surface adsorbates and structural disorder.[175] As optical excitation generates electron-hole pairs in the semiconducting channel, either electrons or holes can be trapped in the localized states, acting as a local gate that can influence the Fermi level in 2D semiconductors. [176] This phenomenon often leads to a high external quantum efficiency (EQE), defined as the number of charge carriers contributed to photocurrent divided by the number of incident photons. On the other hand, the photogating effect also brings drawbacks. The photogating effect may be responsible for the hysteresis loop of output I-V characterization during source-drain sweeps. Another big problem is that the response time during light-dark switching may be slower as it takes time for carriers to escape from the traps.

The photoconductive effect often leads to a high photogain in 2D phototransistors. The photogain could be physically explained as the recombination lifetime of minority carriers divided by the transit time of charge carrier travelling across the semiconductor

between the two electrodes of the device. In other words, if the transit time is much shorter than the recombination time of photogenerated electron-hole pairs, the device would have a high intrinsic photogain. Therefore, the high mobility 2D materials could be good candidates to produce high gain photodetectors. [177]

2.5.2 Photodiodes-Photovoltaic Effect

Photodiode is another common type of the photodetector, operated by a so-called photovoltaic effect.[178] In a typical photodiode, a p-type semiconductor and a n-type semiconductor are connected together, forming a built-in electric field at junction interface. The built-in electric field separates the photogenerated electron-hole pairs and extracts them to opposite direction. The 2D p-n junctions are different from traditional bulk p-n junction. They can be easily tuned by external gate voltage owing to weak screening effect from ultrathin thickness.

MoS_2 is one of the most widely studied n-type 2D semiconductors,[178-179] and WSe_2 is one of the well-known p-type 2D semiconductors.[180] **Figure 2.23(a)** shows a typical 2D p-n junction made by vertically stacking MoS_2 and WSe_2. The Al and Pt bond pads are deposited onto MoS_2 and WSe_2, respectively, in order to further improve the n-type and p-type characteristics. In dark state, the I-V characteristic curves of WSe_2/MoS_2 p-n junction present a gate-dependent rectifying behavior. When the device is illuminated, the electrons can be effectively injected into n-type MoS_2 whereas the holes injected into p-type WSe_2. The heterojunction exhibits photovoltaic response that can also be tuned by applying gate voltage. (**Figure 2.23(b)**) **Figure 2.23(c)(ii)** exhibits the spatial photocurrent map, proving that photovoltaic response is primarily generated at the

overlapping area of MoS_2 and WSe_2. This can be explained by the fast separation of photogenerated electron-hole pair at the interface of MoS_2/WSe_2 p-n junction, combined with an efficient lateral transportation of electrons and holes, as is illustrated by the lateral band diagram in **Figure 2.23(d)**. It should also be noticed that by inserting additional graphene layers into TMD/metal interface, the photoresponsivity can be increased from 2 mA/W to 10 mA/W, probably caused by more effective collection of photogenerated electrons and holes. [179]

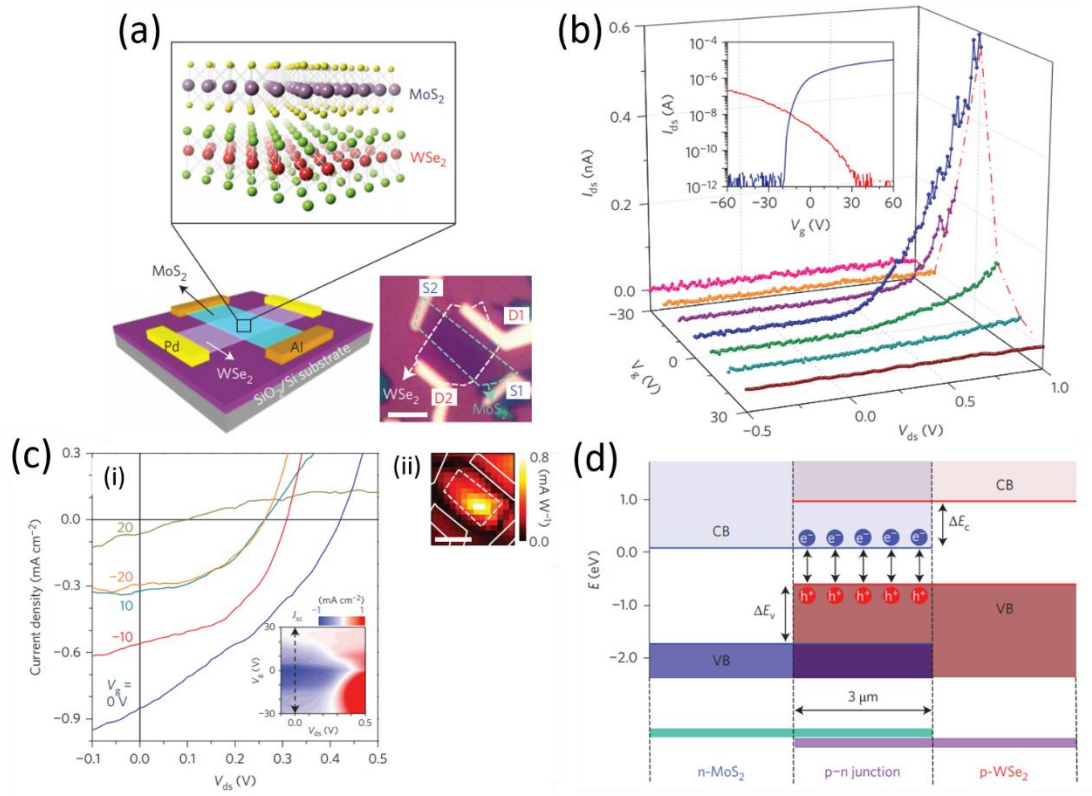

Figure 2.23. Photovoltaic effect in photodiodes. (a) Schematics and optical image of a typical photodiode based on vertical MoS_2/WSe_2 heterojunction. (b) Gate dependent I-V characteristics of the photodiode. (c) Gate dependent photoresponse characteristics of the photodiode. (i) and the photocurrent mapping of the MoS_2/WS_2 photodiode. (d) Energy band diagram of MoS2, WS2 and their overlapping area. ref. [179]. Reprinted with permission from **© 2014 Macmillan Publishers Limited. All rights reserved**

2.5.3 Schottky Barrier- Contact Engineering

As the channel length reduces in transistor, the performance of devices become dominated by the contact resistance at the interface between semiconductor and metal electrodes.[181-183] To achieve high photoresponsivity and high on-state current, low contact resistance is desirable in devices made by 2D materials. For metal-

semiconductor junctions, Schottky barrier height (SBH) is a crucial figure of merits to resolve the contact resistance. Generally, as the Schottky barrier height increases, the energy required for thermionic emission transport of charge carriers to overcome the barrier at the interface also increases.

Ideally, the SBH between metal and semiconductor can be estimated by the Schottky-Mott rule, which describes the SBH as the energy difference between the vacuum work function of metal and the vacuum electron affinity of semiconductor. [184-185] According to the rule, it is possible to modulate the Schottky barrier height by choosing different metals with various working function for a semiconductor channel. However, in real metal-2D semiconductor contacts, the experimental results do not match with the Schottky-Mott rule. The work functions of metal have negligible influence on the Schottky barrier heights, due to Fermi level pinning effect.[186-187] For example, when using Sc and Pt as the metal contacts for the MoS_2 based transistors, the theoretical Schottky barrier height should be -0.7 eV and 1.4 eV, respectively, according to Schottky Mott rule. However, the experimental measurement indicated that the SBH is 30 meV for Sc and 230 meV for Pt.[188] A plot of extracted Schottky barrier heights for a selection of metals is illustrated in **Figure 2.24(b)**.

Naturally, the Fermi level pinning phenomenon occurs as the result of the charged states in the semiconductor side at the interface, with energy states inside the semiconductor's bandgap. These charged states could possibly be introduced by the chemical bonding between metal and semiconductor during metal deposition or already exist in the semiconductor–vacuum surface. The highly dense surface states can absorb a large

amount of charge injected from metal, acting as a shielding. Consequently, the semiconductor's bands would likely align to a location relative to the surface states which is macroscopically exhibited as a pinning to Fermi level.

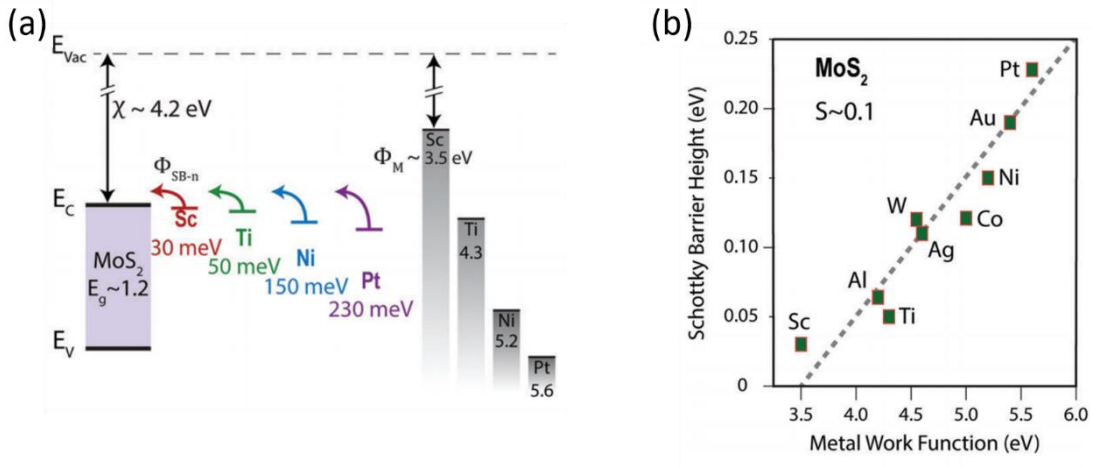

Figure 2.24. Fermi level pinning at the contacts between metal and 2D semiconductors. (a) Schematic band diagram of the calculated and experimental band alignment between MoS_2 and various metal contacts (b) Experimental Schottky barrier height as function of metal work function. ref. [178]. Reprinted with permission from **© 2018 The Royal Society of Chemistry.**

Being a highly conductive 2D material, graphene is a promising replacement for metal contact in 2D devices. Comparing to metal-2D semiconductor interfaces, the graphene-2D semiconductor interfaces are supposed to be better for two reasons. First, thanks to the unique linear dispersion relationship with finite density of states in graphene, by applying gate voltage or doping, it is possible to modulate the Fermi level of graphene for a better band matching.[190-191] Second, unlike metal, graphene is more chemically inert which limits the formation of chemical bonds with other 2D semiconductors. With

proper transfer technique to assembly the 2D heterojunctions, the amount of charge trapping states at the interface of graphene and 2D semiconductors could be significantly reduced, resulting in a weakened Fermi level pinning effect.[192-193]

2.6 2D heterostructures

The successful isolation of ultrathin 2D materials created a new area in materials science: 2D heterostructures. In 2D heterostructures, 2D materials are either vertically or lateral stacked. Among the family of 2D materials, graphene is an ideal candidate for electrodes and h-BN is a promising dielectric material. By combining with other semiconducting 2D materials, the 2D heterostructure can be the fundamental building blocks for a wide range of ultrathin electronic and optoelectronic devices, such as transistors, phototransistors, solar cells, LEDs, and photodetectors. This section will present a brief review of lateral and vertical 2D heterostructures.

2.6.1 Vertical Heterostructures

The vertical heterostructures, also known as van der Waals heterostructures, are usually assembled via layer-by-layer transfer. The dry transfer methods, such as the PDMS stamping technique, is popular among research groups, allowing one 2D material to be transferred onto another. Different type of 2D stacks have been fabricated and studied including graphene/hBN,[194-195] graphene/MoS_2,[190,196-197] graphene/WS_2,[198-199] WSe_2/MoS_2,[200] and WS_2/MoS_2.[201-202] By manually transfer, complex heterostructures can be stacked but the method suffers from poor scalability and contaminations at the interface between layers.

To conquer these problems, researchers have explored the possibility to synthesize the

vertical heterostructures using direct CVD growth method. The simplest vertical heterojunction is graphene/h-BN on metal substrate. Gao et al.[203] reported a temperature-triggered selective assembly of vertical Gr/hBN heterostructures. The process started with the CVD growth of a continuous monolayer hBN film on Cu, followed by the direct growth of graphene on hBN using benzoic acid as precursor. The reaction temperature was restricted to <900 °C, in order to protect the underlying hBN film. Song et al.[204] reported a CVD process using prepatterned PMMA as seedings on Cu substrate, as displayed in **Figure 2.25(a)** and **(b)**. The advantage of this method is that the location and nucleation density of graphene domains can be precisely controlled.

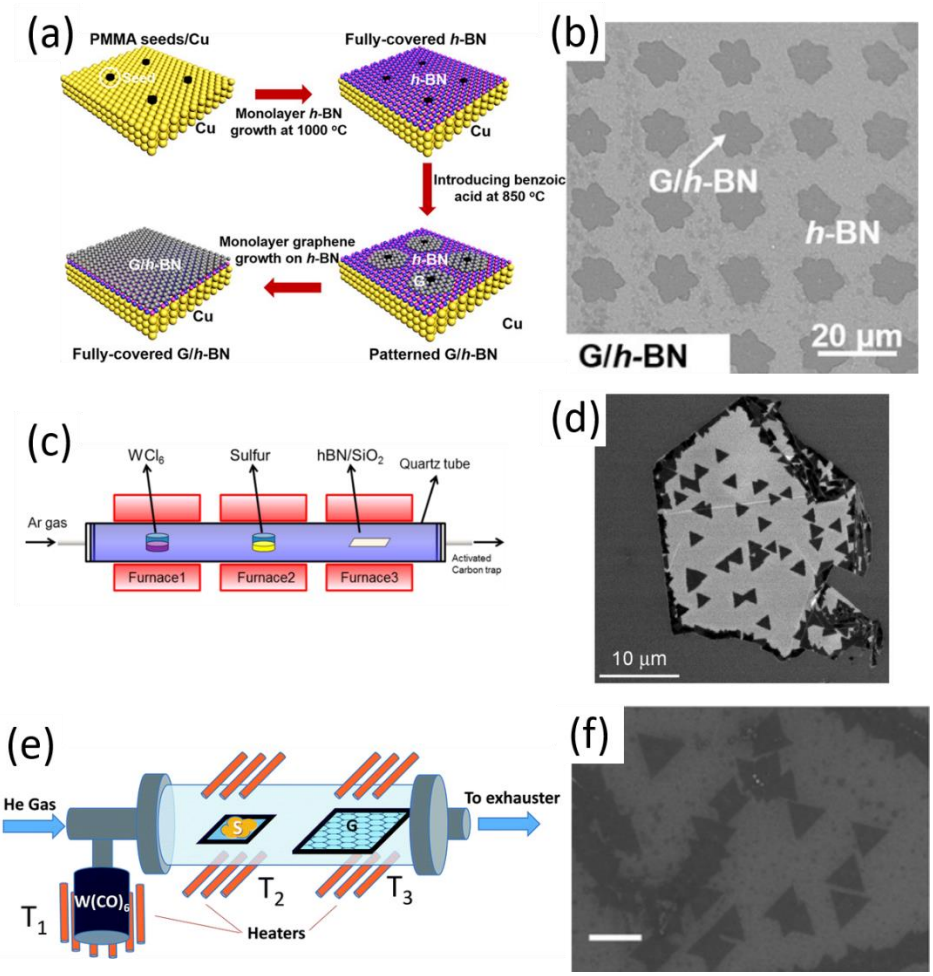

Figure 2.25. Direct CVD growth of vertical heterostructure. (a) Schematic illustration of direct CVD growth of Gr/hBN heterostructure with PMMA seeding. (b) SEM image of as grown graphene/hBN heterojunction arrays. ref. [204]. Reprinted with permission from © **2016 American Chemical Society.** (c) Schematic illustration of the three hot zone system to grow WS_2/hBN heterostructure using WCl_6 and S as reagents. (d) SEM image of oriented WS_2 domains grown on the surface of hBN flakes. ref. [205] Reprinted with permission from © **2014 American Chemical Society.** (e) Schematic illustration of MOCVD setup used to grow WS_2 on graphene surface. (f) SEM image of triangular WS_2 domains grown on graphene. The scale bar is 500 nm. ref. [209]. Reprinted with permission from © **The Royal Society of Chemistry 2015**

hBN is also considered as the ideal substrate for the CVD growth of other 2D semiconductors, as hBN is chemically inert, dangling bonds-free and charged impurities-free. Okada et al.[205] used a three-furnace CVD system for the direct growth of monolayer WS_2 domains onto mechanical exfoliated hBN flakes. The crystalline orientation of as grown WS_2 domains was characterized by low-energy electron microscopy (LEEM), showing a strong oriented growth behavior due to the van der Waals force and the Coulomb interaction between WS_2 and hBN layers. Later, Zhang et al.[206] reported similar method to grow WSe_2 domains on hBN. Wang et al.[207] reported direct CVD growth of monolayer MoS_2 on hBN films transferred on SiO_2/Si substrate. It was discovered that the MoS_2 had higher nucleation density but smaller average domain size on hBN surface comparing SiO_2/Si. This can be explained by the increased surface roughness of hBN film due to transfer process.

Similar to hBN, chemically inert graphene can also be used as growth template for other 2D materials. Shi et al.[208] demonstrated direct CVD growth of MoS_2 domains on graphene/Cu substrate using ammonium thiomolybdate as precursor. The growth temperature was restricted to 400 °C to prevent the sulfurization of Cu substrate. MoS_2 domains were orientedly grown on the graphene surface and by increasing the amount of precursor transported to surface of graphene, continuous film of MoS_2 could form on the surface of graphene. Bianco et al.[209] reported CVD growth of WS_2 on orientedly graphene on SiC and CVD grown graphene transferred on SiO_2 using a MOCVD process using $W(CO)_6$ as precursor. The domain size could reach up to 200 nm.

Besides this, numerous efforts have been applied to direct CVD synthesis of 2D semiconductor vertical heterostructure to avoid trapped impurities and transfer residues at the interface. Gong et al.[210] developed a single step controlled CVD process to synthesize MoS_2/WS_2 heterostructure using a powder mixture of MoO_3, tellurium and tungsten, and sulfur powders. By putting them in the different positions in the furnace, the nucleation and growth rate of MoS_2 and WS_2 could be controlled individually, which determines the sequence of deposition and the final structure. Vertical WS_2/MoS_2 bilayer heterojunctions could be constructed at 850 °C. Zhou et al.[211] demonstrated a two-step-oriented growth of $SnSe_2/MoS_2$ vertical heterojunction. The photodetector based on this heterojunction exhibited a photoresponsivity up to 9100 A/W, two orders of magnitude higher than conventional devices made by MoS_2 only.

2.6.2 Lateral Heterostructure

As is challenging to atomically stitch different 2D materials using transfer method, lateral heterostructures are mostly stacked via multistep vapor phase deposition. The typical procedure consists of two steps. One of the 2D materials is first controlled synthesized or patterned, followed by a second step growth of another 2D material on the edge of it. Similar to vertical heterostructures, the graphene/hBN lateral heterostructure is the simplest structure to construct. Han et al.[212] reported a two-step continued CVD growth procedure to assembly lateral hBN/Graphene film on Cu. During this process, hBN could directly nucleate and grow at the edge of hexagonal graphene domains. (**Figure 2.26(a)**) Shortly afterwards, Liu et al.[213] reported lateral oriented growth of graphene/hBN lateral heterojunction with a hydrogen etching step

to create hexagonal holes in monolayer graphene film on Cu. The purpose of hydrogen etching was to create sharp and clean graphene edge that enables the nucleation of hBN.

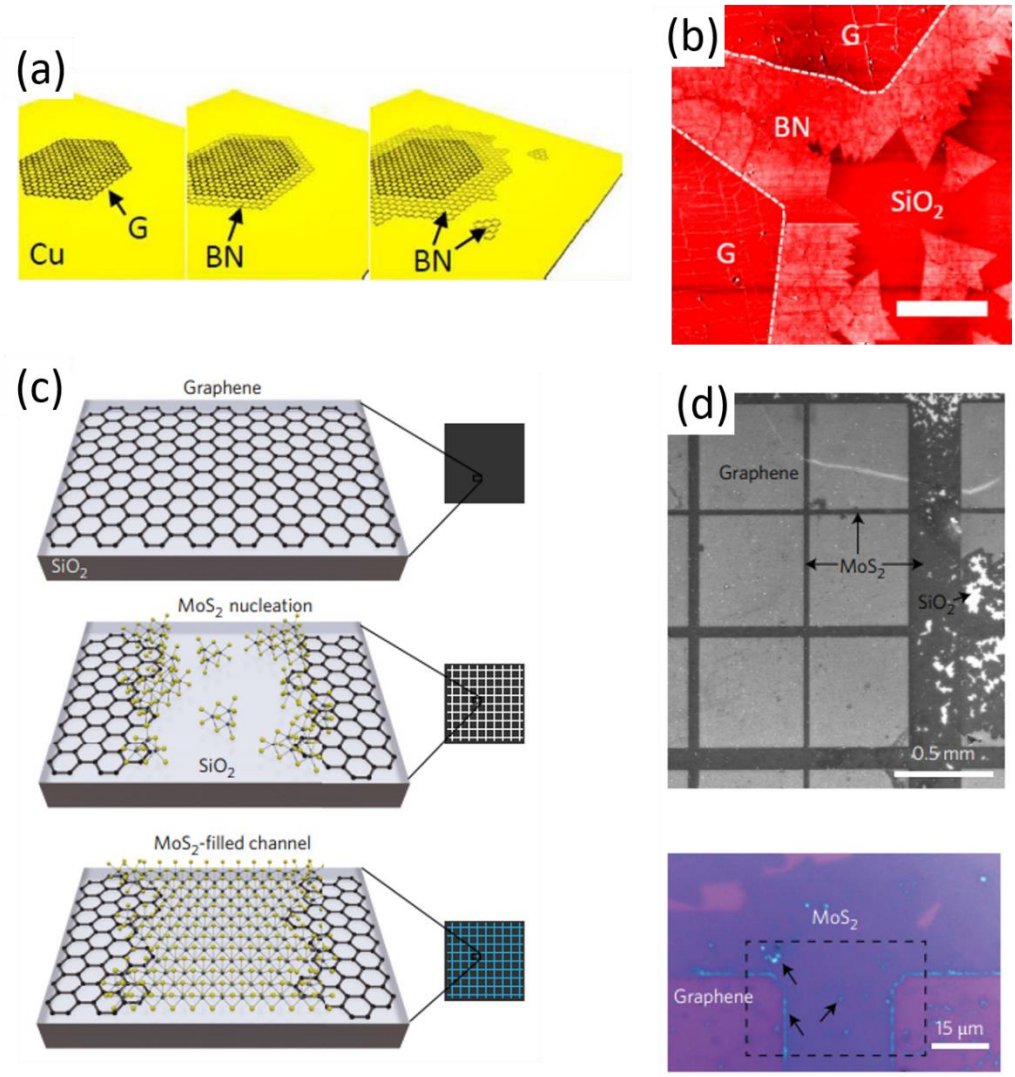

Figure 2.26. Direct CVD growth of lateral heterostructure. (a) Schematic of the CVD growth of lateral graphene/hBN heterostructure. (b) AFM phase mode image of graphene/hBN lateral heterojunction, suggesting that the nucleation of hBN happens at the edge of graphene. ref. [212]. Reprinted with permission from **© 2013 American Chemical Society.** (c) Schematic illustration of the CVD growth of MoS2 in the prepatterned graphene channel. (d) SEM image (top) and optical image (bottom) of CVD grown MoS_2/graphene lateral heterostructure. ref. [214] Reprinted with permission from **© 2016 Macmillan Publishers Limited, part of Springer Nature. All rights reserved.**

Recently, lateral heterostructures between graphene and 2D semiconductors is a structure of great interests as they can be important building blocks for 2D electronics and optoelectronics. The most straightforward fabrication route is to transfer the graphene onto the desired substrate, pattern the graphene and directly CVD grow 2D semiconductors. Zhao et al.[214] demonstrated the CVD growth of large-scale, spatially controlled lateral MoS_2/Graphene heterojunctions. Transmission electron microscopy (TEM) images proved that the heterogeneous nucleation of monolayer MoS_2 occurs at the edge of graphene. The phototransistor based on the MoS_2/graphene heterostructure was reported to have an on-off ratio of ~10^6 and mobility of 17 $cm^2V^{-1}s^{-1}$. In 2017, Zheng et al.[215] demonstrated large-scale seedless CVD synthesis of WS_2/graphene lateral heterostructure. A flat-band condition (zero Schottky barrier height) was observed, suggesting a negligible contact resistance and perfect band alignment between graphene and WS_2. Almost at the same time, Tang et al.[216] reported direct CVD assembly of WSe_2/graphene lateral heterojunction using similar procedure. The cross-section TEM image of the interface of WSe_2 and graphene proved that there was an overlapping region at the interface.

Heterostructures between 2D semiconductors is another structure being widely studied recently. In most cases, the heterostructures are fabricated by growing individual component sequentially with multistep CVD growth, providing atomically sharp interface and narrow active region at the junction. So far, several lateral heterostructures including MoS_2/WS_2,[210,217-218] $MoSe_2$/WSe_2,[219-220] WS_2/WSe_2,[221] MoS_2/$MoSe_2$,[221] and

WSe_2/MoS_2,[222-223] have been successfully fabricated. However, the biggest challenge is that most single layer or few layer 2D materials have no tolerance to high temperature which may cause thermally degradation during multistep CVD process.

2.7 Conclusion

After decades' study on graphene and other 2D materials, heterostructures based on 2D materials has become a new chapter in the history of science. The long-term studies on the properties and synthesis of individual 2D materials have paved way for the fabrication of 2D heterostructures. Thanks to the versatile electronic properties of 2D warehouse, including insulators, semiconductors, semi-metals and metals, it provides the opportunity to assembly 2D heterostructure with various functionalities in electronic and optoelectronic applications, which have great potential in ultrathin and flexible nanodevices.

Chapter 3

Methodology

3.1 Introduction

This chapter aims to give a brief introduction to the major apparatuses used for the synthesis of materials, device fabrication and property characterization, which are exclusively employed in this project. Comparing to the working principles, this chapter will focus more on the equipment models and operational details of the techniques used, including CVD setups and recipes, transfer methods for 2D materials, device fabrication and characterization of physical and electronic properties. By providing these details, I expect that all the experiments and measurements results in this thesis can be reproduced by other people in future.

3.2 Graphene synthesis, transfer and patterning

3.2.1 CVD growth of graphene

As is illustrated in **Figure 3.1**, a 4-inch CVD system was used to prepare the graphene sheets for further processing. The CVD system is composed of a horizontal furnace with accompanying control unit (Carbolite model HST 12/400) and a 4-inch quartz tube. A piece of 14 cm × 6 cm copper foil (Goodfellow, 99.8%, thickness ~ 25 μm) was first manually polished using Brasso for 15 min. Afterwards, copper foil was sonicated in diluted hydrochloric acid solution (HCl, Alfa Aesar, 37 % HCl:H_2O = 1:3) for 2 min to remove oxide residue on the surface, followed by sonication in acetone and isopropanol (IPA) for 5 min, respectively, to remove remaining chemical residues. Finally, the

copper foil was flattened on a ceramic plate and placed in the center of an air-tight 4-inch quartz tube. The horizontal furnace was then moved to the copper sheet's position by sliding it across mounted rails. During the reaction, the copper sheet was positioned at the center of the furnace in order to maintain a uniform temperature across the copper sheet. Three different types of gas were used in the system: 1% methane in argon (BOC), 25% hydrogen in argon (BOC), and 100% argon (BOC), referring to CH_4, H_2 and Ar. Three Alicat mass flow controllers connected to a computer were used to individually control the flow rate of each gas, using Flowvision software. The flow rate of all three gases was measured in standard cubic centimeters per minute (sccm).

The whole CVD process to grow continuous graphene film was performed at atmospheric pressure. The system was first purged with 2000 sccm Ar, 500 sccm H_2 and 50 sccm CH_4 for 30min. Afterwards, the gas flow was changed to a mixture of 500 sccm Ar and 100 sccm H_2. At the same time, the furnace was heated to 1060 °C at a ramping rate of 60 °C/min. After reaching the target temperature, the copper sheet was annealed with the same flow for 1 hour. The nucleation and growth of graphene was then initiated by changing the gas flow to 500 sccm Ar, 100 sccm H_2 and 10 sccm CH_4. The growth stage lasted for 1 hour. After growth, the graphene sample was fast cooled by sliding the furnace away from the sample to one end of the rail.

Figure 3.1. The CVD setup used for graphene synthesis in this thesis.

3.2.2 Transfer of graphene

In this project, the CVD-grown graphene films were required to transfer onto Si wafer with 300 nm oxide layer (SiO_2/Si) substrate for measurements and other post-processing. The as-grown graphene sheet was first spin coated with a layer of Poly-methyl-methacrylate (PMMA, 8% wt. in anisole, 495k molecular weight) with a spin coater (Laurell-WS-650MZ-23NPP). The spin-coating process took 60 seconds at 4500 rpm for desirable thickness of PMMA film. A hot plate (STUart-SD160) was used to cure the PMMA/graphene at 180 °C for 90 seconds to evaporate the anisole. Afterwards, copper substrate was removed by floating the sample on an ammonium persulfate solution (APS, 0.2 mol/L). The PMMA/graphene sheet was then rinsed by floating on

deionized water (DI water) for three times, 30 min each time, to remove remaining etchants. After the cleaning process, a SiO_2/Si chip was used to scoop the PMMA/graphene film. The sample was then left overnight to evaporate the water encapsulated between PMMA/graphene film and SiO_2/Si substrate. Afterwards, the sample was baked on the hot plate for 15 min at 150 °C to completely remove the water residue and make the PMMA/graphene firmly attached on the substrate. Subsequently, the sample was placed in warm acetone (~ 45 °C) for 2-3 hours to remove PMMA.

3.2.3 Graphene patterning

To pattern the as-transferred graphene into desired growth template for subsequent CVD growth of other 2D materials, electron beam lithography (EBL, JEOL 5500 FS) was utilized. Depending on the design of pattern, either positive or negative resists were used.

In order to pattern graphene ribbons, negative resist (maN-2403) was used. maN-2403 resist was first spin coated on as transferred graphene on SiO_2/Si chip at 3000 rpm for 30 seconds. The sample was then baked at 90 °C and cooled to room temperature before exposure to electron. After exposure, the negative resist was developed in ma-D525 for 120 seconds and the remaining developer was washed away by DI water. The excess graphene area was etched away by oxygen plasma generated from the RF electromagnetic field in a reactive ion etching (RIE, Plasmalab 80 Plus) equipment. Finally, the negative resist was removed by REM-660, followed by acetone to remove the residue chemicals.

In order to pattern the gaps in the middle of graphene ribbons, bilayer PMMA positive

resist was utilized. A PMMA-495k (8% wt. in anisole, 495k molecular weight) layer was first spin-coated on the sample, followed by spin coating of another layer PMMA-950k (8% wt. in anisole, 950k molecular weight). Both layers were spin-coated at 4500 rpm for 45 seconds and then baked for 90 seconds at 180 °C on the hot plate. After electron exposure, the bilayer PMMA film was developed by 1:3 MIBK/IPA developer, followed by the RIE treatment to remove the excess graphene. Finally, the sample was cleaned by acetone to remove the residue PMMA.

3.3 Chemical Vapor Deposition synthesis of 2D Materials on Graphene Templates

3.3.1 Synthesis of Molybdenum Disulfide (MoS_2) on Graphene Templates

As depicted in **Figure 3.2**, a two-furnace CVD system was used to synthesize MoS_2 on monolayer graphene transferred on to a Si wafer with SiO_2 surface layer, using Sulfur and MoO_3 powder as precursors. Sulfur powder and the substrate were placed in the middle of front (Furnace 1) and back furnace (Furnace 2) respectively for precise temperature control, while MoO_3 could be tuned by the distance from the center of Furnace 2. The Graphene/SiO_2 substrate was placed vertically to the direction of gas flow so that the reaction took place uniformly on the substrate. The whole reaction was carried out within two parallel furnaces in Argon atmosphere under ambient pressure. Similar to the CVD method previously reported, a multiple-step CVD process was developed with four stages. (1) Creation of a S rich environment in quartz tube by heating up Furnace 1 and Furnace 2 to 160 °C and 200 °C respectively for 15 min with

a 10 sccm H_2 gas and 140 sccm Ar gas flow.(2) Main nucleation stage of MoS_2 domains by heating up Furnace 1 to 200 °C and Furnace 2 to 770 °C which corresponded to the temperature of S and graphene substrate respectively. The temperature of MoO_3 precursor was about 400 °C when Furnace 2 was heated up to 770 °C. The nucleation stage lasted for 15 min. (3) Growth stage of MoS_2 domains by changing the gas flow to 10 sccm H_2. The growth stage lasted for 15-45 min, depending on the demands of MoS_2 topology. (4) Fast cooling to room temperature after the growth stage by moving the furnace 2 to the right end and exposing the sample.

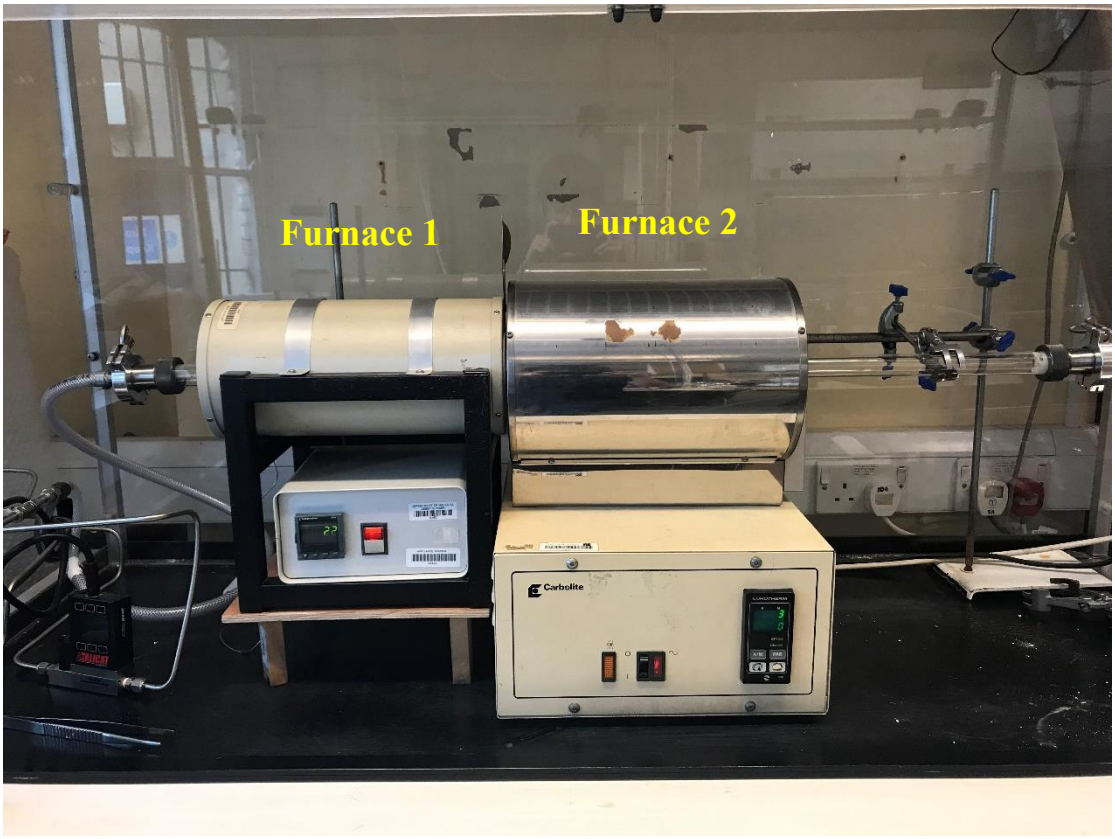

Figure 3.2. The CVD setup used for synthesis of MoS_2, WS_2 and GaS in this thesis.

The furnace on the left refers to the Furnace 1 and furnace on the right refers to the Furnace 2 in this chapter.

3.3.2 Synthesis of Tungsten Disulfide (WS_2) on Graphene Templates

A two-furnace system using the same setup in section 3.3.1 was used to synthesis WS_2. Sulfur and WO_3 powder were used as precursors. Sulfur powder and WO_3 powder were placed in the middle of Furnace 1 and Furnace 2 and the Si wafer substrate with pre-patterned graphene template was placed at downstream of WO_3 precursor. A multiple-step CVD process with four stages was designed to CVD grow the WS_2 (1) Heating up Furnace 1 and Furnace 2 to 180 °C and 1000 °C, respectively, from room temperature with a mixture gas of 240 sccm Ar and 10 sccm H_2 gas flow. The two temperature

correspond to actual temperature of S and WO_3 precursor during the reaction. (2) Main nucleation and growth stage of WS_2 starts when two furnaces reached target temperature; (3) when the growth stage ended, the reaction was stopped by cooling Furnace 2 down to 900 °C. Afterwards, furnace 1 was heated up to 400 °C and Ar flow rate was set to 490 sccm to blow away surplus S powder. (4) Cooling process by setting both furnaces to room temperature and Furnace 2 was moved to the right end to expose the sample for fast cooling.

3.3.3 Synthesis of Gallium Sulfide (GaS) on Graphene Templates

A one-furnace system was used to synthesize GaS in graphene gap, using the same setup illustrated in **Figure 3.2**. During the reaction, only Furnace 2 was used. The Ga_2S_3 precursor was placed at the center of the growth furnace. The SiO_2/Si substrate with pre-patterned graphene was placed at the downstream of the growth furnace. The CVD growth of GaS was composed of three stages. First, the whole system was flushed with 500 sccm argon gas for 30 min. Afterwards, the carrier gas was changed to 70 sccm 25% H_2/ 75% Ar mixture gas. At the same time, the Ga_2S_3 precursor was heated up to 800 °C at a ramping rate of 50 °C/ min. The reaction started as soon as the temperature reached 800 °C. By holding the Ga_2S_3 precursor in H_2-rich atmosphere at 800 °C for 25 min, a high-coverage deposition of layered GaS on substrate could be achieved. After the reaction, the carrier gas was changed to 150 sccm Ar for fast cooling process to room temperature.

3.4 Material Characterization

3.4.1 Optical Microscopy

Optical microscopy (OM) is a useful tool to give a quick and non-destructive evaluation of samples, especially for checking the coverage and surface contaminants. A custom-built optical microscope was used in this project with a yellow LED as the light source. Two Mitutoyo objective lens, 10× and 50× magnification, were employed for different purposes. The images were acquired by a Thorlabs high-resolution 1280 × 1024 CMOS color sensor connected to a computer. Optic images were post-processed by ImageJ software to adjust brightness/contrast to highlight the information of interest

3.4.2 Scanning Electron Microscopy

In this project, scanning electron microscopy (SEM) was frequently used to investigate nanoscale geometry and identify the thickness of graphene and other 2D materials. A Hitachi S-4300 field-emission gun was employed in this project using 3 kV accelerating voltage with a beam current of 10 μA. The low accelerating voltage could minimize the charge-up and irradiation damage to samples. To prepare the samples, carbon sticky tape was used to paste the sample onto a sample stub. During imaging, the astigmatism, brightness, contrast and focus need to be adjusted to obtain the best image quality.

3.4.3 Optical Transmission Measurement

The optical transmission measurement is an effective method to determine the layer number of 2D materials. The absorbance at specific wavelength is also a crucial parameter to calculate the efficiency of photodetectors. A JASCO V-570 spectrometer was used to characterize the light transmission. Light from the ultraviolet to near infrared regime can be produced by this spectrometer. The transmittance was obtained by measuring the variation of intensity of light collected after passing through the

sample. Before measurement, all samples were transferred on a transparent substrate, which was glass in this project. A baseline was first taken by measuring the transmittance of a bare substrate. The samples were then measured in the range of target wavelength.

3.4.4 Raman and Photoluminescence Spectroscopy

Raman and photoluminescence (PL) spectroscopy measurements were performed in this project to provide an insight of the thickness, doping level, lattice strain and interlayer interaction of graphene and other 2D materials. Both Raman and PL spectra were collected using a JY Horiba LabRAM Aramis confocal Raman spectrometer. By switching modes in the software package installed, either Raman or PL measurement mode could be selected. The excitation light source was a linearly polarized 532 nm frequency Nd:YAG laser. The maximum power of the laser was 12.5 mW with a laser spot size around 1 μm. The laser intensity can be tuned by a set of filters to obtain a proper laser power in case of signal saturation or laser damage to sample. Before measurements, a standard silicon chip was used to calibrate the system.

Two different types of grating, 1800 g/mm (1800 silts per mm grating) and 600 g/mm can be selected for different purposes. 1800 g/mm grating was used for Raman measurement due to better spectral resolution while the PL measurements were performed using 600 mm^{-1} grating for fast capture. In both modes, the range of spectrum, either in cm^{-1} or nm, as well as the acquisition time and accumulating number could be set using the software installed to obtain a good signal intensity and signal to noise ratio. To investigate the uniformity of as grown 2D materials, Raman and PL mapping

measurements were utilized. They were pre-programmed capture of multi-point spectra across lateral dimensions (XY coordinates) in a fixed step size by sequence. The spectra of each point could be reconstructed into XYZ grid mapping image in Origin software.

3.4.5 Atomic Force Microscopy

Atomic force microscopy (AFM) is the most straightforward technique to characterize the thickness, layer number and surface morphology of 2D materials. Characterization of the as-grown GaS within prepatterned graphene ribbons' gap in Chapter 6 was performed by Ms. Yu Shu, with an atomic force microscope (Asylum Research MFP-3D) using an AC-160TS cantilever made of silicon (Olympus, resonant frequency ~ 300 kHZ and spring constant ~42N/m). The thickness of GaS film grown on SiO_2 can be directly measured without transfer. There are four imaging modes in the AFM, which can be recorded simultaneously: topography, phase, amplitude and Kelvin probe microscopy (KPM) modes. In this project, topography mode was used to display the height profile and determine the thickness of GaS film. The AFM data were processed by software, Gwyddion.

3.5 Device Fabrication and Measurement

3.5.1 Device Fabrication

The device fabrication process started with the metal bond pad patterning by EBL patterning utilizing the bilayer PMMA positive resist demonstrated in section 3.2.3. After the EBL patterning and development, the samples were sent into a thermal evaporator (Edward 360) to deposit of Cr/Au (10 nm/ 80 nm) metal bond pads. During the thermal evaporation process, Cr and Au were evaporated by Joule heating in a

vacuum environment and deposited onto the target substrates at a controlled rate. After deposition, excess region of metal films was removed by a lift-off process, where the metal films on the resist was delaminated by placing the samples in warm acetone (45°C) overnight to dissolve the PMMA

3.5.2 Electrical and Opto-Electrical Measurement

A home-built probe station., shown in **Figure 3.3**, was employed for the electrical and opto-electrical measurements of the devices fabricated in this project. The as fabricated devices were placed on a moveable stage which can be adjusted in X, Y and Z directions using digital controllers. A 532 nm diode-pumped solid-state laser (Thorlabs, DJ532-40) was used as monochromatic excitation source for the photodetection measurements of MoS_2 and WS_2 photodetectors. The laser, coupled into a confocal microscope, can be focused into a ~150 μm^2 spot size. For illumination during the photodetection measurements for GaS phototransistor, Thorlab LED370E was used as the light source for blue light (centered 375 nm) and Thorlab M275L4 as UV light source (centered 275 nm). The power values of the laser and LEDs were measured with a manually fixated power meter (Thorslab Optics PM100D) which was placed under the illumination light source before each measurement. All the I-V and I-V_g measurements were performed with two Keithley 2400 source meters. One Keithley source meter was connected to the bond pads of devices via two tungsten tips (Signatone SE-T) to apply a source-drain bias. The gate voltage was applied by connecting the p-doped silicon substrate from the back side with another Keithley source meter using silver paste. All measurements were carried out in a dark room at room-temperature under ambient pressure.

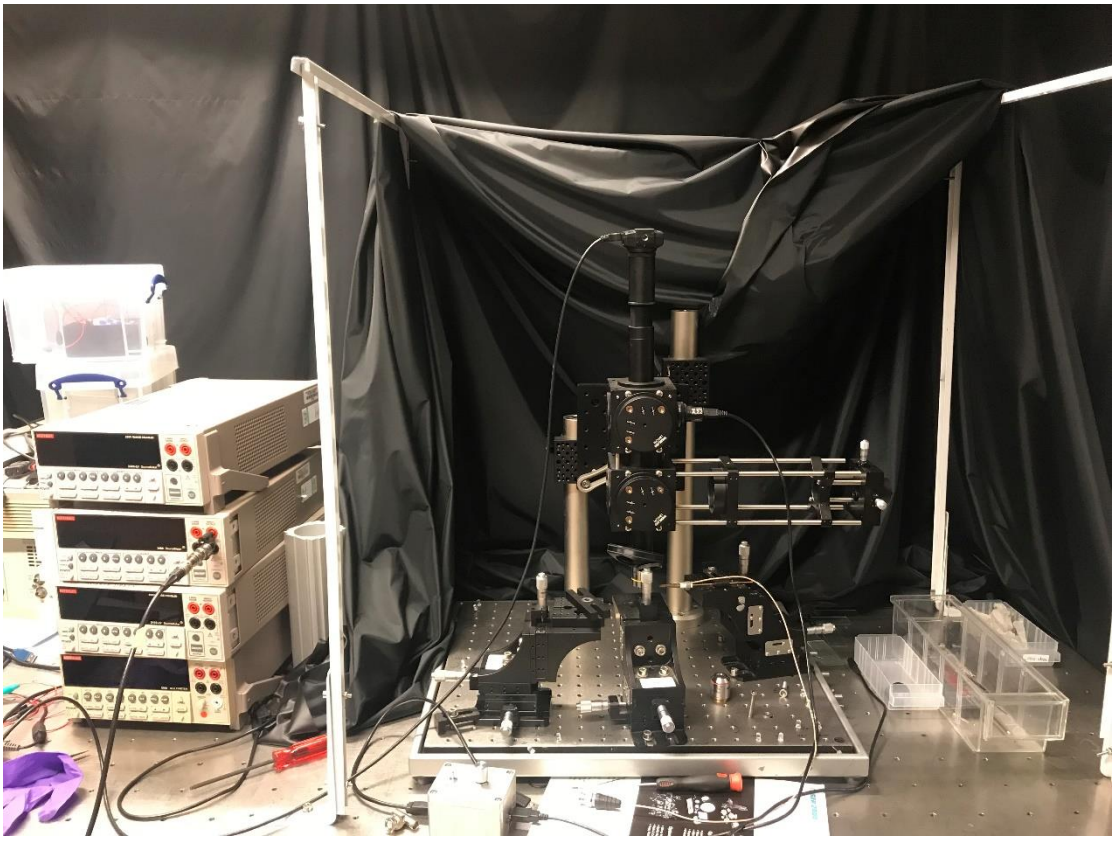

Figure 3.3 Custom-built probe station used for device characterization in this thesis.

Chapter 4

Hydrogen Assisted Growth of Large Area Continuous Films of MoS_2 on Monolayer Graphene

4.1 Introduction:

Two-dimensional (2D) materials have received considerable attention since successful isolation of graphene was first reported.[1] Monolayered 2D materials such as hexagonal Boron Nitride (h-BN) [224] and transition metal dichalcogenides (TMDs) including tungsten disulphide (WS_2), [131] molybdenum disulphide (MoS_2), [225] tungsten diselenide (WSe_2), [226] molybdenum diselenide ($MoSe_2$), [227] etc. [228] have been successfully synthesized. Among them, MoS_2 has become increasingly investigated due to its semiconductor properties with a direct band gap (1.8 eV), and it has shown a potential in manufacturing the next-generation nano-electronics, optoelectronics and flexible devices. [81, 88, 90, 229] To make such devices, different 2D materials are usually vertically stacked together, giving rise to van der Waals heterostructures that could take the advantage of transparency and flexibility properties of 2D materials [199, 201, 230-232].

The successful fabrication of different MoS_2-graphene based heterostructure devices usually involves two steps: individual synthesis of 2D MoS_2 by CVD growth, exfoliation or PVD method followed by layer-by-layer transfer with aids of solvent or polymer. [233-237] However, scalable fabrication of high-performance devices is difficult to achieve by those approaches. The transfer process is not only time-consuming but inevitably introduces imperfections such as cracks, wrinkles and polymer residuals,

which can dramatically affect the doping level of TMDs and hence the band gap and light transfer efficiency. [238]

An ideal solution is to directly synthesize MoS_2 on other 2D materials by CVD methods. A few studies have been reported about the realization of direct CVD growth of MoS_2 domains. [208, 239] However, the MoS_2 coverage reported in these studies was relatively low and the size of MoS_2 domains synthesized could only reach sub-micron scale, which limits their application in device fabrication. Chen et al. reported successful CVD growth of large-scale bilayer MoS_2 film on graphene substrate but the photoresponsivity is only 32 mA/W. [240] Besides, most of these synthesis procedures were also carried out at low pressure, which increases the complexity of experimental equipment and processing design. Further work is needed to realize the direct growth of large area film coverage of monolayer TMD materials on other 2D materials such as graphene and h-BN.

In this chapter, I demonstrate how direct growth of large area (1cm x 1cm), continuous monolayer MoS_2 films on graphene can be realized by the controlled addition of hydrogen to modify the nucleation of domains. I explore the sensitivity of monolayer graphene to decomposition during the reactions and optimize the conditions to enable growth of continuous MoS_2 films within a time scale that allows graphene to survive at the high temperature needed for MoS_2 crystallization. The large area MoS_2:graphene vertical stacked layered system is utilized to create arrays of photodetectors with lateral electrodes, yielding high photocurrents and photoresponsivity.

4.2 Results and discussion

As depicted in **Figure 4.1(a)**, a two-furnace CVD system was used to synthesize MoS_2 on monolayer graphene transferred on to a Si wafer with SiO_2 surface layer. Graphene was grown by CVD on Cu substrate. Sulfur powder and the substrate were placed in the middle of front and back furnace respectively for precise temperature control, while the temperature of MoO_3 could be tuned by the distance from the center of Furnace 2. The Graphene/SiO_2 substrate was placed vertically to the direction of gas flow so that the reaction took place uniformly on the substrate. The whole reaction was carried out within two parallel furnaces in Argon atmosphere under ambient pressure. Similar to the CVD method previously reported, I designed a multiple-step CVD process with four stages. [241] (1) Creation of a S rich environment in quartz tube by heating up Furnace 1 and Furnace 2 to 160 °C and 200 °C respectively for 15min with a 150 sccm Ar gas flow. (**Figure 4.1(b)** and **(c)**, section I) (2) Main nucleation stage of MoS_2 domains by heating up Furnace 1 to 200 °C and Furnace 2 to 770 °C which corresponded to the temperature of S and graphene substrate respectively. MoO_3 precursor was placed 10 cm away from the center of Furnace 2 which reached 400 °C when Furnace 2 was heated up to 770 °C. The gas flow was set to relatively high flux to increase local reactant concentration which favored the nucleation of MoS_2 domains. (**Figure 4.1(b)** and **(c)**, section II) (3) Slow growth stage by reducing the Ar flow rate to 10 sccm to maintain a slow and stable growth condition which favored the growth of MoS_2 domains. (**Figure 4.1(b)** and **(c)**, section III). (4) When the grow stage ended, the reaction was stopped by cooling down to 700 °C while keeping Ar flow rate to 10 sccm.

Then both furnaces were set to room temperature and Ar flow rate was set to 500 sccm for fast cooling.

The reason for this multi-step CVD setup is to achieve separate control of the nucleation density and then the growth of nuclei into larger domains. In the nucleation stage, the density of MoS_2 domains on graphene has a positive correlation with Ar flow rate while extending the growth time can increase the average MoS_2 domain size. By altering the flow rate during nucleation and growth time, I optimized the parameters to grow continuous MoS_2 films on graphene. Oriented MoS_2 triangular domains could be synthesized on the graphene surface using 50 sccm flow rate during the nucleation period with 15 min nucleation + 15 min growth CVD process, shown as **Figure 4.1(d)** and **(f)**. However, I noticed that the formation of a MoS_2 film could not be easily achieved by altering the parameters within this approach due to decomposition of the graphene. The introduction of hydrogen to the growth enabled faster growth and the formation of large area continuous MoS_2 films could be achieved on graphene, **Figure 4.1(e)** and **(g)**. The region with graphene underneath is about 1 cm×1 cm, as is pointed out in **Figure 4.1(e)**. **Figure 4.1(g)** is the SEM image of as synthesized MoS_2/Graphene heterostructure. The CVD grown MoS_2 film (black region) shows high continuity that almost completely covers the surface of graphene. The coverage of monolayer MoS_2 could reach up to 96%.

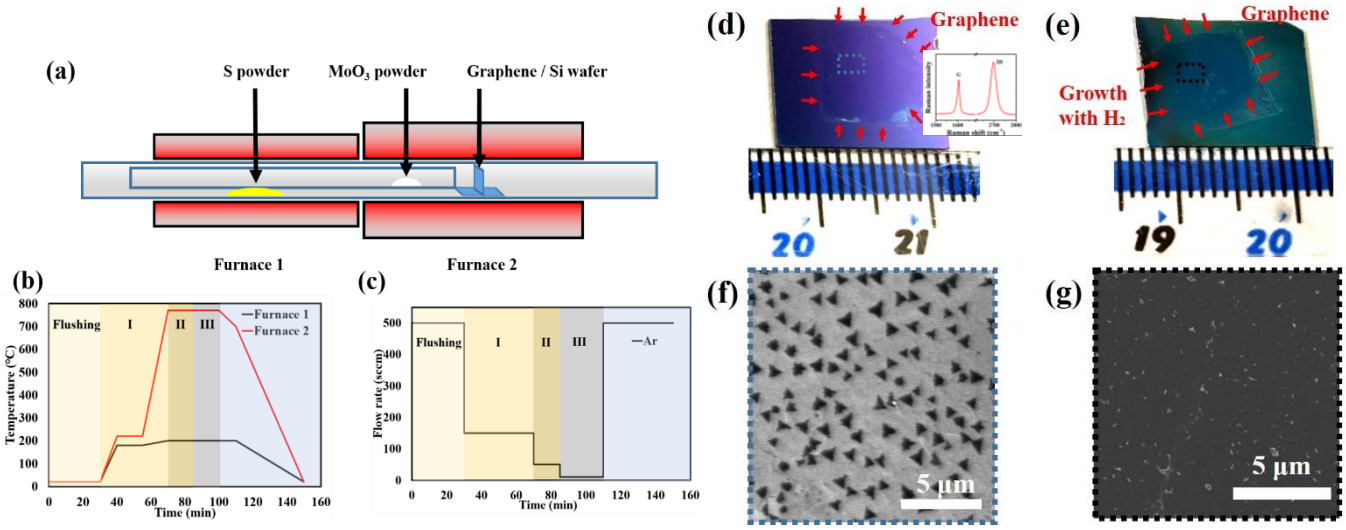

Figure 4.1. Atmospheric CVD synthesis of MoS_2 on graphene substrate (a) Schematic illustration of the two furnace CVD system used to synthesize MoS_2 on graphene substrate. (b) Temperature programming process of Furnace 1 and Furnace 2. (c) Gas flow programming process during the CVD process. (d-e) Photos showing contrast difference between graphene film transferred on SiO_2/Si substrate with and without H_2 respectively. The embedded figure shows the Raman spectrum of as transferred Graphene. (f) SEM image of triangular MoS_2 domains deposited on Graphene. (g) SEM image of MoS_2 film deposited on Graphene with aid of hydrogen.

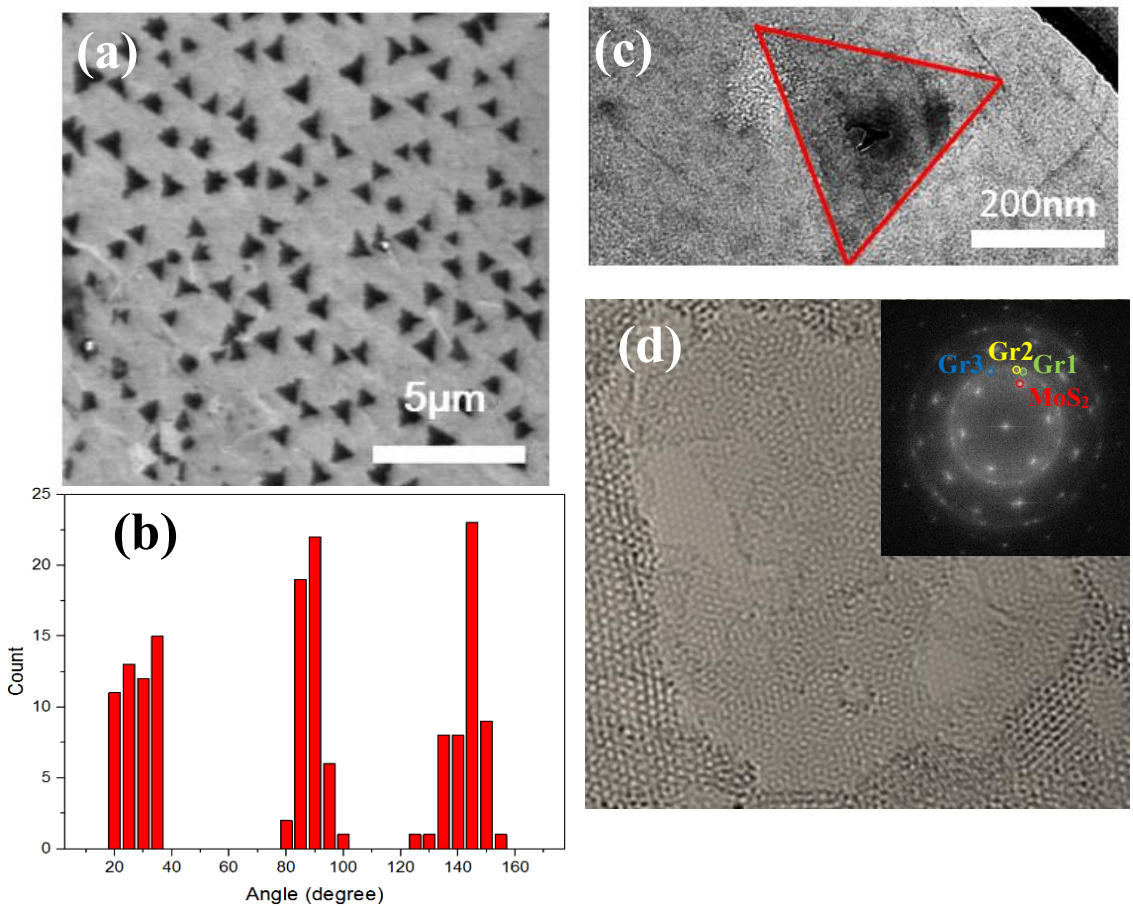

Figure 4.2. Characterization of monolayer MoS_2 domains on graphene substrate

(a) SEM images of triangular MoS_2 domains (black triangles) on graphene substrate. (b) is the statistic distribution of the angle between triangle edges and X axis. The three distinct peaks with 60° difference between each other showed good oriented growth of triangular domains. (c) and (d) are TEM picture and FFT pattern of Mo/G heterostructure, demonstrating that the MoS_2 synthesized on graphene was monolayer.

Figure 4.2(a) illustrates SEM image of synthesized MoS_2 domains grown on graphene. The size of triangular MoS_2 domains (black triangular in **Figure 4.2(a)**) could reach up to 1.5 μm. By quantifying the statistic distribution of edges of triangular domains, three distinct peaks can be obtained, with 60° angle difference between each peak, suggesting that there is an oriented relationship between triangular MoS_2 domains. The oriented growth behavior might be due to the match of orientations of graphene and MoS_2 hexagonal lattices. In the FFT pattern shown in **Figure 4.2(d)**, there was only one set of hexagonal diffraction pattern of MoS_2 which suggests that MoS_2 domains synthesized on graphene were highly crystalline and monolayer, which can be a good reference sample for the measurements mentioned below.

The reason MoS_2 film could not be formed by simply changing the growth time and flow rate was that the formation of large area continuous film required longer growth time while the graphene was observed not to sustain long time reaction within the CVD setup. In **Figure 4.3(a)** and **(b)**, I present the comparative CVD process with different growth time. I discovered that after an overall 40 min CVD process graphene started to disappear before MoS_2 films formed. The Raman spectrum of remaining graphene shows significant increase of D peak and decrease in 2D peak intensity (**Figure 4.3(e)**), suggesting that the graphene was heavily oxidized. [242]

I speculated that the oxidation of graphene resulted from reactive O released during the decomposition of the MoO_3 precursor as well as the decomposition of SiO_2 substrate at high temperature. Therefore, I introduced hydrogen into the carrying gas once the growth temperature reaches 770 °C. Hydrogen serves multiple purposes. Firstly,

hydrogen leads to more efficient reduction of MoO_3, aiding the formation of MoS_2 by reducing the precursors. Secondly, it acts as a reducing agent that reacts with reactive O atoms to prevent graphene from oxidation. Furthermore, at high temperature, hydrogen could help to further clean PMMA residuals away from graphene surface. After introducing H_2 into the CVD system, I observed that graphene could be well preserved during long time CVD process. (**Figure 4.3(c)**) Comparing to Raman spectrum of graphene without H_2 protection (**Figure 4.3(e)**), the rise in D peak decreased, indicating that graphene was less damaged in presence of H_2.[243] Moreover, I also observed that the concentration of hydrogen was crucial to the formation of MoS_2 domains. By applying different hydrogen concentration, I found that graphene could be well-protected and act as a growth template for MoS_2 with presence of a trace amount of hydrogen gas, while with a relatively higher hydrogen concentration no MoS_2 domains formed on the graphene's surface. (**Figure 4.3(c-d)**) This is due to the fact that besides being a reducing agent hydrogen also has an etching effect on MoS_2, especially at high temperature with high concentration.[153] The optimal carrying gas flow I discovered was a mixture of 7.5 sccm Ar and 2.5 sccm 25% H_2/75% Ar.

With a trace amount of hydrogen introduced into the CVD system, the CVD growth time could be extended longer than 40min. However, I noticed that MoS_2 film was not able to grow directly onto graphene substrate by simply increasing growth time with previous CVD process due to oxidization (**Figure 4.3(a)**). Even with an extended reaction time growth (15min nucleation+ 45min growth time), the size of MoS_2 domains remained barely unchanged and no continuous MoS_2 film was formed, which

suggests that there is a limitation in the size of MoS_2 domains on graphene surface, as shown in **Figure 4.4(a-c)**.

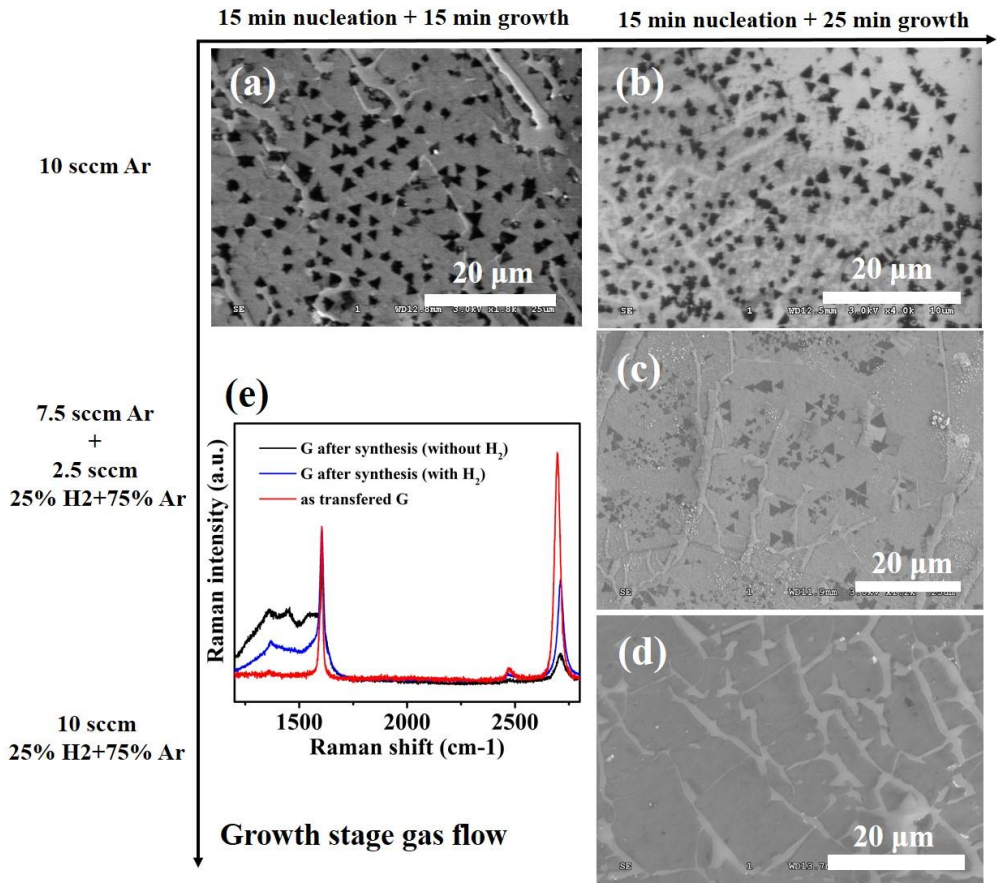

Figure 4.3. Influence of H_2 concentration in carrying gas on MoS_2 and graphene

(a) MoS_2 domains grown on graphene substrate with 15 min nucleation + 15 min growth in 10 sccm Ar flow; (b) MoS_2 domains grown on graphene substrate with 15 min nucleation + 25 min growth in 10 sccm Ar flow. Graphene (darker grey) started to be burned away; (c) MoS_2 domains grown on graphene substrate after 15 min nucleation + 25 min growth in 7.5 sccm Ar and 2.5 sccm 25% H_2/75% Ar gas flow. (d) MoS_2 domains grown on graphene substrate after 15 min nucleation + 25 min growth with higher H_2 concentration. (e) Raman spectrum of graphene before and after CVD synthesis. The black (without H_2) and blue (with H_2) plots corresponds to graphene in (b) and (c).

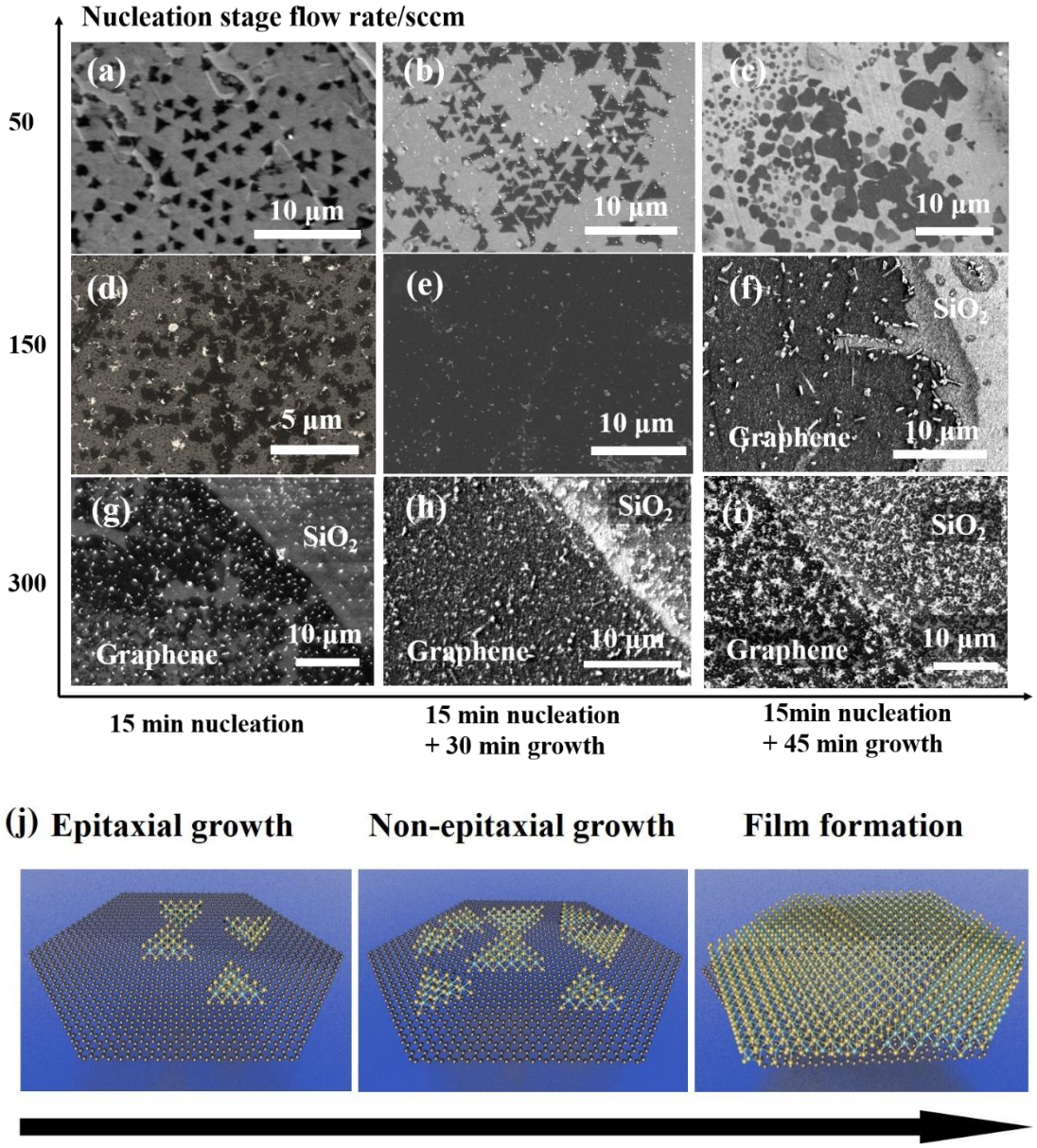

Figure 4.4. SEM images of comparable MoS_2 grown on graphene under different conditions. (a)-(i) are SEM image of MoS_2 grown on graphene using different nucleation flow rate and growth time. The white dots are 3D MoS_2 particles. Increasing the nucleation flow rate dramatically increased the nucleation density of 3D MoS_2 crystals. (j) the growth mechanism of MoS_2 film on graphene

With the size of individual MoS_2 domain restrained in certain range, the alternative way to grow a continuous lay of MoS_2 film is to increase the nucleation density of MoS_2 on graphene so that multiple small MoS_2 domains could be linked together. Different nucleation flow rate and growth time were applied to figure out the optimal conditions for the formation of continuous MoS_2 film. (**Figure 4.4**) I observed that with a high nucleation flow rate, 2D MoS_2 domains as well as 3D crystals nucleated, and these 3D crystals grew larger as the growth time increased. To maximize the nucleation density of MoS_2 on graphene but minimize the formation of 3D crystals, I tried different flow rate of nucleation stage and growth stage time. The optimal recipe for CVD growth of MoS_2 film on graphene was a 15min nucleation stage in 150 sccm Ar followed by a 30min growth stage in 7.5 sccm Ar + 2.5 sccm 25% Hydrogen/ 75% Ar. A continuous MoS_2 film could form on top of graphene substrate while at the same time the formation of 3D MoS_2 crystals was limited to a very low level. (**Figure 4.4(e)**) It should also be noticed in **Figure 4.4(d)** that upon increasing nucleation density, the MoS_2 domains grown on graphene starts to lose their orientation preference and show a non-oriented growth behaviour. These phenomena suggest that the evolution of continuous MoS_2 film consists of several steps. First, oriented MoS_2 domains formed on the surface of graphene substrate. As the size of these domains increase to their size limit (~5 μm), the rising lattice mismatch between graphene and MoS2 disfavour further growth of oriented MoS_2 domains. As a result, secondary MoS_2 domains nucleate on the edge of oriented MoS_2 domains and start non-oriented growth. The secondary domains grow until their edges merge and form the continuous film. Further MoS_2 deposited on the

MoS_2 film leads to the nucleation of 3D MoS_2 particles. (**Figure 4.4(j)**)

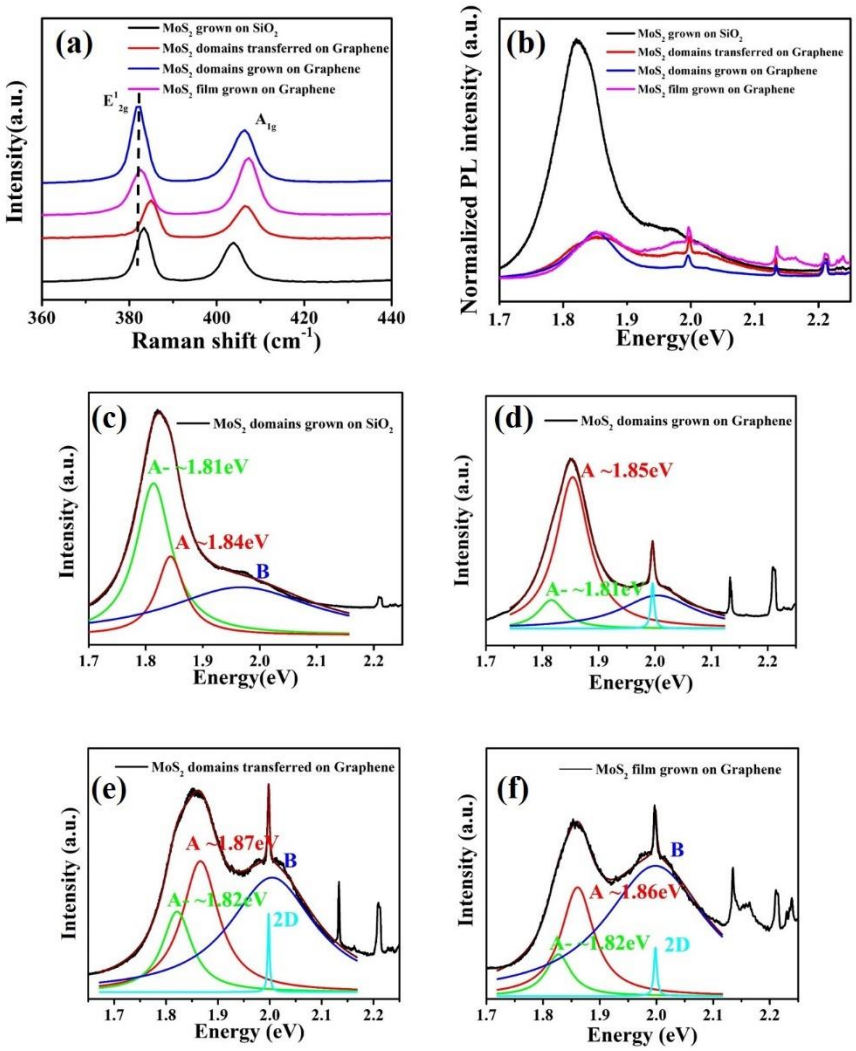

Figure 4.5. Raman and PL study on MoS_2 on Si/SiO_2 and graphene substrate (a) Raman spectra of MoS_2 domains grown on SiO_2, MoS_2 domains transferred on graphene, MoS_2 domains grown on graphene and MoS2 film grown on graphene respectively. The dashed black line indicates the shift of E^1_{2g} and A_{1g} peak between spectra; (b) PL spectra of MoS_2 domains grown on SiO_2, MoS_2 domains transferred on graphene, MoS_2 domains grown on graphene and MoS_2 film grown on graphene respectively; (c-f) Multipeak fits to the PL peak of MoS_2 with subpeaks corresponding to B excitonic transition (B), the neutral excitonic transition A (A) and the charged excitonic transition of A (A-).

Based on the best quality MoS_2 film I obtained via controlling the parameter (**Figure 4.4(e)**), I then planned to study the quality of as synthesized MoS_2 film. Raman and PL spectroscopy are two very useful techniques to determine the layer number, as well as to investigate other effects such as lattice strain, doping levels and interfacial van der Waals interactions between different 2D materials. [98] In Raman spectrum of MoS_2, E^1_{2g} and A_{1g} peak represent two characteristic vibration modes. [244] E^1_{2g} mode is related to the in-plane vibration of Mo and S atoms, while the A_{1g} mode refers to the out-of-plane vibration of S atoms. [245] In order to determine the layer number and lattice strain of the continuous MoS_2 film grown on graphene, I compared the Raman spectrum with monolayer MoS_2 domains grown on graphene, monolayer MoS_2 domains grown on SiO_2/Si using similar CVD method and transferred monolayer MoS_2 domains from SiO_2/Si to graphene. The Raman spectra are presented in **Figure 4.5(a)**, with an excitation wavelength of 532nm. The frequency difference between E^1_{2g} and A_{1g} peak could help to determine the layer number of MoS_2. [245] The fitting result shows that for MoS_2 film grown on graphene, the center of E^1_{2g} and A_{1g} peak located at ~382.4cm^{-1} and 407.0cm^{-1} respectively, while the two peaks of monolayer MoS_2 domains grown on graphene centered at ~382.1 cm^{-1} and 406.5 cm^{-1}. They both have a similar frequency difference ~24.5cm^{-1}, which proves that the continuous MoS_2 film produced on graphene was monolayer. However, it should also be noticed that the frequency difference of monolayer MoS_2 transferred onto graphene was relatively smaller. E^1_{2g} peak shew a significant blue shift to ~385 cm^{-1} while the position of peak remained ~

406.5 cm^{-1}.I speculate that this phenomenon results from the lattice strain of MoS_2, as previous studies reported that the position of E^1_{2g} peak could be easily affected by the built-in strain of MoS_2 whilst A_{1g} peak is less influenced.[246] The lattice mismatch between MoS_2 domains and graphene of CVD grown MoS_2 introduced lattice strain in MoS_2 domains and films. On the other hand, the transfer process released potential strain in CVD grown MoS_2 domains. This conclusion is also supported by the blue shift of E^1_{2g} peak of MoS_2 film grown on graphene compared to the oriented MoS_2 domains grown on graphene. In previous discussions on the growth mechanism of MoS_2 film on graphene, I discovered that initially MoS_2 domains were formed on graphene in oriented pattern, followed by non-oriented growth. The non-oriented growth reduced part of the lattice strain coming from the lattice mismatch, resulting in the blue shift of E^1_{2g} mode.

I also studied the photoluminescence (PL) of monolayer MoS_2 in different conditions, as depicted in **Figure 4.5(b)**. All the PL spectra were normalized against the Raman intensity. For PL spectra of MoS_2 either grown or transferred on graphene substrate, the PL peak intensity was dramatically quenched compared to that on SiO_2 substrate. The quench indicates that the MoS_2 displays effective interlayer coupling and electronic interaction with graphene substrate. The photo-excited electrons and holes from monolayer MoS_2 could efficiently transfer to graphene and combine rapidly through nonradioactive recombination, leading to the PL quench.[247] Furthermore, I performed the peak fitting on PL spectra based on Lorentz peak function to show the relative photoluminescence quantum efficiency between samples. As depicted in **Figure 4.5(c-**

f), the PL spectra of MoS_2 have three subpeaks which correspond to A, A- and B peaks according to previous researches.[106] The peak A and B corresponds to the direct transition from conduction band to two spin-orbit split valence band at the K point. The peak A-, located at slightly lower energy than A peak, is associated with the recombination of negatively charged excitons of trions A-. The trion A- arise from a free electron bounded to a neutral exciton via Coulomb interaction as MoS_2 could be easily negatively doped by contamination or contact with substrate.[248]

By comparing the integrated A and A- PL peaks of all four samples, I noticed that the PL intensity ratio of A to A- (A/A-) were different. The A/A- ratio indicated the relative populations of neutral and charged A excitons. In the PL spectra of MoS_2 grown on SiO_2, the PL peak was dominated by A- peak, revealing high degree of charged impurities from SiO_2 substrate, in agreement with previous studies. [207] On the contrary, for the other three samples of MoS_2 on graphene substrate, the A/A- ratio was much higher. This indicated that graphene could conduct away charged impurities and act as P-doping agent for MoS_2. Higher A/A- ratio indicated higher P-doping level as well as stronger interfacial interaction between MoS_2 and graphene. It was found that among three MoS_2/Graphene samples, MoS_2 domains directly grown on graphene had highest A/A- ratio, followed by directly grown MoS_2 film on graphene and transferred MoS_2. This sequence matches with the Raman study of built-in strain in MoS_2. Moreover, a red shift of A peak could be observed alongside with the decrease of A/A- ratio. Other studies suggest that uniaxial tensile strain could not only influence the Raman spectrum

but reduces the band gap of MoS_2 and therefore cause the red shift of A exciton peak, which further supports the observation. [249]

Besides the change in A and A- peak, the change in B peak is also worth mentioning. Comparing to the B peak in MoS_2 domains grown on graphene, the B/A ratio of MoS_2 domains transferred on graphene and MoS_2 film grown on graphene were much higher. In other words, the PL quench was less effective in the B peaks of these two samples. As is mentioned before, the quench results from the nonradioactive recombination of photo-excited electrons and holes. Therefore, I speculate that the increased B/A ratio is due to weaker coupling between MoS_2 and graphene layer. In the case of transferred MoS_2 on graphene, the decoupling derives from interlayer impurities introduced during transfer process. While for CVD grown MoS_2 film on graphene, the oxidation of graphene underlayer increased the number of defects and surface roughness of graphene, leading to the decoupling. However, it is still not clear why the A peak seems to be less influenced than B peak. As so far there is very few studies on the factors that may cause the evolution of B peak intensity in monolayer MoS_2, further studies would be worthwhile in future.

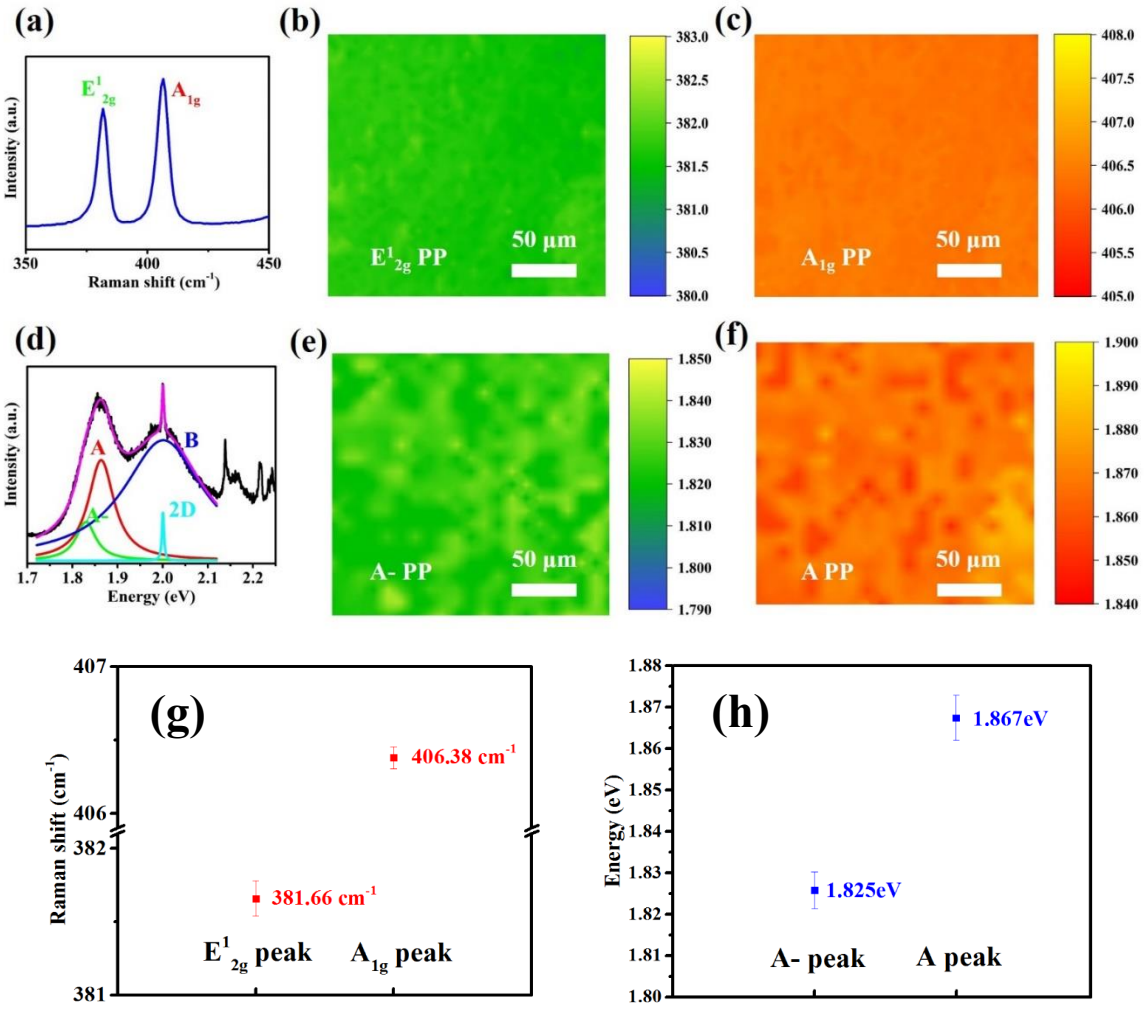

Figure 4.6. PL and Raman measurement of as–grown MoS_2 film on graphene. (a) Raman spectrum of as-prepared sample; (b-c) Raman maps (200µm × 200µm) of the continuous MoS_2 film grown on Graphene, showing (b) E^1_{2g} peak position; (c) A_{1g} peak position; (d) PL spectrum of as-prepared sample; (e-f) PL mappings of the continuous MoS_2 film grown on Graphene showing (e) A- peak position and (f) A peak position.(g-h) Average peak position of different peaks in Raman and PL measurement.

In addition, the PL and Raman spectra could help to evaluate the areal uniformity of as synthesized continuous MoS_2 film on graphene via PL and Raman mappings. **Figure 4.6(c-d)** presents the Raman integrated mappings corresponding to E^1_{2g} and A_{1g} peak

position, obtained on a typical region of 200μm × 200μm. The average position of E^1_{2g} peak was 381.66 cm^{-1} with a standard deviation of 0.12 cm^{-1}. The average position of A_{1g} peak was 406.38 cm^{-1} with a standard deviation of 0.07 cm^{-1}. **Figure 4.6(e-f)** show the PL mapping of the peak position of A and A- on the same region. The average position of A- peak was 1.825 eV with a standard deviation of 0.044 eV. The average position of A peak was 1.867 eV with a standard deviation of 0.0054 eV. Both mappings show good uniformity among the measured area and the peak positions match with the previous discussion, proving high quality and uniformity of the MoS_2/Graphene film produced.

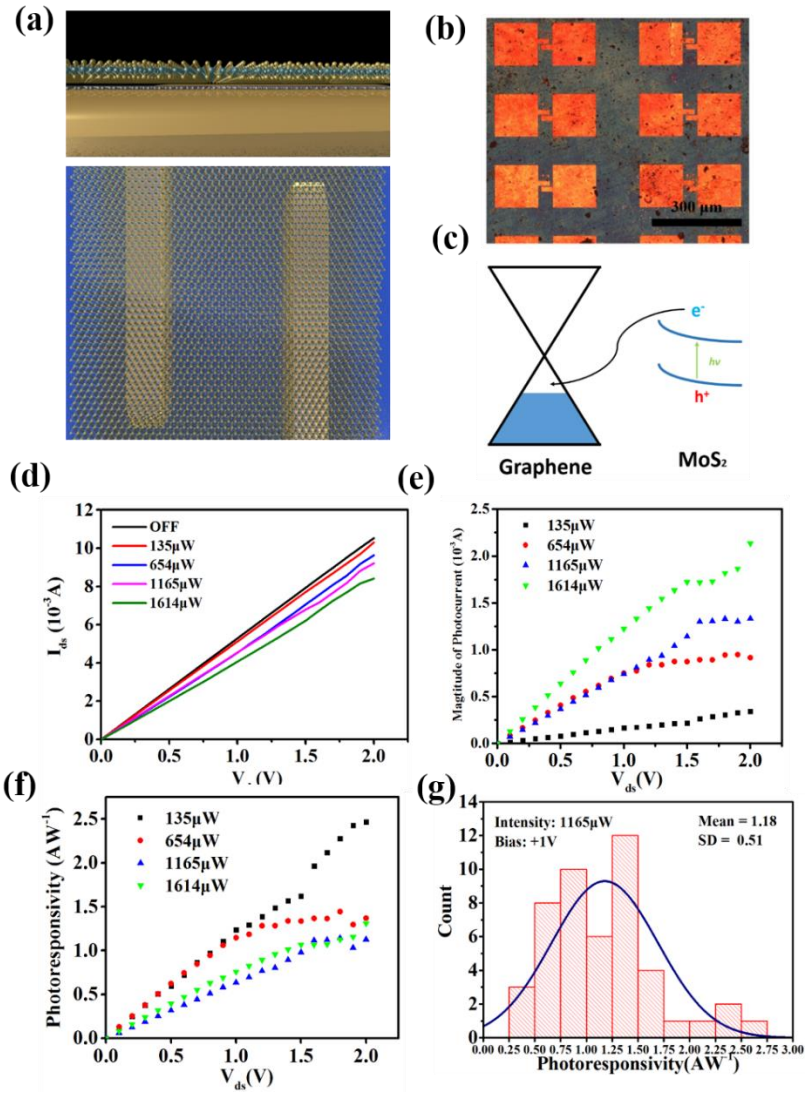

Figure 4.7. Photodetector fabricated by all CVD grown MoS_2 film/Grapene heterostructure (a) Schematic illustration of side view and top view of photodetector devices fabricated by CVD grown MoS_2/Graphene film; (b) Optic image of as fabricated devices. The photo image of device chip is presented in **Appendix, Figure 1**; (c) Band diagram explaining the photo electron transfer; (d) I-V curve of as fabricated dievice under various illumination; (e) Magtitude of photocurrent of as fabricated device under various illumination; (f) Photoresponsivity of as fabricated device under various illumination as a function of bias voltage; (g) The statsitic distribution of

photoresponsivity of as fabricated devices under 1V bias with an incident light intensity of 1165 μW.

In order to characterized the optoelectrical properties of the all CVD grown MoS_2 film/Graphene heterostructure, I fabricated a simple photodetector. **Figure 4.7(a)** and **7(b)** is the schematic illustration and optical image of photodetector device I fabricated using CVD grown MoS_2/Graphene film. To fabricate the device, MoS_2/Graphene film was directly transferred onto a SiO_2 (300 nm)/p++ Si substrate (University Wafer) with predeposited gold pads, which used the method reported in previous studies. [250] The gold pads directly contacted with graphene film, acting as electrodes.

To study the photoresponse of as fabricated device, source-drain voltage was applied on gold electrode pairs and I-V measurements were carried on the device under dark and four different illumination circumstances. **Figure 4.7(c)** shows the plots of photocurrent verses applied source-drain voltage. When the laser was off, the I-V plot shw a linear curve, indicative of good contact between gold electrodes and MoS_2/Graphene film. By emitting laser on the photodetector, I observed that the response current was decreased. This phenomenon can be explained by a photoinduced electron transfer from MoS_2 to graphene. Previous studies have proved that the graphene film transferred onto SiO_2/Si using the method in this work is p-doped. [251] When no gate voltage is applied, drain current in the graphene FET is dominated by holes. When the FET is illuminated with visible light, photoinduced electrons inject from MoS_2 to graphene which reduces the current. [252] (**Figure 4.7(d-e)**)

Photoresponsivity(R) and photogain(G) are two important figure of merits to evaluate the performance of photodetectors. [253-254] Photoresponsivity is a measure of device's electrical response and can be defined as $R = \frac{I_{photo}}{P_{laser}}$, where I_{photo} is the photocurrent and P_{laser} is the collected illumination power. In my case, the photo-induced current is negative therefore I define the current change as the photocurrent I_{photo}. In **Figure 4.7(f)**, I present the calculated R of the device as a function of V_{ds} under different illumination intensity. Under all incident power density, R showed an increasing trend with a larger applied bias. The largest R measured could reach over 2.4 A/W with 3.3×10^{-4} A photocurrent under 135 μW illumination at +2 V bias. Photoresponsivity could also be expressed by a function of photogain as

$$R = \eta_{ext} Ge/hv$$

Where η_{ext} is the external quantum efficiency, e is the elementary charge unit, and $v = c/\lambda$ is the frequency of incident light. I assume that $\eta_{ext} = 8.1\%$, as the absorbance of the MoS_2/graphene film is ~8.1% at 532 nm, measured by absorption spectroscopy. The calculated photogain of the device could reach up to 69 under P_{laser} = 135 μW and V_{bias} = 2 V, thanks to high electron mobility and photoconductive effect.

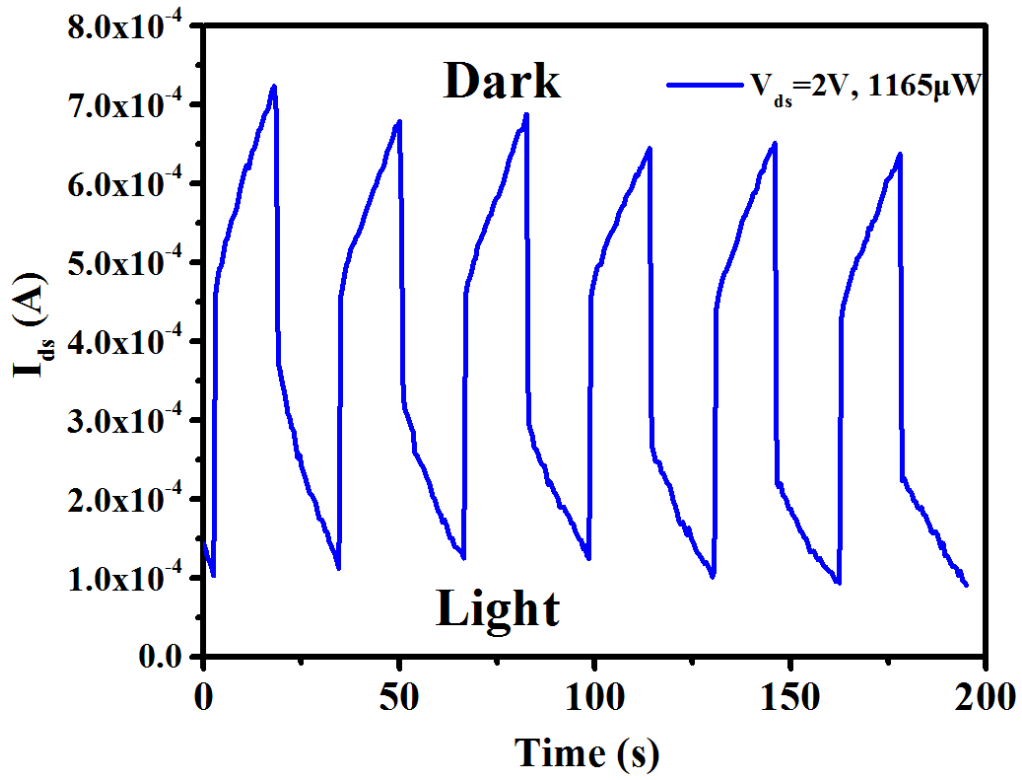

Figure 4.8. Transient photocurrent characteristics obtained from MoS_2/graphene device. The measurement was performed under +2V bias and 1165μW illumination.

I measured the time-resolved photoresponse of one of the MoS_2/Graphene devices at a fixed bias of 2 V with an incident light intensity of 1165 μW, shown in **Figure 4.8**. Reproducible high and low impedance states could be obtained by repeated cycles of on-off states of light irradiation. Also, to evaluate the uniformity of the performance of as fabricated devices, I measured 50 devices within ~8 mm^2 effective MoS_2/Graphene film area I transferred, among them 48 of them have sufficient MoS_2/Graphene coverage and clean surface to make working devices. The success rate was 96%. The statistic distibution of photoresponsivity of the devices is presented in **Figure 4.7(g)**. The average photoresponsivity is about 1.18A/W and the standard deviation is 0.51.

The result exhibited acceptable uniformity in the performance of as fabricated devices. It should be awared that the scattering of photoresponsivity data was relatively higher than the achieved uniformity. The main reason of the discrepancy is due to the processing and measurement of the devices. Since that these devices were fabricated by polymer-assisted transfer method, contaminations may inevitably introduced into the system. Besides, during the measurements, the probes need to pierce MoS_2/graphene film to contact with gold electrodes, this leads to possible contamination between probe tips and gold electrodes, resulting in high deviation.

These photodetectors with direct CVD grown MoS_2/Graphene film exhibited high photoresponsivity and photogain in absence of applied gate potential under ambient environment, comparing to other studies with similar design of device. Lin et al.[44] demonstrated a responsivity of 79mA/W when P_{light} = 40μW and bias = 1V on a directly grown MoS_2/Graphene/SiC heterostructure. Liu et al.[255] observed that on a printable MoS_2/Graphene heterostructure a photresponsivity of 835mA/W could be achieved under P_{light} of 0.05mW/cm^2 and bias of 5V. My device exhibits at least 1- order improvement of photoresponsivity. I also noticed that the photoresponsivity of MoS_2/Graphene heterostructure could reach up to 10^7 A/W with a comb-shape drain-source pair. [235] This reminds us that the performance of the directly CVD grown MoS_2/Graphene heterostructure is likely to be further improved with modified device design, which is worthy of further studies in future.

4.3 Conclusion

In summary, I have demonstrated a simple approach to directly synthesize a large area

of continuous monolayer MoS_2 film on graphene substrate by a two-step CVD process with aids of hydrogen under ambient pressure. I discovered that oxidation of graphene is one of the important factors that hinders the formation of MoS_2 film on graphene during long time CVD process. Graphene can be effectively protected from being oxidized by adding hydrogen into the carrying gas. Centimetre-scale continuous MoS_2 film were grown on graphene susbtrate with an appropriate nucleation rate, growth time and hydrogen concentration. The film's microsctructure and thickness were characterized by PL and Raman measurement, suggesting that the MoS_2 film is monolayer. I also fabricated a simple photodetector based on MoS_2/Graphene film, exhibiting high photo current, photoresponse reaching up to 2.4 A/W and photogain reaching up to 69. This approach shows a potential for scalable fabrication of high performance optoelectronics based on 2D Van der Waals heterostructures.

Chapter 5

High Photoresponsivity in Ultrathin 2D Lateral Graphene:WS_2:Graphene Photodetectors Using Direct CVD Growth

5.1 Introduction

Ever since single layer graphene was first isolated by mechanical exfoliation, the study on two-dimensional materials has been greatly simulated. [1, 6] Among the family of two-dimensional materials, semi-metal graphene was most widely studied due to its excellent conductivity which makes it an ideal material for contacts and interconnections. [256-257] Other two-dimensional materials also came into people's sight including insulator hexagonal boron nitride (h-BN), [224, 258] semiconductors such as black phosphorus [259-260] and transition metal dichalcogenides (TMDs). [131, 225, 261-262] Furthermore, the heterostructures based on these materials have gradually drawn people's attention as they are considered as important building blocks for next generation nano-scale electronic and optoelectronic devices. [198, 236, 263-270]

There are primarily two types of heterostructures: vertically stacked heterostructures, [190, 197, 271] and laterally stacked heterostructures. [272-274] The vertical heterostructures are usually accomplished by vertically stacking two-dimensional materials using mechanical transfer. [74, 231] However, scalable fabrication could hardly be achieved by such method. Recent studies have shown the possibility to fabricate various vertical heterostructure by direct CVD growth including WS_2:h-BN, [205] MoS_2:graphene, [208]

MoS_2:WS_2, [275] and etc. [276] Nevertheless, not only these methods are challenging, it is hard to control the continuity and uniformity of the as grown heterostructure film which hinders their applications in industrial production.

Most recently, several groups have explored direct CVD synthesis of lateral heterostructure such as MoS_2:graphene, [214] WS_2:graphene, [215] and WSe_2:graphene. [216] Field-effect transistors (FETs) could directly developed from as grown heterostructure. Smaller and more controllable device size could be achieved by controlling the topology of graphene ribbon. Also, lower intrinsic contact resistance could be obtained from stronger connection between graphene and TMDs. These two benefits make the CVD-synthesis lateral heterostructures appealing building blocks of 2D circuits.

However, most studies on direct CVD synthesis of lateral heterostructure use sapphire as growth template. [215-216] As the sapphire wafer is very costly, Si wafer is considered to be a better substrate for manufacture purpose. There is a need to develop an approachable method to fabricate lateral-heterostructure based devices directly on Si wafer. Besides, as a promising candidate for next generation 2D opto-electronics, Gr:TMD:Gr lateral heterostructure synthesized by direct CVD growth method is supposed to improve the overall performance of light detection and light harvesting devices.

Here I demonstrate the selective CVD synthesis of WS_2 stitching to pre-patterned multilayer graphene (2-3 layers) under ambient pressure. WS_2 serves as the channel material of n-type FET. Due to the high reaction temperature of WS_2 synthesis, as well as other TMDs such as MoS_2 and WSe_2, the pre-patterned graphene could be easily

damaged by oxidation. This factor is more significant on Si wafer since at the reaction temperature (1000 °C) the Si oxide layer would decompose. I discovered that graphene could be well protected when hydrogen was introduced into the reaction system. The opto-electronic property measurements were then carried on as fabricated Gr:WS_2:Gr device. By comparing the performance of similar device fabricated by wet transfer method, I discovered that the on-off ratio and photoresponsivity was significantly improved due to better contact between graphene and WS_2.

5.2 Results and Discussion

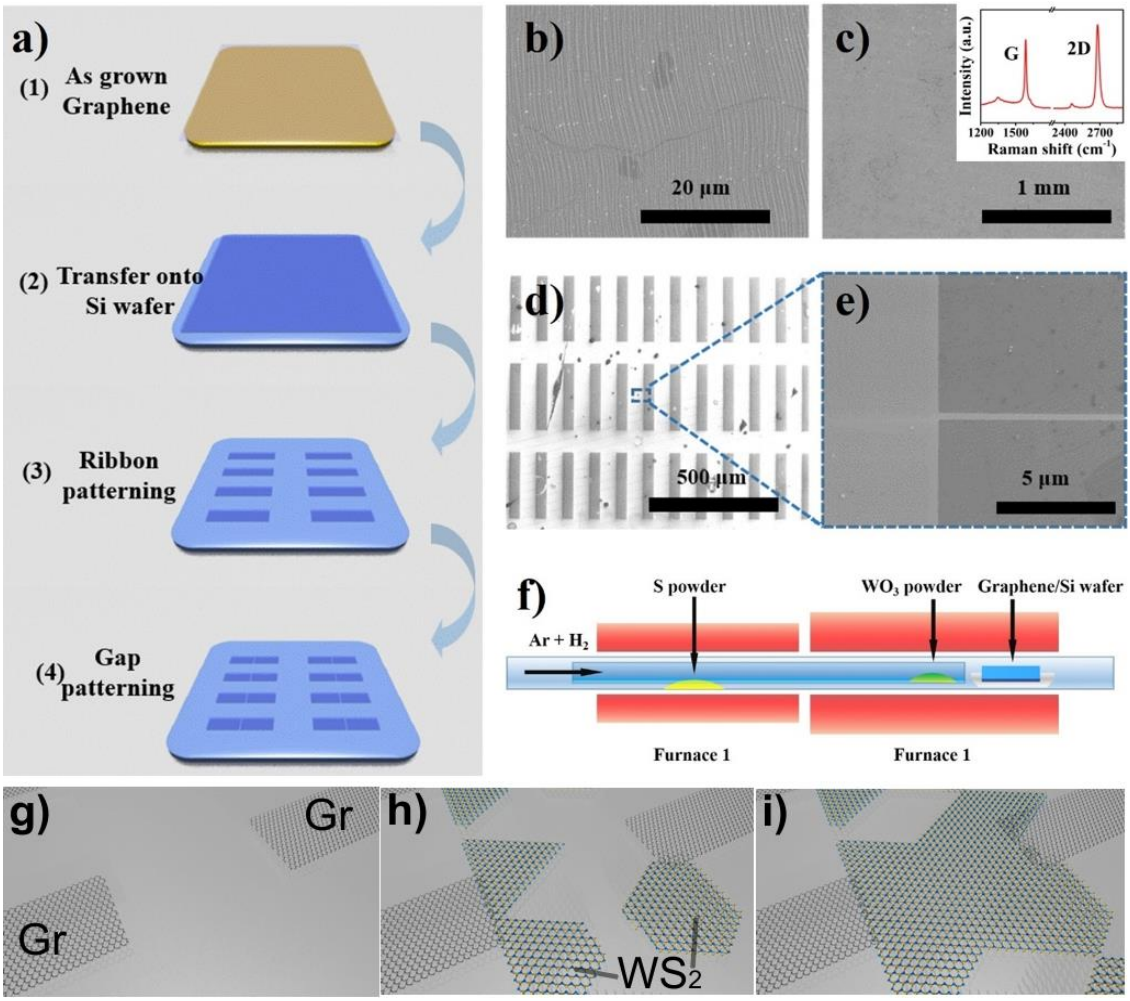

Figure 5.1 Preparation of sample. (a) Schematic illustration of the preparation process of graphene ribbon substrate. (b-e) SEM images of (b) as grown graphene. The wrinkle that could be observed results from the difference in coefficient of expansion of graphene and copper during the cooling stage in CVD process; (c) As-transferred graphene on Si chip. The embedded figure is the Raman spectrum of as-transferred graphene; (d) As patterned graphene ribbon and (e) Graphene ribbon with small gap in the middle; (f) Schematic illustration of CVD system; (g)-(i) Schematic illustrations showing the WS_2 growth between the graphene gap electrodes.

The first step to fabricate Gr/WS_2/Gr heterostructure is to prepare graphene ribbon with gap in the middle. Here I present a simple route with help of electron beam lithography (EBL), shown in **Figure 5.1(a)**. I started from CVD-grown graphene film on copper foil (**Figure 5.1(b)**). First, I transferred graphene on SiO2 (300 nm)/p++Si substrate (University Wafer) using wet transfer method. (**Figure 5.1(c)**) Then EBL was applied with aids of positive resist (PMMA 485 A4) to pattern as-transferred graphene into graphene ribbons. (**Figure 5.1(d)**) Afterwards, another EBL process with aids of positive resist (PMMA 950 A3) was applied to pattern the gap (~1μm)

A two-furnace CVD system was used to synthesize WS_2 in graphene gap, as depicted in **Figure 5.1(f)**. 200 mg Tungsten trioxide (WO_3) and 300 mg Sulfur powder (S) were used as precursors. Sulfur powder and WO_3 powder were placed in the middle of front and back furnace, respectively, for precise temperature control, while the temperature of substrate could be tuned by the distance from the center of Furnace 2. Different from conventional CVD process, the whole reaction was carried in Argon and Hydrogen mixture atmosphere under ambient pressure. I introduced hydrogen into CVD system for two reasons. First, as was reported before, Hydrogen could help to further reduce WO_3 precursor. As a result, the amounts of effective reactants increase in the system, which enhance the nucleation density and coverage of WS_2 during the CVD process. [153] Second, Hydrogen could act as a reducing agent that reacts with reactive O atoms released from SiO_2 decomposition at high temperature and therefore could prevent graphene from oxidation and degradation.

Similar to the CVD method previously reported, [277] I designed a multiple-step CVD

process with three stages. (1) Heating up Furnace 1 and Furnace 2 to 180 °C and 1000 °C respectively from room temperature with a mixture gas of 240 sccm Ar and 10 sccm H_2 gas flow. The two temperature correspond to actual temperature of S and WO_3 precursor during the reaction. (2) Main nucleation and growth stage of WS_2 started when two furnaces reached target temperature; (3) when the growth stage ended, the reaction was stopped by cooling furnace 2 down to 900 °C. Afterwards, furnace 1 was heated up to 400 °C and Ar flow rate was set to 490 sccm to blow away surplus S powder. Then both furnaces were set to room temperature for fast cooling.

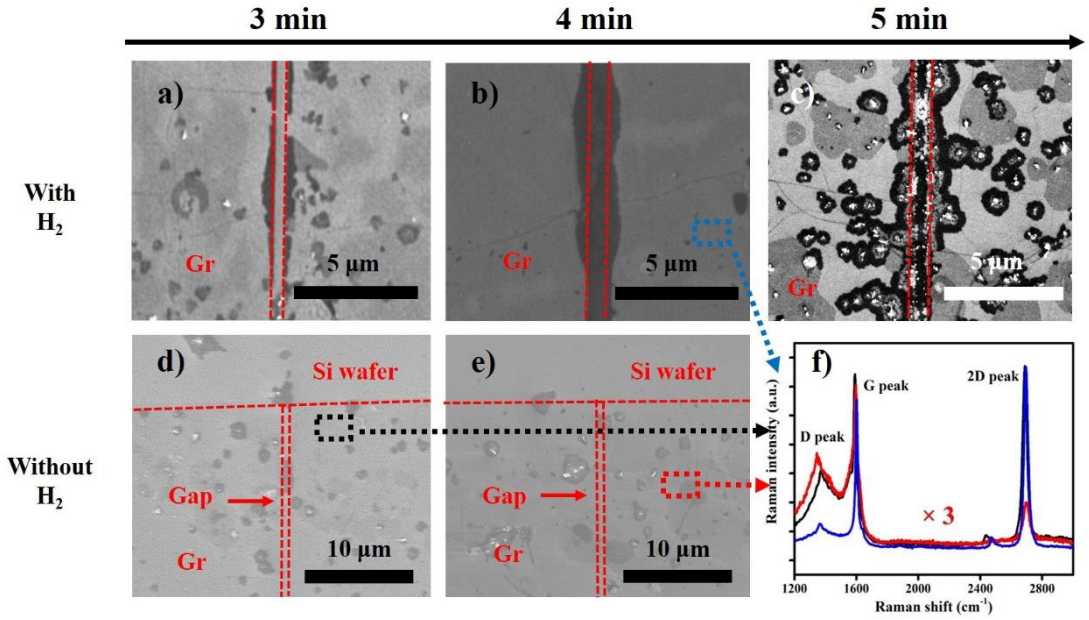

Figure 5.2 Influence of growth time on the topography of WS_2. (a - c) SEM images of as grown WS_2:graphene in Ar/H_2 atmosphere. The growth time was 3 min (a), 4 min (b) and 5 min (c) respectively; (d-f) SEM image of as grown WS_2: graphene in Ar atmosphere. The growth time was 3 min (d) and 4 min (e) respectively. (f) Raman spectra of post-growth graphene shown in (b), (c) and (d).

By altering growth time, I hoped to figure out the ideal parameter to enable lateral growth of WS_2 within graphene gap, as is shown in **Figure 5.1(g-i)**. During my attempts to narrow down growth parameter and optimize WS_2 growth condition, I discovered that different growth time could result in various topography of WS_2. As is shown in **Figure 5.2(a)**, selective growth could be observed that at the beginning stage of CVD growth. WS_2 tended to nucleate at the edge of graphene ribbons, although little nucleation also took place on the surface of graphene ribbon. This is because that the edges of graphene ribbon could provide abundant heterogeneous nucleation site rather

than on the surface of graphene. As the growth stage continued, the nucleuses gradually grew laterally to fill the gap between graphene, shown in **Figure 5.2(b)**. Upon further extending the growth time, 3D WS_2 crystals (white crystal clusters) started to form on the surface of WS_2 and graphene (**Figure 5.2(c)**), while lateral growth of WS_2 on graphene was prohibited.

It should be noticed that the presence of hydrogen is essential to successful synthesis. In the comparison experiments without presence of hydrogen, I discovered that the quality of graphene could be damaged. **Figure 5.2(f)** shows the Raman spectra of post-growth graphene undergoing different growth process. After 4 min growth in Ar/H_2 atmosphere (**Figure 5.2(b)**), only a small D peak could be observed in the Raman spectrum (blue line), indicating minor degradation in the graphene ribbons. The damage was likely due to the inevitable thermal degradation during high temperature reaction as it could also be observed on other CVD processes on sapphire substrate.[216] On the other side, after 3 min growth in Ar atmosphere, a strong d peak could be observed in the spectrum (black line). Comparing with as-transferred graphene, the D/G peak intensity ratio rises from 0.22 to 0.48, suggesting severe damage to the graphene. After 4 min growth in Ar atmosphere, the intensity of spectrum (red line) significantly decreases. The relative intensity of 2D peak comparing to G peak (2D/G) also dropped from 1.2 to 0.33, indicating further degradation of graphene ribbons. [278] The presence of hydrogen could keep the damage to lowest level.

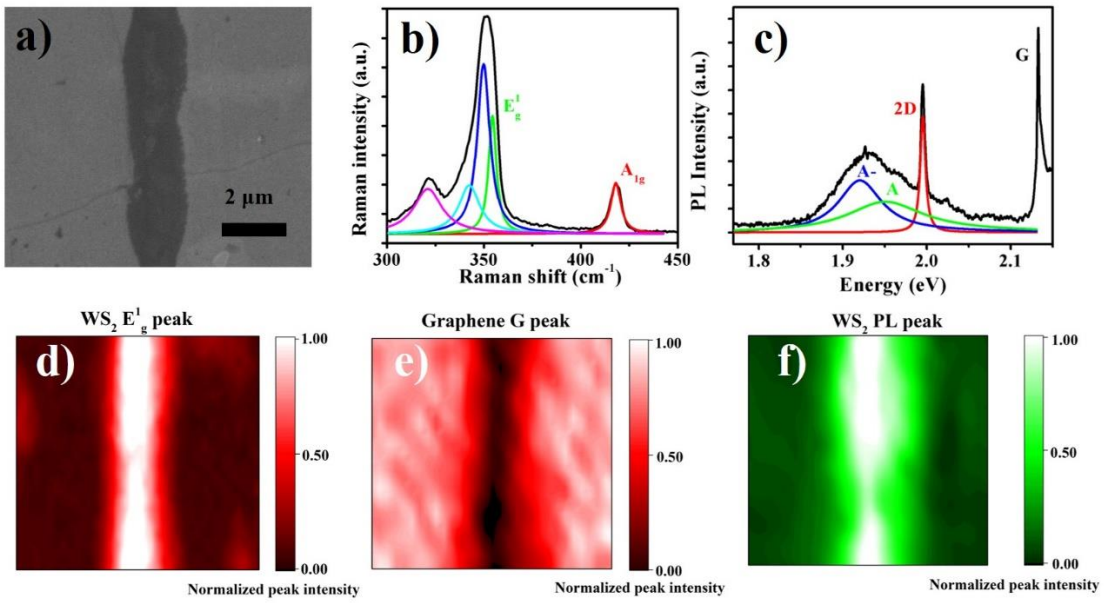

Figure 5.3 Characterization of Gr/WS_2/Gr heterostructure. (a) SEM image of as-prepared Gr/ WS_2/Gr heterostructure; (b) Raman spectrum of WS_2 grown in graphene gap; (c) PL spectrum of WS_2 grown in graphene gap; (d) Mapping of WS_2 E^1_g Raman peak near the gap; (e) Mapping of graphene G Raman peak near the gap; (f) Mapping of WS_2 PL peak near the gap.

Based on the best quality Gr:WS_2:Gr heterostructure I obtained via controlling the parameter, I then planned to characterize the quality of as synthesized heterostructure. Raman and PL spectroscopy are two very useful techniques to determine the quality and layer number of WS_2.

In the Raman spectrum of WS_2, E^1_g and A_{1g} peak represents two characteristic vibration modes. E^1_g mode is related to the in-plane vibration of W and S atoms, while the A_{1g} mode refers to the out-of-plane vibration of S atoms. The intensity ratio of E^1_g and A_{1g} peak was between 1 and 2, indicating that the WS_2 grown in graphene gap was mono- or bi-layer.

I also performed PL spectroscopy measurement on WS_2 grown in the graphene gap. As the gap is smaller (~500 nm) comparing to laser spot size (2 μm), I inevitably observed the G and 2D Raman peak of graphene in the PL spectrum of WS_2. Also, due to the low effective area of WS_2, the intensity of WS_2 PL peak was also relatively weak comparing to graphene Raman peaks. However, sufficient WS_2 PL response could still be obtained. (**Figure 5.3(c)**). In order to study the property of as grown WS_2, the WS_2 signal was then deconvoluted into separate peaks by fitting two Lorentzian curves, exciton emission (A), at ~1.95eV and negative trion emission (A-), at ~1.92eV. The PL intensity ratio of exciton to trion (A/A-) was very low (~0.56), indicating a high level of doping, probably from graphene and oxide impurities from SiO_2 decomposition. [278]

Based on the difference in the Raman spectra of graphene and WS_2, Raman and PL mapping could help to determine the uniformity of graphene and WS_2 near the gap area. In **Figure 5.3(d)**, **(e)** and **(f)**, I could spot a distinctive gap in both mappings. This proved the formation of Gr:WS_2:Gr heterostructure.

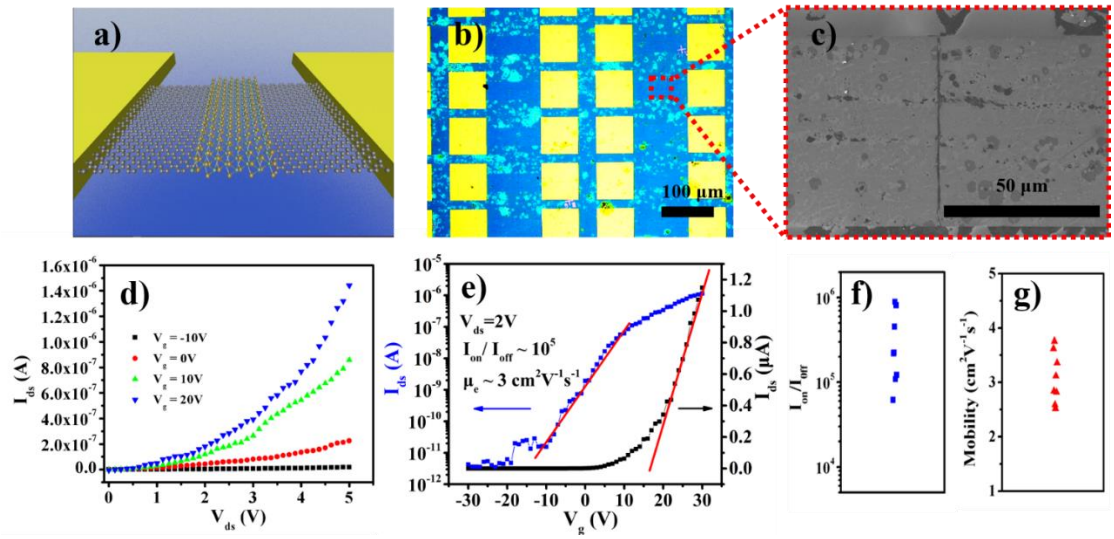

Figure 5.4 Electrical properties of Gr:WS_2:Gr heterostructure. (a) Schematic illustration of Gr: WS_2:Gr FET; (b) Optic image of as fabricated FET array; (c) SEM image of framed region (red dotted line) in (b); (d) I-V characterization of as fabricated device under different gate voltage; (e) I-V_g curve obtained under 2V bias; (f) Statistics result of on-off ratio of eight measured FET devices; (g) Statistics of mobility performance of eight measured FET devices.

To evaluate the electrical and opto-electrical properties of as fabricated Gr:WS_2:Gr heterostructure, a simple field effect transistor (FET) was fabricated. **Figure 5.4(a)** is the schematic illustration of the side view of the photodetector devices I fabricated. To make the device, the Gr:WS_2:Gr heterostructure was directly transferred onto a SiO_2 (300 nm)/p++ Si substrate (University Wafer) followed by depositting gold pads. The gold pads directly contacted with graphene film, acting as electrodes. By aligning the bond pad with Gr: WS_2:Gr heterostructure, an array of FET devices were made, shown in **Figure 5.4(b)**. **Figure 5.4(c)** is the SEM image of Gr:WS_2:Gr junction, showing a channel length of 1μm and a channel width of 50 μm.

The electrical properties of Gr:WS_2:Gr FET were measured as ambient pressure with and without gate bias. **Figure 5.4(d)** shows the I-V measurement under various gate bias applied through a heavily p-doped silicon under 300 nm SiO_2 layer. The I-V plot exhibited a nonlinear curve, indicating of Schottky contacts at metal-semiconductor interface of graphene ribbon and WS_2. It could also be observed that the current rose with increasing gate voltage, indicating an N-type semiconductor behaviour. This is further proved by a gate sweep measurement presented in **Figure 5.4(e)**. The black curve exhibited a well-defined N-type transistor behaviour with a threshold voltage (V_{th}) of ~10V. From the I-V_g curve, I could extract the field-effect electron mobility (μ_{FE}) by following equation:[153]

$$\mu_{FE} = \frac{dI_{ds}}{dV_g} \times \frac{L}{w} \times \frac{1}{V_{ds}} \times \frac{1}{C_{ox}}$$

where $\frac{dI_{ds}}{dV_g}$ is the transconductance, L is the channel length, w is the channel width, V_{ds} is the applied drain source bias, and C_{ox} is the gate capacitance. Judged by the performance of eight working devices among the device array, the as fabricated WS_2 FET had a FET mobility of 1.45 ± 0.18 $cm^2V^{-1}S^{-1}$, which was much higher than that of similar FET made by transfer method (~ 0.53).[153] The on-off ratio was ~10^{-5} at an applied bias of 2 V, also in agreement with previous works.[250, 279]

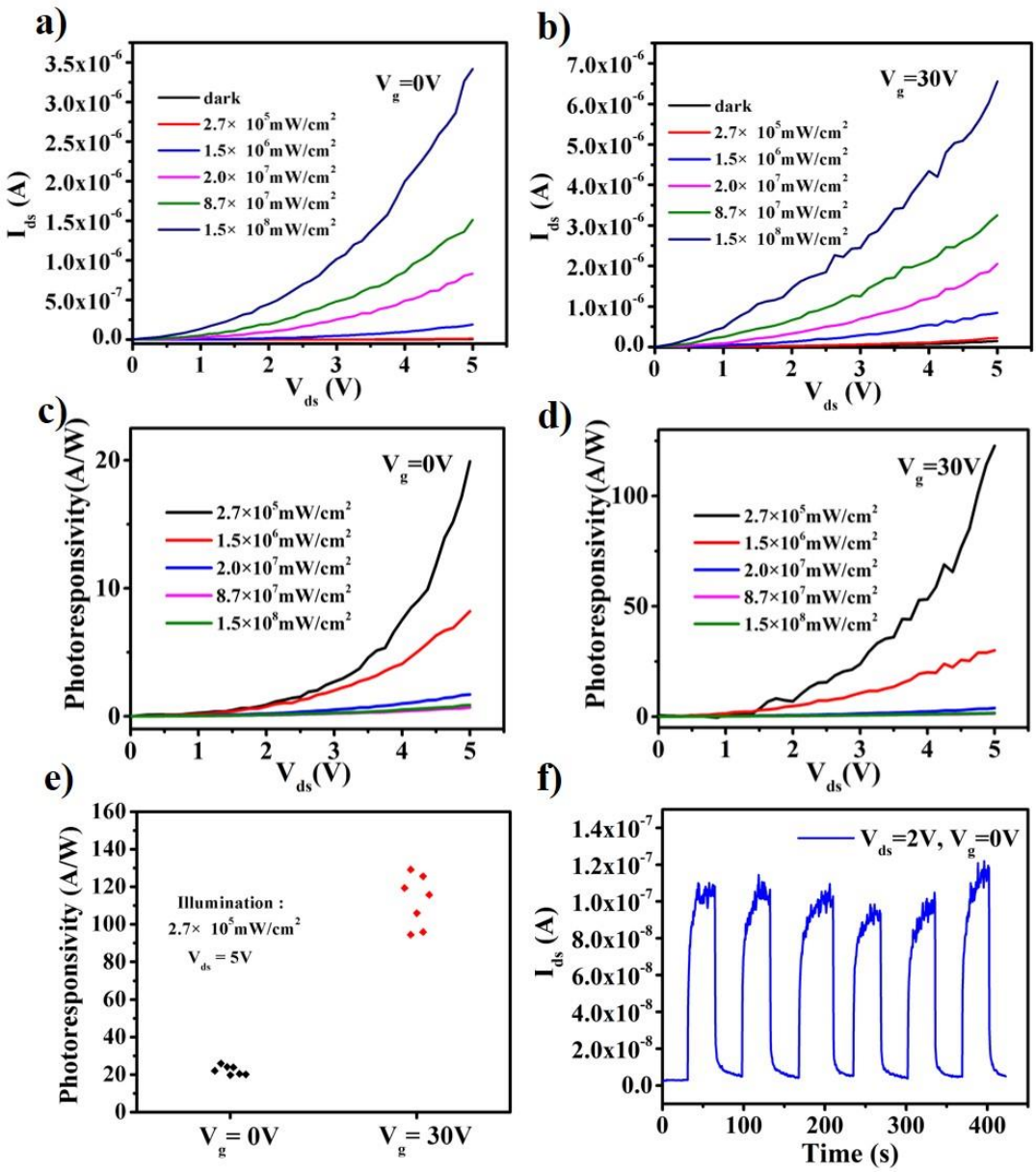

Figure 5.5 Opto-electrical properties of Gr:WS_2:Gr heterostructure. (a - b) I-V curves of Gr:WS_2:Gr FET under various illumination power with 0 V gate voltage (a) and 30 V gate voltage (b); (c-d) As calculated photoresponsivity under 0 V (c) and 30 V (d) gate voltage; (e) Photoresponsivity map of measured device under 0 V and 30 V gate voltage (f) Transient photocurrent characteristics obtained from the device under 2 V bias with an incident light intensity of 2.0×10^7 mW/cm^2;

To evaluate the photodetection performance of my devices, I-V measurements were carried on the device under dark and five different illumination circumstances. **Figure 5.5(a)** and **(b)** show the plots of photocurrent verses applied source-drain voltage under various illumination and gate voltage. By emitting laser on the photodetector, I observed that the response current was increased by increasing laser power with or without gate voltage. The I_{light}/I_{dark} ratio could reach up to ~457 without gate voltage. This suggests that my devices have promising potential in photodetection applications. Photoresponsivity(R) is an important figure of merits to evaluate the performance of photodetectors. [280] Photoresponsivity is a measure of device's electrical response and can be defined as $\mathbf{R} = \frac{I_{photo}}{P_{laser}}$, where I_{photo} is the photoinduced current defined by I_{light} - I_{dark}. P_{laser} is the collected illumination power. In my case, the photoinduced current is the current difference between dark and illuminated state. In **Figure 5.5(c)** and **(d)**, I present the calculated R of the device as a function of V_{ds} under different illumination intensity and gate voltage. Under all incident power density, R exhibited an increasing trend with a larger applied bias. I also performed a statistic measurement on seven devices, shown in **Figure 5.5(e)**. Without any gate voltage, the R was 22.3 ± 2.4 A/W under 2.7×10^5 mW/cm^2 illumination at +5 V bias. When a 30V gate voltage was applied, the R further increased as the photocurrent increases. The R I obtained was about 121.1 ± 13.8 under 2.7×10^5 mW/cm^2 illumination at +5 V bias. In addition, **Figure 5.5(f)** shows the time-resolved photoresponse of one of the working devices at a fixed bias of 1 V with an incident light intensity of 1165 μW. Reproducible high and low impedance states could be obtained by repeated cycles of on-off states of light irradiation,

suggesting reproducible and stable photoswitching characteristics.

Besides photoresponsivity, photogain is another parameter to characterize and understand the performance of photodetectors.[280] Photoresponsivity could be expressed as a function of photogain as follows:

$$R = \eta_{ext} Ge/hv$$

where η_{ext} is the external quantum efficiency, e is the elementary charge unit, and $v = c/\lambda$ is the frequency of incident light. Based on the function and photoresponsivity, I could calculate the corresponding photogain. According to the Raman and PL spectrum of embedded WS_2, I assumed that WS_2 was bi-layer. Therefore it could be speculated that $\eta_{ext} = 7\%$, as the absorbance of single layer WS_2 is ~3.5% at 532 nm, measured by absorption spectroscopy. [134] I obtain the photogain of my device could reach up to ~4030 under $P_{laser} = 2.7\times10^5$ mW/cm^2 and $V_{bias} = +5$ V.

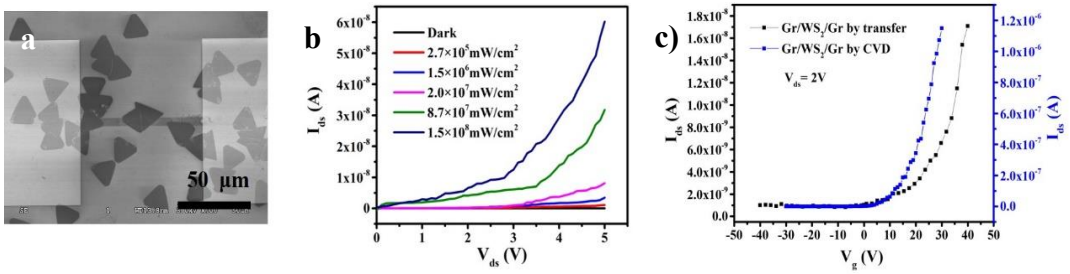

Figure 5.6. Gr/WS_2/Gr photodetectors made by transfer method (a) SEM image of a Gr/WS_2/Gr photodetectors made by transfer WS_2 triangular domains on pre-patterned graphene gap; (b) I-V curves of Gr:WS_2:Gr FET under various illumination power with 0V gate voltage; (c) I-V_g curve of device made by transfer and CVD method obtained under 2V bias.

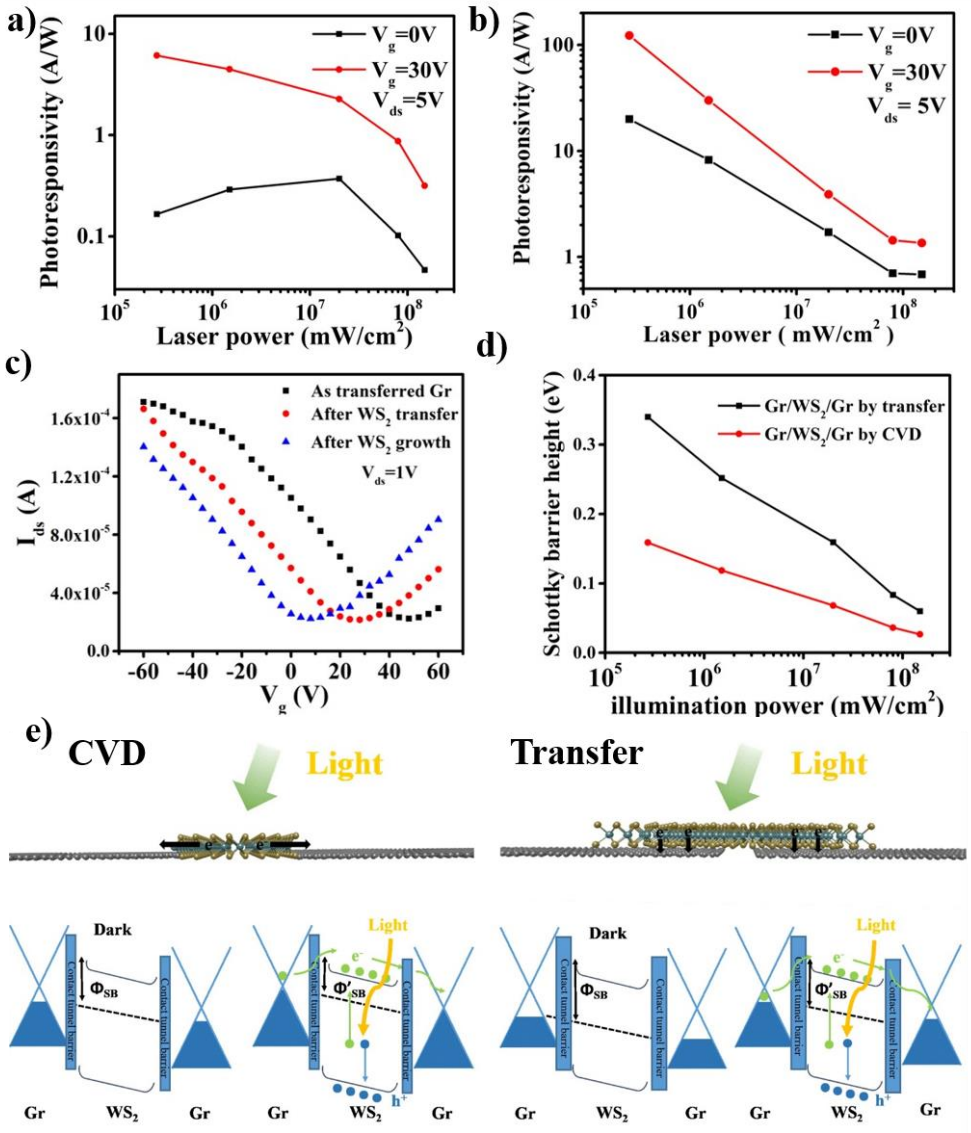

Figure 5.7 Mechanism of illumination power dependent pattern of photoresponsivity. (a-b) Illumination power dependent pattern of photoresponsivity of device made by transfer (a) and CVD (b) method; (c) Field effect measurement of as transferred graphene, graphene after WS_2 transfer and graphene after WS_2 CVD growth, using the setup shown in **Appendix, Figure 2**; (d) As calculated effective Schottky barrier height as a function of illumination power; (e) Schematic illustration of photo-doping effect and band diagram of Gr/WS_2/Gr heterostructure made by transfer and CVD method.

In order to evaluate the performace of CVD grown devices, it is necessary to make a comparison with other devices. I made a similar device using transfer method (**Figure 5.6(a)).** The electronic and opto-electronic properties were then characterized under same condition as CVD grown devices, as is illustrated in **Figure 5.6(b-c)**. It was found that the photoresponsivity and photogain of CVD grown devices were much higher. Also, It is worth noting that in previous study the Gr:WS:Gr photodetector made by transfer method exhibits different power dependent pattern under its ON and OFF state. **Figure 5.7(a)** and **(b)** shows illumination power dependent photoresponsivity of a similar device made by transfer method and a device made by direct growth method, as a function of illumination power under On (V_g= 30 V) and OFF state (V_g= 0 V). For the device made by CVD method, under both On (V_g= 30 V) and OFF state (V_g= 0 V), the photoresponsivity decreased as enhanced illumination. However the device made by transfer method shew different pattern. Under ON state, the photoresponsivity also followed a negative correlation with ullumination. While under OFF state, the photoresponsivity initially rose along with increasing illumination then decreases along with enhanced illumination.

Contact resistance between graphene and WS_2 is an important factor in 2D heterostructure opto-electronic devices. For graphene:WS_2 hybrid structure made by transfer method, polymer residues are inevitably trapped between graphene and WS_2. As the graphene:WS_2 hybrid structure was made by direct growth method, there is less impurities trapped on the contact surfce, leading to a stronger contact between graphene

and WS_2. The reduced contact resistance enables easier charge transfer between Gr and WS_2, increasing the corresponding photo induced current (I_{photo}). This contributes to high photoresponsivity and photogain.

In the 2D heterostructure devices, Schottky barrier plays an important role in the photoresponse bahaviour. Theoretically, the working function of Gr on Si wafer is estimated ~4.6 eV and the electron affinity of WS_2 is ~4.2 eV, resulting in the formation of Schottky barrier at the interface between Gr and WS_2. [251] However, when graphene contacts with WS_2, the charge transfer between graphene and WS_2 can dope the graphene and change the Fermi level as well as the Schottky barrier height. To study the doping level in graphene, I measured the dirac point position via a I_{ds}-V_g measurement with help of back gate, as is shown in **Figure 5.7(c)**. It could be observed that the as transferred graphene on Si wafer is p-doped and WS_2 has a n-doping effect on graphene, matching with previous studies. [243] Comparing to simply transferring WS_2 on to graphene ribbon, CVD growth of WS_2 had a stronger doping effect on graphene. This is possibly due to easier surface charge transfer between Gr/WS_2, as direct CVD growth method enables a cleaner Gr/WS_2 contact surface. The stronger doping effect in CVD grown Gr/WS_2 heterojunction lead to an increase in graphene Fermi level, lowering the effective Schottky barrier height. The combination of lowering contact resistance and effective Schottky barrier height resulted in the better photoresponse in the devices made by CVD method.

The effective Schottky barrier height also influences the divergence of power dependent pattern under On and Off between devices made by transfer method. When light shines

on the device, two contradictory phenomena occur. On one hand, when the illumination power increases, more electron-hole pairs are generated. As the result, the exciton recombination time decreases hence the photoresponsivity decrease. On the other hand, upon illumination the effective Gr/WS_2 Schottky barrier changes due to photogating effect. When the device is illuminated, the excitons are generated in the WS_2 channel with electrons injecting into graphene and holes remaining in WS_2. Consequently, the working function of graphene increases as well as the Schottky barrier height decrease. The reduced energy barrier allows a more efficient generation of photocurrent and higher photoresponsivity. [250, 279, 281]

Therefore, in order to further explain the relationship between photoresponsivity and illumination power, I introduce a back-to-back Schottky diode model as a simplified representation of Metal(Gr):Semiconductor (WS_2):Metal(Gr) structure to estimate the Schottky barrier height. By fitting the I-V measurement using a modified thermoionic emission equation (**Appendix, section 1**), I could extract the effective height of Schottky barrier. [216] **Figure 5.7(d)** shows the extracted effective Schottky barrier as a function of illumination power of devices made by transfer and CVD method. For the device made by CVD method, the Schottky barrier was smaller than that of the device made by transfer method. The decrease in effective Schottky barrier height was also relatively less significant. Therefore, I speculate that the photogating effect was not strong enough to compromise the decrease of exciton recombination time, leading to a negative correlation between photoresponsivity and illumination power. [250]

To conclude, **Figure 5.7(e)** is the schematic illustration of band diagram of Gr/WS_2/Gr

heterostructure made by transfer and CVD method under dark and light state. A smaller contact resistance and Schottky barrier height at CVD-grown Gr/WS_2 interface enabled increased electron transfer efficiency between graphene and WS_2, as well as the photoresponsivity. The reduced Schottky barrier also weakened the photogating effect upon illumination, resulting in different power dependent pattern of photoresponsivity from that of devices made by transfer method.

5.3 Conclusion

In summary, compared to the conventional route of using dry or wet transfer methods, constructing the heterostructure by direct CVD growth within pre-patterned graphene gaps has potential for large scale fabrication of lateral heterostructure with high quality contacts. Recent studies have attempted to directly synthesize the n-type and p-type TMD in graphene gap on sapphire substrate. However, it has been challenging to achieve the same process on Si wafer due to the degradation of SiO_2 layer and graphene during high temperature synthesis. In this work, I achieved the directly grown WS_2 in pre-patterned graphene gaps on Si wafers by using a hydrogen-aided CVD process. The reduced contact resistance and effective Schottky barrier height of directly CVD-grown WS_2:Gr junction resulted in an improved photocurrent. The I_{photo}/I_{dark} ratio (~457) and photoresponsivity (~121) are significantly higher than the photodetector with same structure under similar conditions using the conventional layer by layer wet transfer method. Since the behavior of the TMD:Gr photodetector could be tuned by the injection carrier type, I anticipate that an enhanced performance of both n-type and p-type transistors could be achieved using the similar CVD process, which paves the way to large scale construction of next generation 2D opto-electronics.

Chapter 6

Ultrathin All-2D Lateral Graphene:GaS:Graphene UV Photodetectors by Direct CVD Growth

6.1 Introduction

Since single layer graphene was successfully isolated, two-dimensional (2D) materials have drawn great attention thanks to the new properties that emerged in the 2D confinement.[1, 6, 36, 282] Transition metal dichalcogenides (TMDs) with the chemical composition of MX_2, such as MoS_2, [98, 283] $MoSe_2$, [227-284] WS_2, [91, 95, 131] and WSe_2, 226, [285-286] have become the focus of recent research due to their direct semiconducting band gap, but recent work has extended the family into 2D monochalcogenides with the form of MX. The monochalcogenides can have a layered structure, where in each layer the two bounded post-transition group III or group V metal atoms such as Ga, In are sandwiched by two layers of S or Se atoms. Like TMDs, these 2D monochalcogenides also present outstanding physical properties and show great potential in various applications. [155, 287-290] Gallium sulfide (GaS) is one of the 2D monochalcogenides that has been investigated recently. [156, 167] According to first principle calculations, layered GaS has an indirect band gap with energy ranging from 3.3 eV for monolayer GaS to 2.5 eV for 3D nanocrystals, corresponding to emission wavelengths of blue to UV. [157-158] The band gap of GaS is different than most other studied 2D materials whose band

energy is either much lower, such as WS_2 and MoS_2, or much higher, such as h-BN. [291-292] This makes GaS a favorable building block for ultrathin electronics and optoelectronics composed of 2D materials for the blue and UV regions. Previous studies suggest that there are various methods to synthesis layered GaS, including mechanical exfoliation, liquid phase exfoliation, screen printing deposition, atomic layer deposition (ALD) and chemical vapor deposition (CVD). [156, 290, 293-295] Among these methods, CVD is considered to be one of the most promising techniques to produce large area 2D GaS materials. Researchers have developed several CVD process with different precursors, such as gallium chalcogenide cubane $[(t\text{-}Bu)GaS]_4$, GaN-Bi_2S_3, and Ga_2S_3. [165-166, 296] To date, the synthesis of GaS materials by CVD has been limited to random nucleation of domains across the substrate, without specific control over the location of the GaS material. Providing seed sites on the growth substrate can help control nucleation and for devices this can be the actual electrodes. For all-2D devices graphene can serve as both the electrode and seed site for nucleation of the semiconducting 2D material.

In this study, I explore the chemistry of GaS growth with graphene electrode seeds to provide site specific nucleation. By controlling the time and precursor conditions, I show preferential GaS growth on the substrate with minimal nucleation on the surface of graphene. This results in the fabrication of lateral Graphene(Gr):GaS:Graphene heterostructures with a CVD method using SiO_2/Si chips with pre-patterned graphene electrode pairs on it. GaS is formed by reduction of Ga_2S_3 precursor in hydrogen atmosphere under ambient pressure and selectively deposited in the gaps of graphene

electrode pairs. I then characterized the electronic and opto-electronic properties of as fabricated Gr:GaS:Gr photodetectors. I discovered that 2D GaS show remarkable photoresponse behavior under ultraviolet (UV) light. This paves the way for further studies on the semiconductor properties of GaS, as well as the large-scale fabrication of GaS based electronics and opto-electronic devices.

6.2 Result and Discussion:

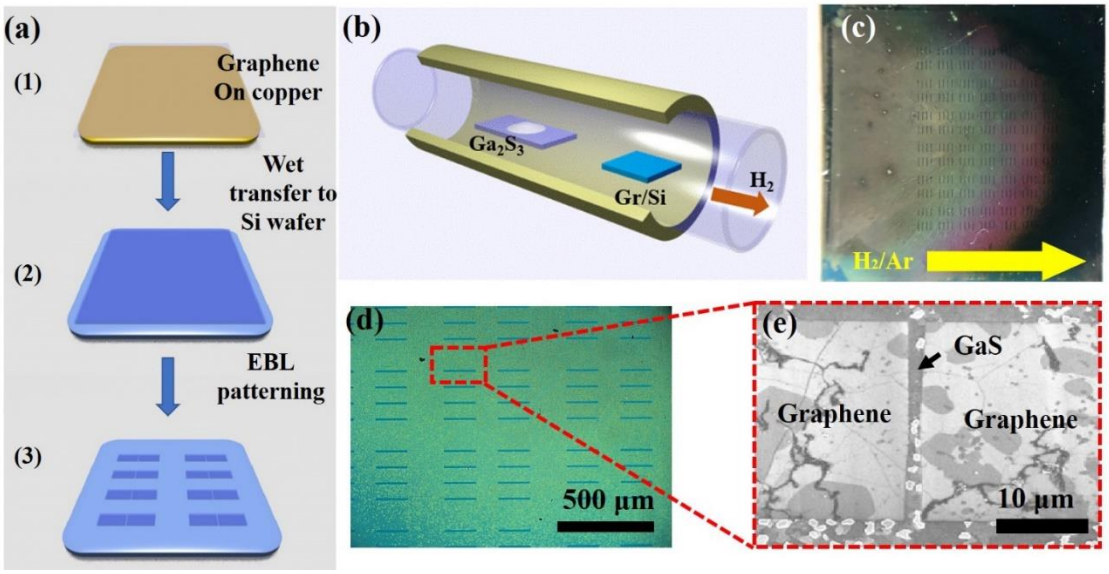

Figure 6.1. CVD growth of Gr/GaS/Gr heterostructure. (a) Schematic illustration of the process to make graphene electrode pairs on Si wafer; (b) Schematic illustration of CVD setup used to synthesize the Gr/GaS/Gr lateral heterostructure; (c) Photograph of as synthesized Gr/GaS/Gr heterostructure. The green area on the left are covered by GaS film and the dashed lines in the GaS area are pre-patterned graphene electrodes; (d) Optic image of Gr/GaS/Gr heterostructure arrays; (e) Magnified SEM image of selected area in (d), showing the interface of Gr/GaS/Gr.

In order to mass produce the Gr/GaS/Gr heterostructure, the first step is to prepare arrays of graphene electrode pairs. **Figure 6.1(a)** shows the standard procedure to pattern graphene electrode pairs. I started with CVD growth of continuous graphene film on copper substrate, followed by It transferring it on SiO_2 (300 nm)/p++ chip, as previously reported.[231] The patterning was performed using electron beam lithography

(EBL) with a negative resist (MaN – 2403). The width of graphene ribbons was 20 μm, with a 2 μm gap. The SEM image of as patterned graphene electrode pair arrays is illustrated in **Appendix, Figure 3**.

A single zone system with a 1-inch diameter quartz tube inside was used to selectively deposit GaS in the graphene gaps. **Figure 6.1(b)** is the schematics of the CVD setup used in this work. Ga_2S_3 powder was placed at the hot zone of the furnace. The SiO_2/Si substrate with pre-patterned graphene ribbon pairs was positioned at the downstream of the growth furnace, 8.5 cm away from the Ga_2S_3 precursor. The whole reaction was carried under ambient pressure.

The CVD growth of GaS was composed of three stages. [167] The whole system was first flushed with 500 sccm argon (Ar) gas for at least 30 min. Afterwards, the carrier gas was changed to 70 sccm mixture gas of 25% H_2/ 75% Ar. At the same time, the Ga_2S_3 precursor was heated to 800 °C at a ramping rate of 50 °C/ min. The reaction was initiated upon reaching the target temperature. By holding the Ga_2S_3 precursor in H_2-rich atmosphere at 800 °C for 25 min, I could ensure the deposition of layered GaS on substrate with a high coverage ratio. After the reaction finished, the carrier gas was changed to 150 sccm Ar for fast cooling process to room temperature.

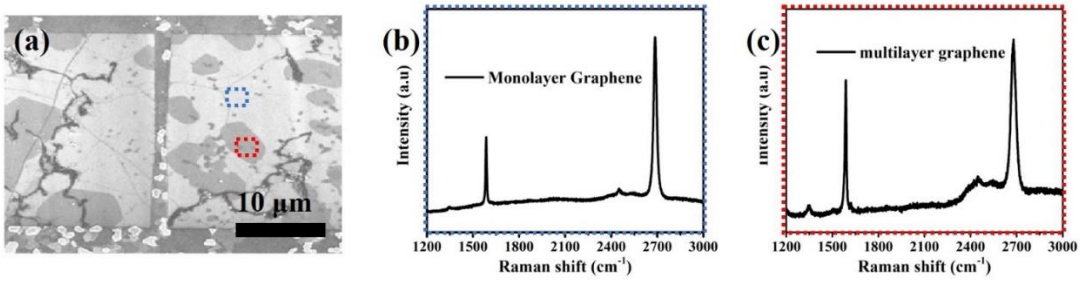

Figure 6.2. Raman spectra of graphene of Gr/GaS/Gr heterostructures (a) SEM image of a Gr/GaS/Gr photodetectors made by CVD growth on pre-patterned graphene gap; (b) Raman spectrum of graphene in highlighted area (blue); (c) Raman spectrum of graphene in highlighted area (red).

Figure 6.1(c) shows the photograph of as synthesized Gr/GaS/Gr heterostructure arrays. The green region in **Figure 6.1(c)** is covered by GaS continuous film while the dark region is covered by GaS domains. **Figure 6.1(d)** is the magnified image of GaS film region. The rectangular stripes are pre-patterned graphene ribbon pairs. The green GaS film covered the area between graphene ribbons. More than 200 devices could be fabricated by one CVD process. **Figure 6.1(e)** is the SEM image of the gap region sandwiched by graphene ribbons. The brighter grey blocks in the image are graphene electrode pairs and darker grey polygons on the ribbon are multilayer graphene, proven by the Raman measurement shown in **Figure 6.2**. The GaS film, appeared to be black, completely fill the gap between the graphene ribbon pairs, naturally forming the lateral Gr/GaS/Gr heterostructures. This makes it possible to use graphene as electrodes by simply applying a bias on them, without any post-processing.

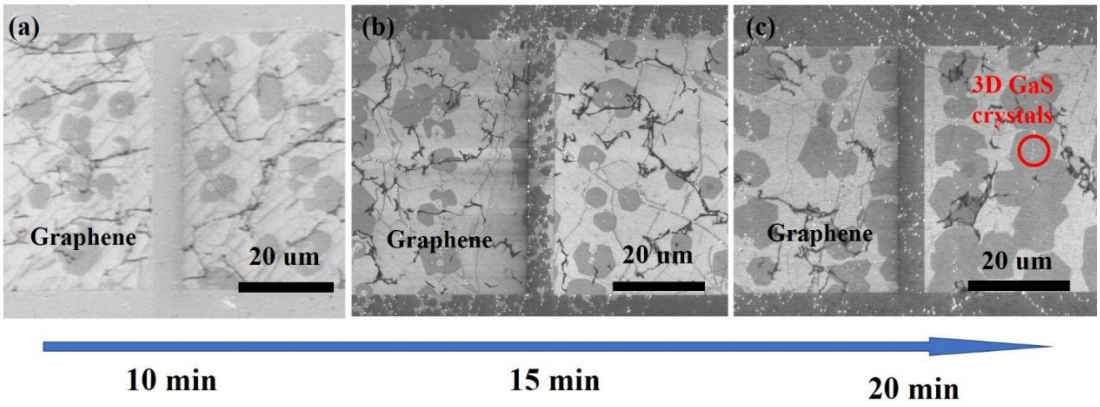

Figure 6.3. CVD growth of GaS as a function of growth time. (a-c) SEM images of CVD grown GaS on Gr/SiO_2 substrate as a function of growth time of (a) 10 min, (b) 15min and (c) 20 min. The darker grey polygons on the surface of graphene are multilayer graphene regions. The black polygons/film on the SiO_2 region are CVD grown GaS. The white points in the images are small 3D GaS crystals.

It should also be noticed that GaS preferentially grows on SiO_2/Si surface compared to the graphene. To understand this phenomenon, I altered the CVD growth time to investigate the growth mechanism of GaS. **Figure 6.3(a-c)** show the SEM image of as grown GaS topography with different growth time. Initially, GaS nucleus formed on the surface of SiO_2, shown as the tiny black spots in the embedded magnified SEM image. As grow time increase, the nucleus grew bigger and formed GaS domains (**Figure 6.3(b)**). By further increasing the growth time, the GaS film filled the gap of graphene film and 3D GaS crystals started to form on the surface of GaS film, shown as the white spots in **Figure 6.3(c)**. During the whole growth process, the nucleation of GaS on graphene surface is very limited. I could only spot some small GaS 3D clusters on the surface of multi-layer graphene domains and at the edge of the curling polymer residues

shown as black lines on graphene in the SEM image. I also noticed that a few GaS domains could be found on the surface of graphene, as the dark triangular shape shown in the SEM image in **Figure 6.4(a).** The Raman measurement (**Figure 6.4(b)**) proved that the dark triangular shapes were GaS grown on graphene.

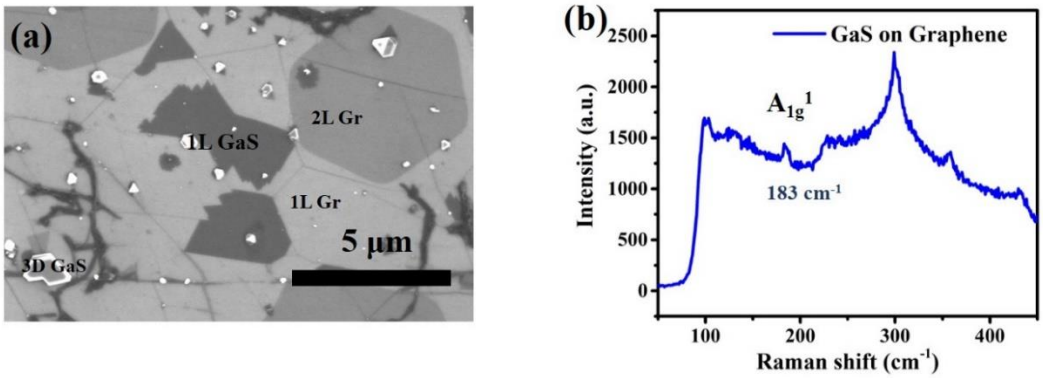

Figure 6.4. CVD growth of GaS on graphene substrate. (a) SEM image of CVD grown GaS on graphene substrate. (b) Raman spectrum of GaS grown on graphene.

However, this kind of deposition happens very occasionally in a small region and highly unlikely to reproduce using the same parameters. Judging by the sequence of GaS growth, I speculate that the selective growth behavior of GaS is determined by nucleation process. As the whole CVD process was carried out in high temperature environment with high H_2 concentration, SiO_2 could be easily modified. [297-299] The generation of defects provides abundant nucleation site for heterogeneous nucleation of GaS nucleus. On the other hand, the graphene is relatively more stable in high concentration H_2 environment. [300-301] Comparing with the surface of SiO_2, there were far fewer defects on the surface of graphene. The difference in the amount of nucleation site resulted in the preference of growth of GaS on SiO_2 surface.

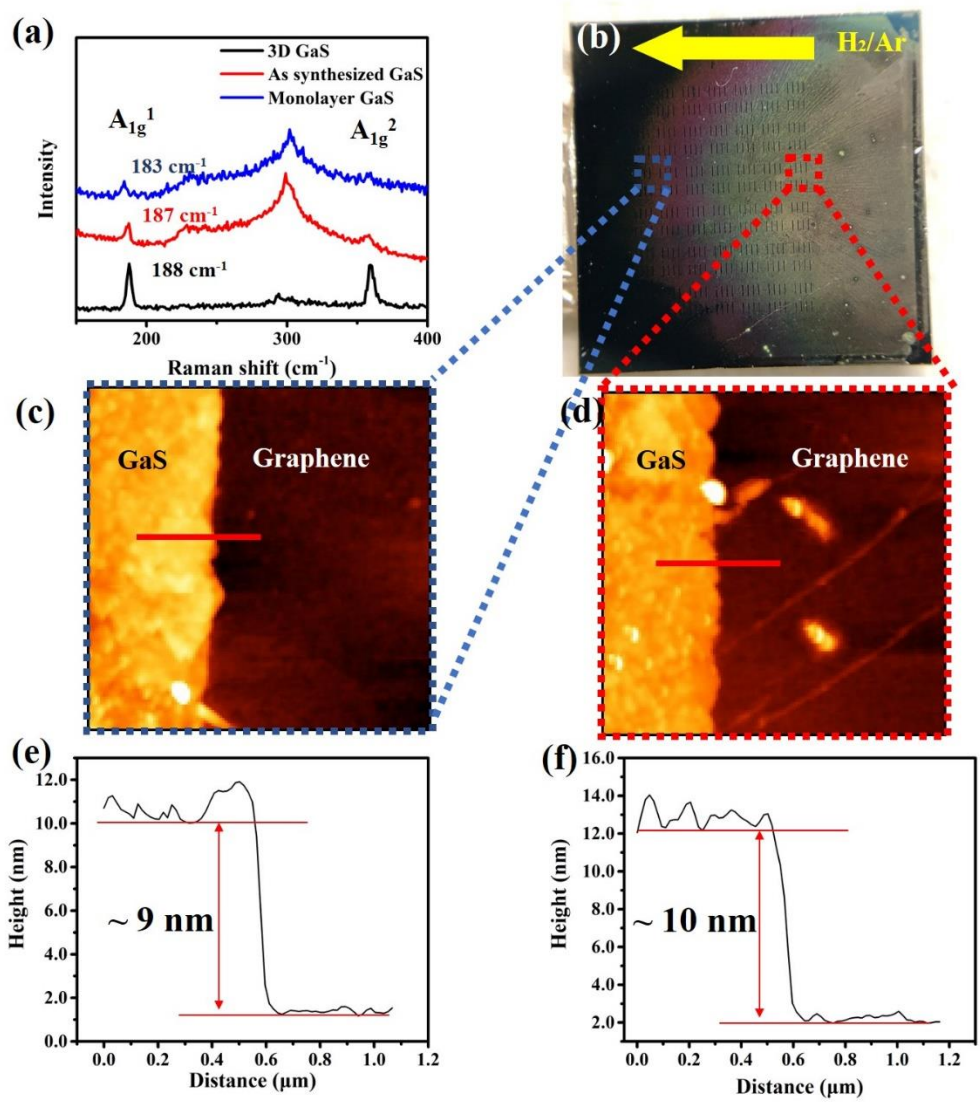

Figure 6.5. Raman spectroscopy and AFM characterization on as synthesized GaS film. (a) Raman spectra of monolayer GaS (blue curve), as synthesized GaS film (red curve) and 3D GaS crystal (black curve); (b) Photograph of as synthesized Gr/GaS/Gr lateral heterostructure arrays; (c-d) AFM height mapping of Gr/GaS interface, corresponding to the highlighted areas in (b); (e-f) Height profile of highlighted lines in (c) and (d), respectively.

The electronic property of GaS is closely related to the layer number and purity of as synthesized GaS. I conducted several characterization methods to investigate the quality of as synthesized GaS. Raman spectroscopy is a commonly used technique to determine the quality and thickness of GaS. According to previous studies, there are three first-order phonon modes in Raman spectra of layered GaS under 532 nm excitation: two out-of-plane mode known as A_{1g}^1 and A_{1g}^2, and one in-plane mode known as E_{2g}^1. [164, 302] For GaS grown on SiO_2, E_{2g}^1 is almost undetectable as the peak locates at around 300 cm^{-1} owing to strong background of SiO_2/Si substrate at ~303 cm^{-1}. On the other hand, A_{1g}^1 and A_{1g}^2 peak can be easily distinguished from background and evolves with the layer number of GaS film, which could help to determine the film thickness. For monolayer GaS, the A_{1g}^1, A_{1g}^2 peaks are very weak and locate at 182 cm^{-1}, 360 cm^{-1} respectively, shown as blue curve in **Figure 6.5(a)**. However, for bulk GaS crystals, the A_{1g}^1 and A_{1g}^2 are very strong and locate at 188 cm^{-1} and 360 cm^{-1} respectively, shown as the black curve in **Figure 6.5(a)**. I also presented the Raman spectrum of as synthesized GaS film in **Figure 6.5(a)** (red curve). It should be noticed that the position of A_{1g}^1 locates at about 187 cm^{-1}, between that of monolayer and 3D GaS. The intensity of A_{1g}^1 and A_{1g}^2 peaks also lays in between that of monolayer and 3D GaS. This suggested that the as synthesized GaS film was about a few layers' thick. It should also be noticed that Ga_2S_3 has a Raman peak at about 240 cm^{-1}, which was not observed in the Raman spectrum. This proves the purity of the GaS film.

AFM was used to deduce the layer number of the synthesized GaS material. According to previous researches, the thickness of wet transferred monolayer graphene is around

1nm. I could use the height of graphene as reference to determine the thickness of GaS. **Figure 6.5(c-d)** are the AFM height mapping profile of the Gr/GaS/Gr interface at downstream and upper stream area in **Figure 6.5(b)**. Judging by the height difference between the graphene and GaS in **Figure 6.5(e)**, I could estimate the thickness of GaS to be around 9+1=10 nm at the downstream area. Since the thickness monolayer GaS is about 1 nm, I could estimate that the layer number of GaS is around 10 layers. [167] I also applied the height line profile measurement of Gr/GaS/Gr heterostructures on the upper stream region. The thickness of GaS is around 10+1=11 nm, shown as **Figure 6.5(f)**. This proves that the as grown GaS film has good uniformity across the film region.

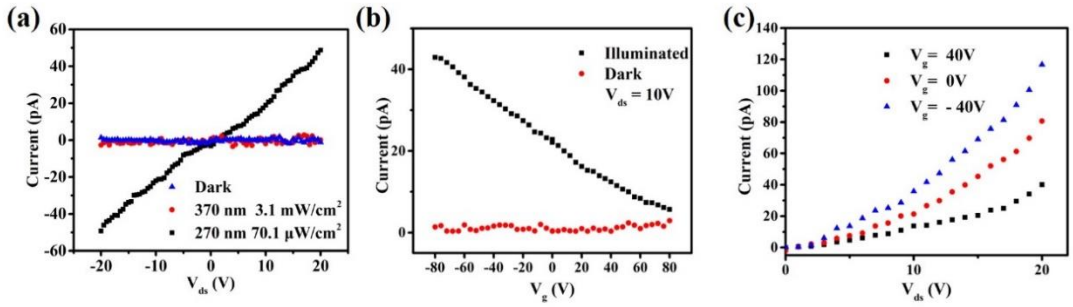

Figure 6.6. Electrical properties of as fabricated Gr/GaS/Gr heterostructures. (a) I-V characterization of as fabricated device under 270 nm UV light excitation, 370 nm blue light excitation and dark condition. (b) I-Vg characterization of the device under 270 nm excitation and dark condition. (c) I-V characterization of the devices under 270 nm excitation with various gate voltage.

I characterized the electronic response of fabricated Gr/GaS/Gr lateral heterostructures under different light excitation. A source-drain bias was applied by directly contacting

the tungsten probe tips to graphene ribbons. Two different light sources, 270 nm UV light and 370 nm blue light, were directly irradiated on to the sample, **Figure 6.6(a)**. When no light is illuminated on the device, no current could be detected within range of -20 V to 20 V. This indicates a large Schottky barrier between the graphene and semiconductor, shown as **Appendix. Figure 4**. However, when 270 nm light was irradiated on the device, I could observe a photocurrent signal that increases with applied bias while no photoresponse was seen for the 370nm excitation, even with the significantly higher power density. To enable photocurrent, the energy of light should be large enough to excite electrons across the band gap. [250, 303-304] **Figure 6.6(b-c)** show modulation of the photocurrent by applied back gate, under 10V source-drain bias.

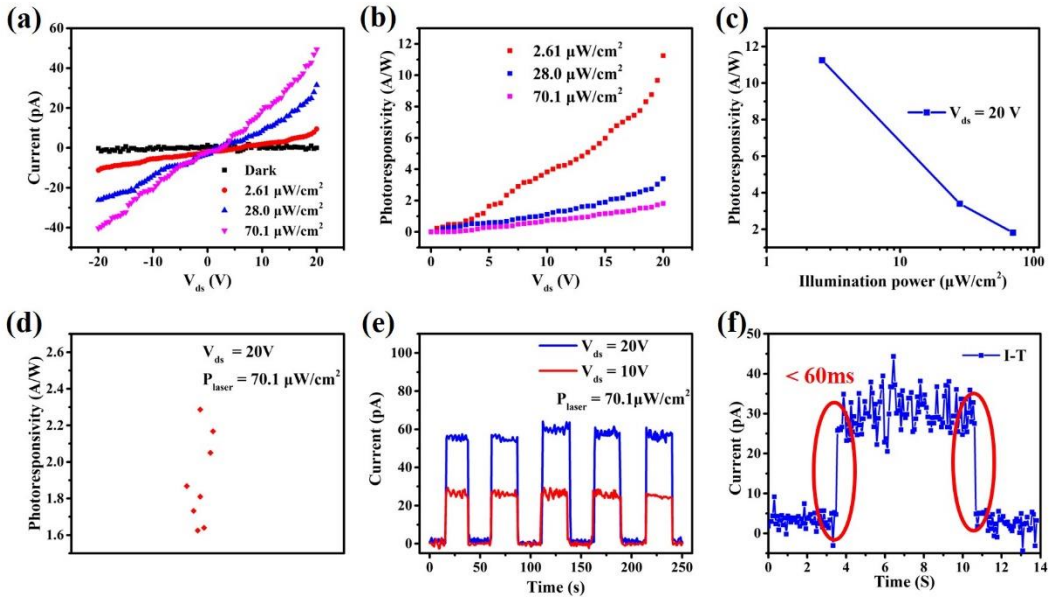

Figure 6.7. Photodetection properties of Gr/GaS/Gr devices. (a) I-V characterization as a function of illumination power; (b) Calculated photoresponsivity according to the I-V curve; (c) Photoresponsivity as a function of excitation power; (d) Statistics of the photoresponsivity of eight working devices; (e) Transient photocurrent characteristics of our device with 10 V and 20 V bias under 70.1 μW/cm^2 270 nm incident excitation; (f) Current vs. time plot of one typical on-off switching for response time measurement.

Figure 6.7(a) shows the I-V plot of as fabricated device under 270 nm incident light with various excitation power. I observed that by increasing the illumination power, the current also increased. As the dark current of the GaS device was basically at the same level with the noise of the measurement unit, which was about 10^{-13} A, the ON current was at the level of 10 pA, which is two magnitudes of order larger than the dark current, could be clearly distinguished from noise signal. The detection limit of the device could reach to as low as 2.61 μW/cm^2 with 10 pA photo-induced current at 20 V bias voltage.

Photoresponsivity(R) is a widely used figure of merits to describe how good photodetectors interact with light excitation via measurement of device's electrical response under light illumination. Photoresponsivity can be defined as the ratio of photoinduced current (I_{photo}) and intensity of excitation(P_{laser}), described as $\mathbf{R} = \frac{\boldsymbol{I_{photo}}}{\boldsymbol{P_{laser}}}$.[251] In **Figure 6.7(b)**, I presented the calculated photoresponsivity from the I-V curve shown in **Figure 6.7(a)**. It can be observed that photoresponsivity increased as bias voltage increased. The maximum R I got is 11.7 A/W at 20 V bias under 2.61 μW/cm^2 power density. **Figure 6.7(c)** is the plot of photoresponsivity versus the power of incident light. R presented a decreasing trend with enhanced incident power, which is typical for most photodetectors that operate of exciton-separation and extracting the respective electrons and holes at each electrode. As the excitation power increases, more photo-induced electron-hole pairs are generated, and their interactions cause a loss of energy and efficiency of charge extraction.

I also conducted statistical measurements on eight devices in one of the arrays, as illustrated in **Figure 6.7(d)**. Without any gate voltage, the R was 11.7 A/W under 2.61 μW/cm^2 illumination at +20 V bias. This proves good uniformity of as fabricated devices. Additionally, the time-resolved photocurrent plot of one of the devices under 270 nm excitation presented reproducible high and low impedance states under repeated cycles of on-off switching, as illustrated in **Figure 6.7(e)**. The ON-state current remains the same level even after 4 min, suggesting excellent stability and reproducible performance over long period of time. By increasing the data acquisition frequency, I could also estimate the response time of the device. **Figure 6.7(f)** shows one On-Off

cycle of the device. The transition from off-state current to on-state current happened within one data point, which suggested that the response time is less than 60 ms. The result is comparable to conventional photodetectors, making the device promising in fast photoswitching applications.

The relation between photoresponsivity (R) and photogain (G) could be expressed as following equation:

$$R = \eta_{ext} Ge/hv$$

where η_{ext} refers to the external quantum efficiency (EQE), e refers to the elementary charge unit, and v refers to the frequency of light source. [281] I could then calculate the photogain of the device using this equation, showing an external photogain up to 53.7 under P_{light} = 2.61 μW/cm^2 at +20 V bias. This indicates that Schottky barrier modulation is occurring and that some thermionic emission is also changing during photoirradiation. This also suggests that the photocurrent is likely coming from two effects, photoinduced exciton separation and charge extraction, and Schottky barrier lowering by photoexcited charge traps

6.3 Conclusion

In summary, compared to most of the widely studied 2D materials, layered GaS has a unique band structure with a wide indirect band gap of ~3 eV. This makes it a promising candidate material for UV detection and UV LED applications. Recently, researchers reported successful synthesis of 2D GaS. However, it has been challenging to fabricate

GaS based devices due to difficulties in post processing. In this work, I achieved the selective deposition of ultrathin GaS in pre-patterned graphene gaps via a one-step hydrogen reduction CVD process. The preferred growth of GaS on Si wafer makes it possible to easily mass-produce the Gr/GaS/Gr lateral photodetectors on Si wafer. Thanks to the wide band gap of GaS, the as fabricated photodetectors exhibited photodetection behavior to UV light only with a detection limit as low as 2.61 μW/cm2. The photoresponsivity (~11.7 A/W) and response time (<60ms) are comparable to other high quality 2D photodetectors made by 2D materials. Due to its unique physical properties, I anticipate that GaS could be an important building block in construction of next generation 2D opto-electronics.

1.

Chapter 7

Conclusion and Future Outlook

7.1 Thesis Summary

The research in this doctoral thesis has been divided into three sections, each referring to one chapter in this thesis. Chapter 4 investigated the method to directly synthesize the centimeter scale MoS_2/Graphene vertical heterostructure using chemical vapor deposition (CVD) technique. Chapter 5 focused on the selective direct CVD synthesis of WS_2 in the gap of prepatterned graphene ribbons, enabling large scale fabrication of graphene/WS_2/graphene lateral heterojunctions. Chapter 6 detailed the CVD synthesis of GaS, a wide band gap two-dimensional (2D) semiconductor, in the gap of prepatterned graphene ribbons, directly constructing the graphene/GaS/graphene lateral heterojunction for UV detection applications.

7.2 Conclusion

Thanks to the exceptional physical and electronic properties, 2D materials have been considered promising candidates in next generation electronics, optoelectronics and flexible devices. Graphene, the most widely studied 2D material, is an excellent conductor. Transition metal dichalcogenides (TMDs), such as tungsten disulfide (WS_2) and molybdenum disulfide (MoS_2), and metal monochalcogenides, such as gallium sulfide (GaS) and gallium selenide (GaSe), are semiconductors with wide range of band gaps. By combining these 2D materials in the form of heterostructures, it is possible to construct ultrathin nanodevices suitable for various applications. However, due to the

limitation of current state of art, it is challenging to produce 2D heterojunction in a large scale.

CVD is regarded as one of the most reliable and reproducible techniques for large area production of high quality 2D materials. It is also a promising method to construct the 2D heterostructure via direct deposition of one 2D materials onto other 2D materials as growth template. Using continuous graphene film on 300 nm SiO_2/Si wafer as substrate, MoS_2 could be directly deposited onto the graphene surface via hydrogen (H_2) to control both the chemistry of graphene and MoS_2. Centimeter scale MoS_2/graphene vertical heterojunction could be efficiently fabricated, whose quality and uniformity can be confirmed by Raman and photoluminescence (PL) spectroscopy. (Chapter 4) The optoelectronic properties of as synthesized heterostructure was characterized by photoresponse measurement via applying source-drain bias onto deposited metal bond pads. The high photo induced current and photoresponsivity proves the potential for scalable fabrication of high-quality photodetectors based on CVD grown 2D vertical heterostructures.

Besides the vertical heterostructures, CVD also holds promise in direct scalable assembly of lateral heterostructures. Through the careful control of growth conditions, WS_2 could selectively deposited in the gap of prepatterned graphene electrode pairs, naturally form the graphene/WS_2/graphene heterojunctions that can be regarded as a phototransistor. (Chapter 5) The as fabricated exhibited better performance than similar devices constructed by transfer method, owing to a better contact between graphene and WS_2 that lowering the Schottky barrier height.

Similarly, GaS, a novel 2D materials that have been successful synthesized recently, can also selectively deposited in the gap of graphene electrode pairs via control of nucleation of GaS domains. (Chapter 6) The wide band gap nature of GaS opens a new area for 2D materials in the application of ultra-violet (UV) light detection. By directly applying bias on the graphene electrodes, the graphene/GaS/graphene heterojunction shew photoresponsivity for UV light only. The outstanding response time, on-off ratio and photoresponsivity exhibits great potential for commercialized scalable production of 2D UV photodetectors.

7.3 Future Outlook

In this thesis, the CVD experiments were conducted under ambient pressure. Due to the nature of ambient pressure chemical vapor deposition (APCVD), the deposition of 2D materials is closely related to the mass transportation in the CVD systems, which is challenging to achieve high uniformity in wafer scale. To facilitate the future industrialization of 2D heterostructures, further work will involve using low pressure chemical vapor deposition (LPCVD) to achieve scalable production of 2D heterojunctions over a large area. In addition, the graphene growth templates used in this thesis were fabricated via a standard procedure: growth, transfer and patterning. This procedure is time consuming and inevitably introduces impurities onto graphene surface that influences the contact between graphene and other 2D materials. A more desirable process is to develop multi-step CVD process that can deposit 2D materials on the same substrate by sequence. This involves a deepened understanding of materials'

chemistry in the CVD process and the development of new techniques that can tune the surface of growth substrates.

Appendix

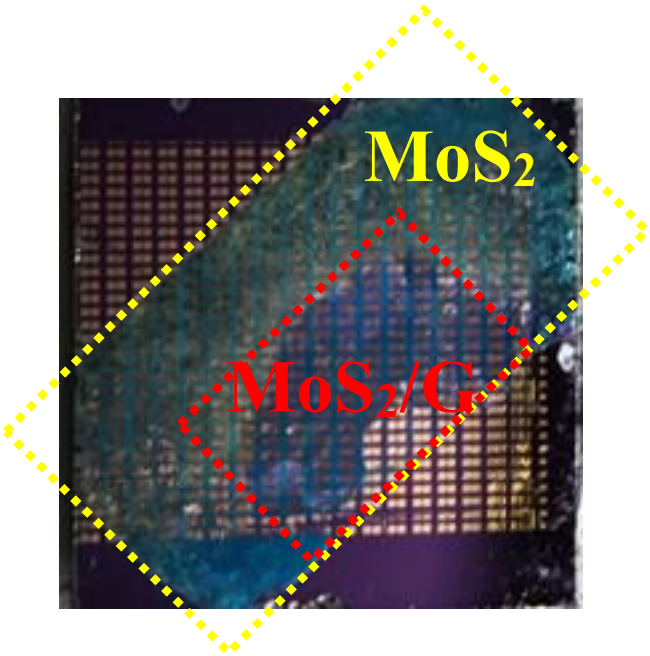

Figure 1. Optical image of as fabricated device chip. The device chip was fabricated by transferring as grown MoS_2/G film (region within yellow dashed line) onto Si wafer prepatterned with gold bond pads. The region within red dashed line was covered by MoS_2/G film while the rest was covered by 2D MoS_2 domains and 3D MoS_2 crystals.

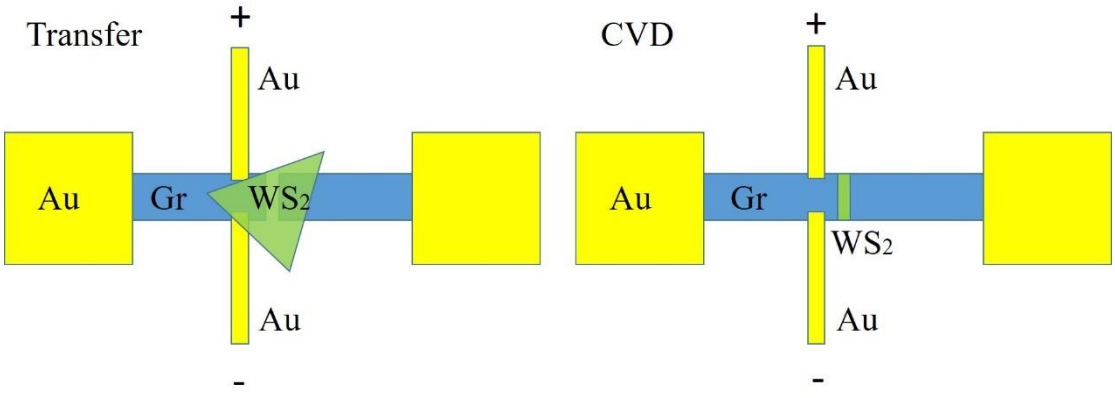

Figure 2. Schematic illustrations of setup used to measure the Dirac point of graphene after transfer of WS_2 and CVD growth of WS_2.

Section 1. Extraction of Schottky barrier using back-to-back diode model

A modified thermionic emission equation was introduced for Schottky barrier extraction from I-V curves. Given the semi-metal and semiconductor properties of graphene and WS_2, the device can be simplified into a back-to-back Schottky diode pair in series. The current of the device could be expressed as following set of equations:

$$\mathrm{I} = I_0 \times \exp\left[-\left(1-\frac{1}{n}\right) e\beta \mathrm{V} V_1\right] \times [\exp(e\beta V_1) - 1] \quad (1)$$

$$\mathrm{I} = \frac{V_2}{R} \quad (2)$$

$$\mathrm{I} = -I_0 \times \exp\left[-\left(1-\frac{1}{n}\right) e\beta \mathrm{V} V_3\right] \times [\exp(e\beta V_3) - 1] \quad (3)$$

$$\mathrm{U} = V_1 + V_2 + V_3 \quad (4)$$

By solving equation (1)-(4), we can obtain:

$$\mathrm{I} = I_0 [\frac{\cosh(\frac{1}{2}(1-\frac{1}{n})e\beta(\mathrm{U-IR}))}{\cosh(\frac{1}{2n}e\beta(\mathrm{U-IR}))}]^{-(1-\frac{1}{n})} \times \frac{\sinh(\frac{1}{2}e\beta(\mathrm{U-IR}))}{\cosh(\frac{1}{2n}e\beta(\mathrm{U-IR}))} \quad (5)$$

Where I is the source-drain current, U is the source-drain bias, n is the ideality factor, e is the elementary charge unit and $\beta = 1/k_B T$ is the Boltzmann factor, V_i (i =1, 2, 3) are the voltage drop across the left diode, middle resistance, and right diode. I_0 is a constant related to the Schottky barrier height which could be expressed as

$$I_0 = \mathrm{w} A_{2d} T^{\frac{3}{2}} \times \exp(-\beta e \Phi_{SB}) \quad (6)$$

Where w is the contact width of graphene and A_{2d} is the two-dimensional equivalent of Richardson constant, T is the temperature, and Φ_{SB} is the effective Schottky barrier height.

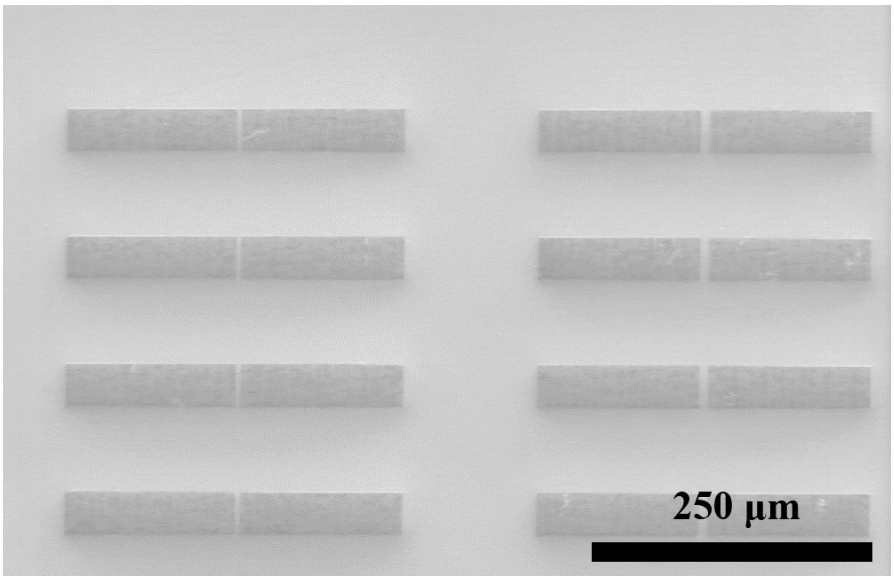

Figure 3. SEM image of as patterned graphene electrode pair array

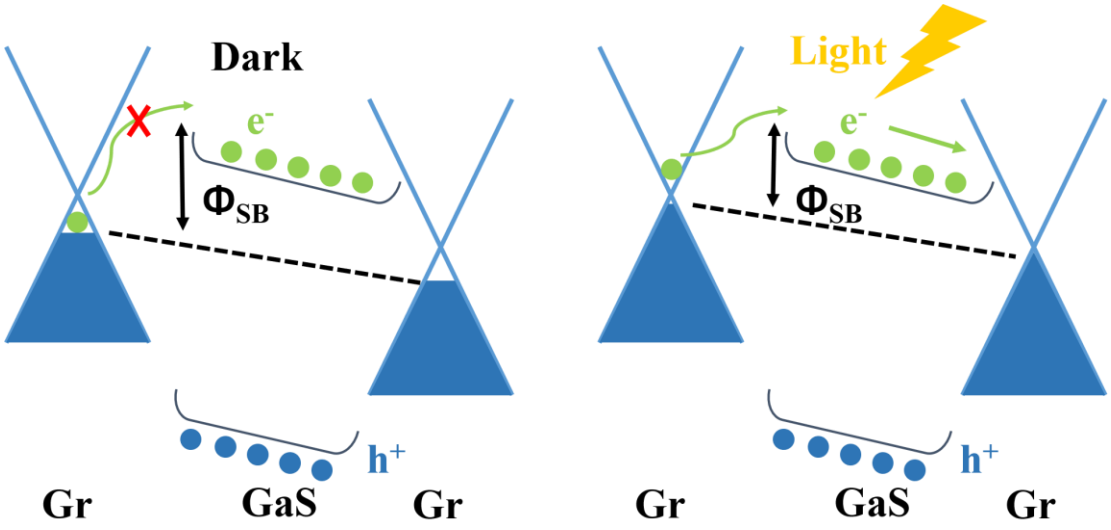

Figure 4. Band diagram of graphene:GaS:graphene heterojunction under dark and illumination

Reference:

1. Geim, A.; Novoselov, K. The Rise Of Graphene. *Nature Materials* **2007**, *6*, 183-191.
2. Wallace, P. The Band Theory Of Graphite. *Physical Review* **1947**, *71*, 622-634.
3. Semenoff, G. Condensed-Matter Simulation Of A Three-Dimensional Anomaly. *Physical Review Letters* **1984**, *53*, 2449-2452.
4. Haldane, F. Model For A Quantum Hall Effect Without Landau Levels: Condensed-Matter Realization Of The "Parity Anomaly." *Physical Review Letters* **1988**, *61*, 2015-2018.
5. Brodie, B. XXIII.—Researches On The Atomic Weight Of Graphite. *Q. J. Chem. Soc.* **1860**, *12*, 261-268.
6. Novoselov, K. Electric Field Effect In Atomically Thin Carbon Films. *Science* **2004**, *306*, 666-669.
7. Novoselov, K.; McCann, E.; Morozov, S.; Fal'ko, V.; Katsnelson, M.; Zeitler, U.; Jiang, D.; Schedin, F.; Geim, A. Unconventional Quantum Hall Effect And Berry'S Phase Of 2Π In Bilayer Graphene. *Nature Physics* **2006**, *2*, 177-180.
8. Zhang, Y.; Tan, Y.; Stormer, H.; Kim, P. Experimental Observation Of The Quantum Hall Effect And Berry's Phase In Graphene. *Nature* **2005**, *438*, 201-204.
9. Jiang, Z.; Zhang, Y.; Stormer, H.; Kim, P. Quantum Hall States Near The Charge-Neutral Dirac Point In Graphene. *Physical Review Letters* **2007**, *99*.
10. Bolotin, K.; Sikes, K.; Jiang, Z.; Klima, M.; Fudenberg, G.; Hone, J.; Kim, P.; Stormer, H. Ultrahigh Electron Mobility In Suspended Graphene. *Solid State*

Communications **2008**, *146*, 351-355.

11. Novoselov, K.; Geim, A.; Morozov, S.; Jiang, D.; Katsnelson, M.; Grigorieva, I.; Dubonos, S.; Firsov, A. Two-Dimensional Gas Of Massless Dirac Fermions In Graphene. *Nature* **2005**, *438*, 197-200.
12. Morozov, S.; Novoselov, K.; Katsnelson, M.; Schedin, F.; Elias, D.; Jaszczak, J.; Geim, A. Giant Intrinsic Carrier Mobilities In Graphene And Its Bilayer. *Physical Review Letters* **2008**, *100*.
13. Han, M.; Ozyilmaz, B.; Zhang, Y.; Jarillo-Herero, P.; Kim, P. Electronic Transport Measurements In Graphene Nanoribbons. *physica status solidi (b)* **2007**, *244*, 4134-4137.
14. Schedin, F.; Geim, A.; Morozov, S.; Hill, E.; Blake, P.; Katsnelson, M.; Novoselov, K. Detection Of Individual Gas Molecules Adsorbed On Graphene. *Nature Materials* **2007**, *6*, 652-655.
15. Kuan, A.; Lu, B.; Golovchenko, J. Electrical Pulse Fabricated Graphene Nanopores For Single Molecule Sensing. *Biophysical Journal* **2015**, *108*, 175a.
16. Sreenivasulu, B.; Ramji, B.; Nagaral, M. A Review On Graphene Reinforced Polymer Matrix Composites. *Materials Today: Proceedings* **2018**, *5*, 2419-2428.
17. Kirkland, N.; Schiller, T.; Medhekar, N.; Birbilis, N. Exploring Graphene As A Corrosion Protection Barrier. *Corrosion Science* **2012**, *56*, 1-4.
18. Prasai, D.; Tuberquia, J.; Harl, R.; Jennings, G.; Bolotin, K. Graphene: Corrosion-Inhibiting Coating. *ACS Nano* **2012**, *6*, 1102-1108.
19. Kim, K.; Zhao, Y.; Jang, H.; Lee, S.; Kim, J.; Kim, K.; Ahn, J.; Kim, P.; Choi, J.;

Hong, B. Large-Scale Pattern Growth Of Graphene Films For Stretchable Transparent Electrodes. *Nature* **2009**, *457*, 706-710.

20. Eda, G.; Fanchini, G.; Chhowalla, M. Large-Area Ultrathin Films Of Reduced Graphene Oxide As A Transparent And Flexible Electronic Material. *Nature Nanotechnology* **2008**, *3*, 270-274.
21. Chitara, B.; Panchakarla, L.; Krupanidhi, S.; Rao, C. Infrared Photodetectors Based On Reduced Graphene Oxide And Graphene Nanoribbons. *Advanced Materials* **2011**, *23*, 5419-5424.
22. Acik, M.; Lee, G.; Mattevi, C.; Chhowalla, M.; Cho, K.; Chabal, Y. Unusual Infrared-Absorption Mechanism In Thermally Reduced Graphene Oxide. *Nature Materials* **2010**, *9*, 840-845.
23. Yin, Z.; Zhu, J.; He, Q.; Cao, X.; Tan, C.; Chen, H.; Yan, Q.; Zhang, H. Graphene-Based Materials For Solar Cell Applications. *Advanced Energy Materials* **2013**, *4*, 1300574.
24. Casaluci, S.; Gemmi, M.; Pellegrini, V.; Di Carlo, A.; Bonaccorso, F. Graphene-Based Large Area Dye-Sensitized Solar Cell Modules. *Nanoscale* **2016**, *8*, 5368-5378.
25. Lin, Y.; Valdes-Garcia, A.; Han, S.; Farmer, D.; Meric, I.; Sun, Y.; Wu, Y.; Dimitrakopoulos, C.; Grill, A.; Avouris, P. et al. Wafer-Scale Graphene Integrated Circuit. *Science* **2011**, *332*, 1294-1297.
26. Huang, Y.; Dong, X.; Shi, Y.; Li, C.; Li, L.; Chen, P. Nanoelectronic Biosensors Based On CVD Grown Graphene. *Nanoscale* 2010, *2*, 1485.

27. Gurunathan, S.; Kim, J. Synthesis, Toxicity, Biocompatibility, And Biomedical Applications Of Graphene And Graphene-Related Materials. *International Journal of Nanomedicine* **2016**, 1927.
28. Zhao, Q.; Nardelli, M.; Bernholc, J. Ultimate Strength Of Carbon Nanotubes: A Theoretical Study. *Physical Review B* **2002**, *65*.
29. Lee, C.; Wei, X.; Kysar, J.; Hone, J. Measurement Of The Elastic Properties And Intrinsic Strength Of Monolayer Graphene. *Science* **2008**, *321*, 385-388.
30. Khare, R.; Mielke, S.; Paci, J.; Zhang, S.; Ballarini, R.; Schatz, G.; Belytschko, T. Coupled Quantum Mechanical/Molecular Mechanical Modeling Of The Fracture Of Defective Carbon Nanotubes And Graphene Sheets. *Physical Review B* **2007**, *75*.
31. Liu, F.; Ming, P.; Li, J. Ab Initiocalculation Of Ideal Strength And Phonon Instability Of Graphene Under Tension. *Physical Review B* **2007**, *76*.
32. Balandin, A.; Ghosh, S.; Bao, W.; Calizo, I.; Teweldebrhan, D.; Miao, F.; Lau, C. Superior Thermal Conductivity Of Single-Layer Graphene. *Nano Letters* **2008**, *8*, 902-907.
33. Saito, K.; Nakamura, J.; Natori, A. Ballistic Thermal Conductance Of A Graphene Sheet. *Physical Review B* **2007**, *76*.
34. Saito, K.; Nakamura, J.; Natori, A. Ballistic Thermal Conductance Of A Graphene Sheet. *Physical Review B* **2007**, *76*.
35. Ferrari, A.; Basko, D. Raman Spectroscopy As A Versatile Tool For Studying The Properties Of Graphene. *Nature Nanotechnology* **2013**, *8*, 235-246.
36. Ferrari, A.; Meyer, J.; Scardaci, V.; Casiraghi, C.; Lazzeri, M.; Mauri, F.; Piscanec,

S.; Jiang, D.; Novoselov, K.; Roth, S. et al. Raman Spectrum Of Graphene And Graphene Layers. *Physical Review Letters* **2006**, *97*.

37. Graf, D.; Molitor, F.; Ensslin, K.; Stampfer, C.; Jungen, A.; Hierold, C.; Wirtz, L. Raman Mapping Of A Single-Layer To Double-Layer Graphene Transition. *The European Physical Journal Special Topics* **2007**, *148*, 171-176.
38. Castro Neto, A.; Guinea, F.; Peres, N.; Novoselov, K.; Geim, A. The Electronic Properties Of Graphene. *Reviews of Modern Physics* **2009**, *81*, 109-162.
39. Chen, J.; Jang, C.; Xiao, S.; Ishigami, M.; Fuhrer, M. Intrinsic And Extrinsic Performance Limits Of Graphene Devices On SiO_2. *Nature Nanotechnology* **2008**, *3*, 206-209.
40. Dürkop, T.; Getty, S.; Cobas, E.; Fuhrer, M. Extraordinary Mobility In Semiconducting Carbon Nanotubes. *Nano Letters* **2004**, *4*, 35-39.
41. Cooper, D.; D'Anjou, B.; Ghattamaneni, N.; Harack, B.; Hilke, M.; Horth, A.; Majlis, N.; Massicotte, M.; Vandsburger, L.; Whiteway, E. et al. Experimental Review Of Graphene. *ISRN Condensed Matter Physics* **2012**, *2012*, 1-56.
42. Hrostowski, H.; Morin, F.; Geballe, T.; Wheatley, G. Hall Effect And Conductivity Of InSb. *Physical Review* **1955**, *100*, 1672-1676.
43. Bonaccorso, F.; Sun, Z.; Hasan, T.; Ferrari, A. Graphene Photonics And Optoelectronics. *Nature Photonics* **2010**, *4*, 611-622.
44. Chen, J.; Jang, C.; Adam, S.; Fuhrer, M.; Williams, E.; Ishigami, M. Charged-Impurity Scattering In Graphene. *Nature Physics* **2008**, *4*, 377-381.
45. Yan, J.; Fuhrer, M. Correlated Charged Impurity Scattering In Graphene. *Physical*

Review Letters **2011**, *107*.

46. Dean, C.; Young, A.; Meric, I.; Lee, C.; Wang, L.; Sorgenfrei, S.; Watanabe, K.; Taniguchi, T.; Kim, P.; Shepard, K. et al. Boron Nitride Substrates For High-Quality Graphene Electronics. *Nature Nanotechnology* **2010**, *5*, 722-726.
47. Gannett, W.; Regan, W.; Watanabe, K.; Taniguchi, T.; Crommie, M.; Zettl, A. Boron Nitride Substrates For High Mobility Chemical Vapor Deposited Graphene. *Applied Physics Letters* **2011**, *98*, 242105.
48. Kuzmenko, A.; van Heumen, E.; Carbone, F.; van der Marel, D. Universal Optical Conductance Of Graphite. *Physical Review Letters* **2008**, *100*.
49. Mazur, M.; Kaczmarek, D.; Domaradzki, J.; Wojcieszak, D.; Song, S.; Placido, F. Influence Of Thickness On Transparency And Sheet Resistance Of ITO Thin Films. *The Eighth International Conference on Advanced Semiconductor Devices and Microsystems* **2010**.
50. Yi, M.; Shen, Z. A Review On Mechanical Exfoliation For The Scalable Production Of Graphene. *Journal of Materials Chemistry A* **2015**, *3*, 11700-11715.
51. Wang, S.; Zhang, Y.; Abidi, N.; Cabrales, L. Wettability And Surface Free Energy Of Graphene Films. *Langmuir* **2009**, *25*, 11078-11081.
52. Hernandez, Y.; Nicolosi, V.; Lotya, M.; Blighe, F.; Sun, Z.; De, S.; McGovern, I.; Holland, B.; Byrne, M.; Gun'Ko, Y. et al. High-Yield Production Of Graphene By Liquid-Phase Exfoliation Of Graphite. *Nature Nanotechnology* **2008**, *3*, 563-568.
53. Keeley, G.; O'Neill, A.; McEvoy, N.; Peltekis, N.; Coleman, J.; Duesberg, G. Electrochemical Ascorbic Acid Sensor Based On DMF-Exfoliated

Graphene. *Journal of Materials Chemistry* **2010**, *20*, 7864.

54. Hamilton, C.; Lomeda, J.; Sun, Z.; Tour, J.; Barron, A. High-Yield Organic Dispersions Of Unfunctionalized Graphene. *Nano Letters* **2009**, *9*, 3460-3462.
55. Hummers, W.; Offeman, R. Preparation Of Graphitic Oxide. *Journal of the American Chemical Society* **1958**, *80*, 1339-1339.
56. Stankovich, S.; Dikin, D.; Piner, R.; Kohlhaas, K.; Kleinhammes, A.; Jia, Y.; Wu, Y.; Nguyen, S.; Ruoff, R. Synthesis Of Graphene-Based Nanosheets Via Chemical Reduction Of Exfoliated Graphite Oxide. *Carbon* **2007**, *45*, 1558-1565.
57. Pei, S.; Zhao, J.; Du, J.; Ren, W.; Cheng, H. Direct Reduction Of Graphene Oxide Films Into Highly Conductive And Flexible Graphene Films By Hydrohalic Acids. *Carbon* **2010**, *48*, 4466-4474.
58. Shin, H.; Kim, K.; Benayad, A.; Yoon, S.; Park, H.; Jung, I.; Jin, M.; Jeong, H.; Kim, J.; Choi, J. et al. Efficient Reduction Of Graphite Oxide By Sodium Borohydride And Its Effect On Electrical Conductance. *Advanced Functional Materials* **2009**, *19*, 1987-1992.
59. Stankovich, S.; Dikin, D.; Dommett, G.; Kohlhaas, K.; Zimney, E.; Stach, E.; Piner, R.; Nguyen, S.; Ruoff, R. Graphene-Based Composite Materials. *Nature* **2006**, *442*, 282-286.
60. Berger, C.; Song, Z.; Li, T.; Li, X.; Ogbazghi, A.; Feng, R.; Dai, Z.; Marchenkov, A.; Conrad, E.; First, P. et al. Ultrathin Epitaxial Graphite: 2D Electron Gas Properties And A Route Toward Graphene-Based Nanoelectronics. *The Journal of Physical Chemistry B* **2004**, *108*, 19912-19916.

61. Berger, C. Electronic Confinement And Coherence In Patterned Epitaxial Graphene. *Science* **2006**, *312*, 1191-1196.

62. Emtsev, K.; Bostwick, A.; Horn, K.; Jobst, J.; Kellogg, G.; Ley, L.; McChesney, J.; Ohta, T.; Reshanov, S.; Röhrl, J. et al. Towards Wafer-Size Graphene Layers By Atmospheric Pressure Graphitization Of Silicon Carbide. *Nature Materials* **2009**, *8*, 203-207.

63. May, J. Platinum Surface LEED Rings. *Surface Science* **1969**, *17*, 267-270.

64. Wintterlin, J.; Bocquet, M. Graphene On Metal Surfaces. *Surface Science* **2009**, *603*, 1841-1852.

65. An, H.; Lee, W.; Jung, J. Graphene Synthesis On Fe Foil Using Thermal CVD. *Current Applied Physics* 2011, *11*, S81-S85.

66. Sutter, E.; Albrecht, P.; Sutter, P. Graphene Growth On Polycrystalline Ru Thin Films. *Applied Physics Letters* **2009**, *95*, 133109.

67. Wang, S.; Pei, Y.; Wang, X.; Wang, H.; Meng, Q.; Tian, H.; Zheng, X.; Zheng, W.; Liu, Y. Synthesis Of Graphene On A Polycrystalline Co Film By Radio-Frequency Plasma-Enhanced Chemical Vapour Deposition. *Journal of Physics D: Applied Physics* **2010**, *43*, 455402.

68. Gao, T.; Xie, S.; Gao, Y.; Liu, M.; Chen, Y.; Zhang, Y.; Liu, Z. Growth And Atomic-Scale Characterizations Of Graphene On Multifaceted Textured Pt Foils Prepared By Chemical Vapor Deposition. *ACS Nano* **2011**, *5*, 9194-9201.

69. Oznuluer, T.; Pince, E.; Polat, E.; Balci, O.; Salihoglu, O.; Kocabas, C. Synthesis Of Graphene On Gold. *Applied Physics Letters* **2011**, *98*, 183101.

70. Yu, Q.; Lian, J.; Siriponglert, S.; Li, H.; Chen, Y.; Pei, S. Graphene Segregated On Ni Surfaces And Transferred To Insulators. *Applied Physics Letters* **2008**, *93*, 113103.

71. Li, X.; Cai, W.; An, J.; Kim, S.; Nah, J.; Yang, D.; Piner, R.; Velamakanni, A.; Jung, I.; Tutuc, E. et al. Large-Area Synthesis Of High-Quality And Uniform Graphene Films On Copper Foils. *Science* **2009**, *324*, 1312-1314.

72. Bae, S.; Kim, H.; Lee, Y.; Xu, X.; Park, J.; Zheng, Y.; Balakrishnan, J.; Lei, T.; Ri Kim, H.; Song, Y. et al. Roll-To-Roll Production Of 30-Inch Graphene Films For Transparent Electrodes. *Nature Nanotechnology* **2010**, *5*, 574-578.

73. Huang, M.; Biswal, M.; Park, H.; Jin, S.; Qu, D.; Hong, S.; Zhu, Z.; Qiu, L.; Luo, D.; Liu, X. et al. Highly Oriented Monolayer Graphene Grown On A Cu/Ni(111) Alloy Foil. *ACS Nano* **2018**, *12*, 6117-6127.

74. Li, X.; Zhu, Y.; Cai, W.; Borysiak, M.; Han, B.; Chen, D.; Piner, R.; Colombo, L.; Ruoff, R. Transfer Of Large-Area Graphene Films For High-Performance Transparent Conductive Electrodes. *Nano Letters* **2009**, *9*, 4359-4363.

75. Li, X.; Colombo, L.; Ruoff, R. Synthesis Of Graphene Films On Copper Foils By Chemical Vapor Deposition. *Advanced Materials* **2016**, *28*, 6247-6252.

76. Wang, Y.; Zheng, Y.; Xu, X.; Dubuisson, E.; Bao, Q.; Lu, J.; Loh, K. Electrochemical Delamination Of CVD-Grown Graphene Film: Toward The Recyclable Use Of Copper Catalyst. *ACS Nano* **2011**, *5*, 9927-9933.

77. Lee, Y.; Bae, S.; Jang, H.; Jang, S.; Zhu, S.; Sim, S.; Song, Y.; Hong, B.; Ahn, J. Wafer-Scale Synthesis And Transfer Of Graphene Films. *Nano Letters* **2010**, *10*,

490-493.

78. Kim, S.; Choi, T.; Lee, B.; Lee, S.; Choi, K.; Park, J.; Yoo, J.; Choi, Y.; Ryu, J.; Kim, P. et al. Ultraclean Patterned Transfer Of Single-Layer Graphene By Recyclable Pressure Sensitive Adhesive Films. *Nano Letters* **2015**, *15*, 3236-3240.
79. Chhowalla, M.; Shin, H.; Eda, G.; Li, L.; Loh, K.; Zhang, H. The Chemistry Of Two-Dimensional Layered Transition Metal Dichalcogenide Nanosheets. *Nature Chemistry* **2013**, *5*, 263-275.
80. Jariwala, D.; Sangwan, V.; Lauhon, L.; Marks, T.; Hersam, M. Emerging Device Applications For Semiconducting Two-Dimensional Transition Metal Dichalcogenides. *ACS Nano* **2014**, *8*, 1102-1120.
81. Wang, Q.; Kalantar-Zadeh, K.; Kis, A.; Coleman, J.; Strano, M. Electronics And Optoelectronics Of Two-Dimensional Transition Metal Dichalcogenides. *Nature Nanotechnology* **2012**, *7*, 699-712.
82. Han, J.; Lee, S.; Yoo, D.; Lee, J.; Jeong, S.; Kim, J.; Cheon, J. Unveiling Chemical Reactivity And Structural Transformation Of Two-Dimensional Layered Nanocrystals. *Journal of the American Chemical Society* **2013**, *135*, 3736-3739.
83. Ganatra, R.; Zhang, Q. Few-Layer Mos2: A Promising Layered Semiconductor. *ACS Nano* **2014**, *8*, 4074-4099.
84. Wi, S.; Kim, H.; Chen, M.; Nam, H.; Guo, L.; Meyhofer, E.; Liang, X. Enhancement Of Photovoltaic Response In Multilayer Mos2 Induced By Plasma Doping. *ACS Nano* **2014**, *8*, 5270-5281.
85. Ding, S.; Zhang, D.; Chen, J.; Lou, X. Facile Synthesis Of Hierarchical

Mos2microspheres Composed Of Few-Layered Nanosheets And Their Lithium Storage Properties. *Nanoscale* **2012**, *4*, 95-98.

86. Li, Y.; Wang, H.; Xie, L.; Liang, Y.; Hong, G.; Dai, H. Mos2nanoparticles Grown On Graphene: An Advanced Catalyst For The Hydrogen Evolution Reaction. *Journal of the American Chemical Society* **2011**, *133*, 7296-7299.
87. Wu, W.; Wang, L.; Li, Y.; Zhang, F.; Lin, L.; Niu, S.; Chenet, D.; Zhang, X.; Hao, Y.; Heinz, T. et al. Piezoelectricity Of Single-Atomic-Layer MoS_2 For Energy Conversion And Piezotronics. *Nature* **2014**, *514*, 470-474.
88. Amani, M.; Chin, M.; Birdwell, A.; O'Regan, T.; Najmaei, S.; Liu, Z.; Ajayan, P.; Lou, J.; Dubey, M. Electrical Performance Of Monolayer MoS_2 Field-Effect Transistors Prepared By Chemical Vapor Deposition. *Applied Physics Letters* **2013**, *102*, 193107.
89. Shinde, S.; Kalita, G.; Tanemura, M. Fabrication Of Poly(Methyl Methacrylate)-MoS_2/Graphene Heterostructure For Memory Device Application. *Journal of Applied Physics* **2014**, *116*, 214306.
90. Lopez-Sanchez, O.; Lembke, D.; Kayci, M.; Radenovic, A.; Kis, A. Ultrasensitive Photodetectors Based On Monolayer MoS_2. *Nature Nanotechnology* **2013**, *8*, 497-501.
91. Gutiérrez, H.; Perea-López, N.; Elías, A.; Berkdemir, A.; Wang, B.; Lv, R.; López-Urías, F.; Crespi, V.; Terrones, H.; Terrones, M. Extraordinary Room-Temperature Photoluminescence In Triangular WS_2 Monolayers. *Nano Letters* **2012**, *13*, 3447-3454.

92. Liu, L.; Kumar, S.; Ouyang, Y.; Guo, J. Performance Limits Of Monolayer Transition Metal Dichalcogenide Transistors. *IEEE Transactions on Electron Devices* **2011**, *58*, 3042-3047.

93. Ye, Y.; Wong, Z.; Lu, X.; Ni, X.; Zhu, H.; Chen, X.; Wang, Y.; Zhang, X. Monolayer Excitonic Laser. *Nature Photonics* **2015**, *9*, 733-737.

94. Yang, W.; Shang, J.; Wang, J.; Shen, X.; Cao, B.; Peimyoo, N.; Zou, C.; Chen, Y.; Wang, Y.; Cong, C. et al. Electrically Tunable Valley-Light Emitting Diode (Vled) Based On CVD-Grown Monolayer WS_2. *Nano Letters* **2016**, *16*, 1560-1567.

95. Ovchinnikov, D.; Allain, A.; Huang, Y.; Dumcenco, D.; Kis, A. Electrical Transport Properties Of Single-Layer WS_2. *ACS Nano* **2014**, *8*, 8174-8181.

96. Shanmugam, M.; Jacobs-Gedrim, R.; Song, E.; Yu, B. Two-Dimensional Layered Semiconductor/Graphene Heterostructures For Solar Photovoltaic Applications. *Nanoscale* **2014**, *6*, 12682-12689.

97. Liu, K.; Yan, Q.; Chen, M.; Fan, W.; Sun, Y.; Suh, J.; Fu, D.; Lee, S.; Zhou, J.; Tongay, S. et al. Elastic Properties Of Chemical-Vapor-Deposited Monolayer MoS_2, WS_2, And Their Bilayer Heterostructures. *Nano Letters* **2014**, *14*, 5097-5103.

98. Splendiani, A.; Sun, L.; Zhang, Y.; Li, T.; Kim, J.; Chim, C.; Galli, G.; Wang, F. Emerging Photoluminescence In Monolayer Mos2. *Nano Letters* **2010**, *10*, 1271-1275.

99. Cheiwchanchamnangij, T.; Lambrecht, W. Quasiparticle Band Structure Calculation Of Monolayer, Bilayer, And Bulk MoS_2. *Physical Review B* **2012**, *85*.

100. Zhu, Z.; Cheng, Y.; Schwingenschlögl, U. Giant Spin-Orbit-Induced Spin

Splitting In Two-Dimensional Transition-Metal Dichalcogenide Semiconductors. *Physical Review B* **2011**, *84*.

101. Radisavljevic, B.; Radenovic, A.; Brivio, J.; Giacometti, V.; Kis, A. Single-Layer MoS_2 Transistors. *Nature Nanotechnology* **2011**, *6*, 147-150.

102. Lee, C.; Yan, H.; Brus, L.; Heinz, T.; Hone, J.; Ryu, S. Anomalous Lattice Vibrations Of Single- And Few-Layer MoS_2. *ACS Nano* **2010**, *4*, 2695-2700.

103. Rice, C.; Young, R.; Zan, R.; Bangert, U.; Wolverson, D.; Georgiou, T.; Jalil, R.; Novoselov, K. Raman-Scattering Measurements And First-Principles Calculations Of Strain-Induced Phonon Shifts In Monolayer MoS_2. *Physical Review B* **2013**, *87*.

104. Mak, K.; Lee, C.; Hone, J.; Shan, J.; Heinz, T. Atomically Thin MoS_2: A New Direct-Gap Semiconductor. *Physical Review Letters* **2010**, *105*.

105. Mouri, S.; Miyauchi, Y.; Matsuda, K. Tunable Photoluminescence Of Monolayer MoS_2 Via Chemical Doping. *Nano Letters* **2013**, *13*, 5944-5948.

106. Mak, K.; He, K.; Lee, C.; Lee, G.; Hone, J.; Heinz, T.; Shan, J. Tightly Bound Trions In Monolayer MoS_2. *Nature Materials* **2012**, *12*, 207-211.

107. Sun, J.; Li, X.; Guo, W.; Zhao, M.; Fan, X.; Dong, Y.; Xu, C.; Deng, J.; Fu, Y. Synthesis Methods Of Two-Dimensional MoS_2: A Brief Review. *Crystals* **2017**, *7*, 198.

108. Zeng, Z.; Yin, Z.; Huang, X.; Li, H.; He, Q.; Lu, G.; Boey, F.; Zhang, H. Single-Layer Semiconducting Nanosheets: High-Yield Preparation And Device Fabrication. *Angewandte Chemie* **2011**, *123*, 11289-11293.

109. Coleman, J.; Lotya, M.; O'Neill, A.; Bergin, S.; King, P.; Khan, U.; Young, K.; Gaucher, A.; De, S.; Smith, R. et al. Two-Dimensional Nanosheets Produced By Liquid Exfoliation Of Layered Materials. *Science* **2011**, *331*, 568-571.

110. Lee, Y.; Zhang, X.; Zhang, W.; Chang, M.; Lin, C.; Chang, K.; Yu, Y.; Wang, J.; Chang, C.; Li, L. et al. Synthesis Of Large-Area MoS_2 atomic Layers With Chemical Vapor Deposition. *Advanced Materials* **2012**, *24*, 2320-2325.

111. Yu, Y.; Li, C.; Liu, Y.; Su, L.; Zhang, Y.; Cao, L. Controlled Scalable Synthesis Of Uniform, High-Quality Monolayer And Few-Layer MoS_2 Films. *Scientific Reports* **2013**, *3*.

112. Kang, K.; Xie, S.; Huang, L.; Han, Y.; Huang, P.; Mak, K.; Kim, C.; Muller, D.; Park, J. High-Mobility Three-Atom-Thick Semiconducting Films With Wafer-Scale Homogeneity. *Nature* **2015**, *520*, 656-660.

113. Valdivia, A.; Tweet, D.; Conley, J. Atomic Layer Deposition Of Two Dimensional MoS_2 On 150 mm Substrates. *Journal of Vacuum Science & Technology A: Vacuum, Surfaces, and Films* **2016**, *34*, 021515.

114. Nandi, D.; Sen, U.; Choudhury, D.; Mitra, S.; Sarkar, S. Atomic Layer Deposited MoS_2 As A Carbon And Binder Free Anode In Li-Ion Battery. *Electrochimica Acta* **2014**, *146*, 706-713.

115. Pyeon, J.; Kim, S.; Jeong, D.; Baek, S.; Kang, C.; Kim, J.; Kim, S. Wafer-Scale Growth Of MoS_2 thin Films By Atomic Layer Deposition. *Nanoscale* **2016**, *8*, 10792-10798.

116. Jang, Y.; Yeo, S.; Lee, H.; Kim, H.; Kim, S. Wafer-Scale, Conformal And

Direct Growth Of MoS_2 Thin Films By Atomic Layer Deposition. *Applied Surface Science* **2016**, *365*, 160-165.

117. Jin, Z.; Shin, S.; Kwon, D.; Han, S.; Min, Y. Novel Chemical Route For Atomic Layer Deposition Of MoS_2 Thin Film On SiO_2/Si Substrate. *Nanoscale* **2014**, *6*, 14453-14458.

118. Shin, S.; Jin, Z.; Kwon, D.; Bose, R.; Min, Y. High Turnover Frequency Of Hydrogen Evolution Reaction On Amorphous MoS_2 thin Film Directly Grown By Atomic Layer Deposition. *Langmuir* **2015**, *31*, 1196-1202.

119. Kuc, A.; Zibouche, N.; Heine, T. Influence Of Quantum Confinement On The Electronic Structure Of The Transition Metal Sulfidets2. *Physical Review B* **2011**, *83*.

120. Zhang, Y.; Zhang, Y.; Ji, Q.; Ju, J.; Yuan, H.; Shi, J.; Gao, T.; Ma, D.; Liu, M.; Chen, Y. et al. Controlled Growth Of High-Quality Monolayer WS_2 Layers On Sapphire And Imaging Its Grain Boundary. *ACS Nano* **2013**, *7*, 8963-8971.

121. Dumcenco, D.; Ovchinnikov, D.; Lopez Sanchez, O.; Gillet, P.; Alexander, D.; Lazar, S.; Radenovic, A.; Kis, A. Large-Area MoS_2 grown Using H_2S As The Sulphur Source. *2D Materials* **2015**, *2*, 044005.

122. Li, H.; Du, M.; Mleczko, M.; Koh, A.; Nishi, Y.; Pop, E.; Bard, A.; Zheng, X. Kinetic Study Of Hydrogen Evolution Reaction Over Strained MoS_2 With Sulfur Vacancies Using Scanning Electrochemical Microscopy. *Journal of the American Chemical Society* **2016**, *138*, 5123-5129.

123. Xiao, D.; Liu, G.; Feng, W.; Xu, X.; Yao, W. Coupled Spin And Valley Physics

In Monolayers Of MoS_2 and Other Group-VI Dichalcogenides. *Physical Review Letters* **2012**, *108*.

124. Frey, G.; Tenne, R.; Matthews, M.; Dresselhaus, M.; Dresselhaus, G. Optical Properties Of MS_2 (M = Mo, W) Inorganic Fullerenelike And Nanotube Material Optical Absorption And Resonance Raman Measurements. *Journal of Materials Research* **1998**, *13*, 2412-2417.

125. Ballif, C.; Regula, M.; Schmid, P.; Remškar, M.; Sanjinés, R.; Lévy, F. Preparation And Characterization Of Highly Oriented, Photoconducting WS_2 Thin Films. *Applied Physics A Materials Science & Processing* **1996**, *62*, 543-546.

126. Jo, S.; Ubrig, N.; Berger, H.; Kuzmenko, A.; Morpurgo, A. Mono- And Bilayer WS_2 Light-Emitting Transistors. *Nano Letters* **2014**, *14*, 2019-2025.

127. Withers, F.; Bointon, T.; Hudson, D.; Craciun, M.; Russo, S. Electron Transport Of WS2 Transistors In A Hexagonal Boron Nitride Dielectric Environment. *Scientific Reports* **2014**, *4*.

128. Berkdemir, A.; Gutiérrez, H.; Botello-Méndez, A.; Perea-López, N.; Elías, A.; Chia, C.; Wang, B.; Crespi, V.; López-Urías, F.; Charlier, J. et al. Identification Of Individual And Few Layers Of WS_2 Using Raman Spectroscopy. *Scientific Reports* **2013**, *3*.

129. Li, H.; Zhang, Q.; Yap, C.; Tay, B.; Edwin, T.; Olivier, A.; Baillargeat, D. From Bulk To Monolayer MoS_2: Evolution Of Raman Scattering. *Advanced Functional Materials* **2012**, *22*, 1385-1390.

130. Wang, F.; Kinloch, I.; Wolverson, D.; Tenne, R.; Zak, A.; O'Connell, E.;

Bangert, U.; Young, R. Strain-Induced Phonon Shifts In Tungsten Disulfide Nanoplatelets And Nanotubes. *2D Materials* **2016**, *4*, 015007.

131. Rong, Y.; Fan, Y.; Leen Koh, A.; Robertson, A.; He, K.; Wang, S.; Tan, H.; Sinclair, R.; Warner, J. Controlling Sulphur Precursor Addition For Large Single Crystal Domains Of WS2. *Nanoscale* **2014**, *6*, 12096-12103.

132. Peimyoo, N.; Shang, J.; Cong, C.; Shen, X.; Wu, X.; Yeow, E.; Yu, T. Nonblinking, Intense Two-Dimensional Light Emitter: Monolayer WS_2 Triangles. *ACS Nano* **2013**, *7*, 10985-10994.

133. Chow, P.; Jacobs-Gedrim, R.; Gao, J.; Lu, T.; Yu, B.; Terrones, H.; Koratkar, N. Defect-Induced Photoluminescence In Monolayer Semiconducting Transition Metal Dichalcogenides. *ACS Nano* **2015**, *9*, 1520-1527.

134. Zhu, B.; Chen, X.; Cui, X. Exciton Binding Energy Of Monolayer WS_2. *Scientific Reports* **2015**, *5*.

135. Fan, X.; Zheng, W.; Liu, H.; Zhuang, X.; Fan, P.; Gong, Y.; Li, H.; Wu, X.; Jiang, Y.; Zhu, X. et al. Nonlinear Photoluminescence In Monolayer WS_2: Parabolic Emission And Excitation Fluence-Dependent Recombination Dynamics. *Nanoscale* **2017**, *9*, 7235-7241.

136. Ye, Z.; Cao, T.; O'Brien, K.; Zhu, H.; Yin, X.; Wang, Y.; Louie, S.; Zhang, X. Probing Excitonic Dark States In Single-Layer Tungsten Disulphide. *Nature* **2014**, *513*, 214-218.

137. Zhu, B.; Zeng, H.; Dai, J.; Gong, Z.; Cui, X. Anomalously Robust Valley Polarization And Valley Coherence In Bilayer WS_2. *Proceedings of the National*

Academy of Sciences **2014**, *111*, 11606-11611.

138. Modtland, B.; Navarro-Moratalla, E.; Ji, X.; Baldo, M.; Kong, J. Monolayer Tungsten Disulfide (WS_2) Via Chlorine-Driven Chemical Vapor Transport. *Small* **2017**, *13*, 1701232.

139. Hu, D.; Xu, G.; Xing, L.; Yan, X.; Wang, J.; Zheng, J.; Lu, Z.; Wang, P.; Pan, X.; Jiao, L. Two-Dimensional Semiconductors Grown By Chemical Vapor Transport. *Angewandte Chemie* **2017**, *129*, 3665-3669.

140. Smith, R.; King, P.; Lotya, M.; Wirtz, C.; Khan, U.; De, S.; O'Neill, A.; Duesberg, G.; Grunlan, J.; Moriarty, G. et al. Large-Scale Exfoliation Of Inorganic Layered Compounds In Aqueous Surfactant Solutions. *Advanced Materials* **2011**, *23*, 3944-3948.

141. Dines, M. Lithium Intercalation Via -Butyllithium Of The Layered Transition Metal Dichalcogenides. *Materials Research Bulletin* **1975**, *10*, 287-291.

142. Osada, M.; Sasaki, T. Exfoliated Oxide Nanosheets: New Solution To Nanoelectronics. *Journal of Materials Chemistry* **2009**, *19*, 2503.

143. Zeng, Z.; Yin, Z.; Huang, X.; Li, H.; He, Q.; Lu, G.; Boey, F.; Zhang, H. Single-Layer Semiconducting Nanosheets: High-Yield Preparation And Device Fabrication. *Angewandte Chemie* **2011**, *123*, 11289-11293.

144. Gordon, R.; Yang, D.; Crozier, E.; Jiang, D.; Frindt, R. Structures Of Exfoliated Single Layers Of WS_2, MoS_2, And $MoSe_2$ in Aqueous Suspension. *Physical Review B* **2002**, *65*.

145. Kappera, R.; Voiry, D.; Yalcin, S.; Branch, B.; Gupta, G.; Mohite, A.;

Chhowalla, M. Phase-Engineered Low-Resistance Contacts For Ultrathin MoS_2 Transistors. *Nature Materials* **2014**, *13*, 1128-1134.

146. Elías, A.; Perea-López, N.; Castro-Beltrán, A.; Berkdemir, A.; Lv, R.; Feng, S.; Long, A.; Hayashi, T.; Kim, Y.; Endo, M. et al. Controlled Synthesis And Transfer Of Large-Area WS_2 Sheets: From Single Layer To Few Layers. *ACS Nano* **2013**, *7*, 5235-5242.

147. Perea-López, N.; Elías, A.; Berkdemir, A.; Castro-Beltran, A.; Gutiérrez, H.; Feng, S.; Lv, R.; Hayashi, T.; López-Urías, F.; Ghosh, S. et al. Photosensor Device Based On Few-Layered WS_2 films. *Advanced Functional Materials* **2013**, *23*, 5511-5517.

148. Hussain, S.; Khan, M.; Shehzad, M.; Vikraman, D.; Iqbal, M.; Choi, D.; Song, W.; An, K.; Seo, Y.; Eom, J. et al. Layer-Modulated, Wafer Scale And Continuous Ultra-Thin WS_2 Films Grown By RF Sputtering Via Post-Deposition Annealing. *Journal of Materials Chemistry C* 2016, *4*, 7846-7852.

149. Song, J.; Park, J.; Lee, W.; Choi, T.; Jung, H.; Lee, C.; Hwang, S.; Myoung, J.; Jung, J.; Kim, S. et al. Layer-Controlled, Wafer-Scale, And Conformal Synthesis Of Tungsten Disulfide Nanosheets Using Atomic Layer Deposition. *ACS Nano* **2013**, *7*, 11333-11340.

150. Lee, Y.; Yu, L.; Wang, H.; Fang, W.; Ling, X.; Shi, Y.; Lin, C.; Huang, J.; Chang, M.; Chang, C. et al. Synthesis And Transfer Of Single-Layer Transition Metal Disulfides On Diverse Surfaces. *Nano Letters* **2013**, *13*, 1852-1857.

151. Cong, C.; Shang, J.; Wu, X.; Cao, B.; Peimyoo, N.; Qiu, C.; Sun, L.; Yu, T.

Synthesis And Optical Properties Of Large-Area Single-Crystalline 2D Semiconductor WS_2 monolayer From Chemical Vapor Deposition. *Advanced Optical Materials* **2013**, *2*, 131-136.

152. Kang, K.; Godin, K.; Yang, E. The Growth Scale And Kinetics Of WS_2 Monolayers Under Varying H_2 Concentration. *Scientific Reports* **2015**, *5*.

153. Sheng, Y.; Tan, H.; Wang, X.; Warner, J. Hydrogen Addition For Centimeter-Sized Monolayer Tungsten Disulfide Continuous Films By Ambient Pressure Chemical Vapor Deposition. *Chemistry of Materials* **2017**, *29*, 4904-4911.

154. Groven, B.; Claes, D.; Nalin Mehta, A.; Bender, H.; Vandervorst, W.; Heyns, M.; Caymax, M.; Radu, I.; Delabie, A. Chemical Vapor Deposition Of Monolayer-Thin WS_2 Crystals From The WF_6 And H_2S Precursors At Low Deposition Temperature. *The Journal of Chemical Physics* **2019**, *150*, 104703.

155. Late, D.; Liu, B.; Luo, J.; Yan, A.; Matte, H.; Grayson, M.; Rao, C.; Dravid, V. GaS And GaSe Ultrathin Layer Transistors. *Advanced Materials* **2012**, *24*, 3549-3554.

156. Hu, P.; Wang, L.; Yoon, M.; Zhang, J.; Feng, W.; Wang, X.; Wen, Z.; Idrobo, J.; Miyamoto, Y.; Geohegan, D. et al. Highly Responsive Ultrathin GaS Nanosheet Photodetectors On Rigid And Flexible Substrates. *Nano Letters* **2013**, *13*, 1649-1654.

157. Ma, Y.; Dai, Y.; Guo, M.; Yu, L.; Huang, B. Tunable Electronic And Dielectric Behavior Of GaS And GaSe Monolayers. *Physical Chemistry Chemical Physics* **2013**, *15*, 7098.

158. Yang, S.; Li, Y.; Wang, X.; Huo, N.; Xia, J.; Li, S.; Li, J. High Performance Few-Layer GaS Photodetector And Its Unique Photo-Response In Different Gas Environments. *Nanoscale* **2014**, *6*, 2582-2587.

159. Meng, X.; He, K.; Su, D.; Zhang, X.; Sun, C.; Ren, Y.; Wang, H.; Weng, W.; Trahey, L.; Canlas, C. et al. Gallium Sulfide-Single-Walled Carbon Nanotube Composites: High-Performance Anodes For Lithium-Ion Batteries. *Advanced Functional Materials* **2014**, *24*, 5435-5442.

160. Barron, A. MOCVD Of Group III Chalcogenides. *Advanced Materials for Optics and Electronics* **1995**, *5*, 245-258.

161. Chen, Z.; Huang, L.; Xi, Y.; Li, R.; Li, W.; Xu, G.; Cheng, H. Geometrical Structures, And Electronic And Transport Properties Of A Novel Two-Dimensional B-GaS Transparent Conductor. *Nano Research* **2015**, *8*, 3177-3185.

162. Late, D.; Liu, B.; Matte, H.; Rao, C.; Dravid, V. Rapid Characterization Of Ultrathin Layers Of Chalcogenides On SiO_2/Si Substrates. *Advanced Functional Materials* **2012**, *22*, 1894-1905.

163. Watanabe, K.; Taniguchi, T.; Kanda, H. Direct-Bandgap Properties And Evidence For Ultraviolet Lasing Of Hexagonal Boron Nitride Single Crystal. *Nature Materials* **2004**, *3*, 404-409.

164. Gasanly, N.; Aydınlı, A.; Özkan, H.; Kocabaş, C. Temperature Dependence Of The First-Order Raman Scattering In GaS Layered Crystals. *Solid State Communications* **2000**, *116*, 147-151.

165. MacInnes, A.; Power, M.; Barron, A. Chemical Vapor Deposition Of Cubic

Gallium Sulfide Thin Films: A New Metastable Phase. *Chemistry of Materials* **1992**, *4*, 11-14.

166. Shen, G.; Chen, D.; Chen, P.; Zhou, C. Vapor−Solid Growth Of One-Dimensional Layer-Structured Gallium Sulfide Nanostructures. *ACS Nano* **2009**, *3*, 1115-1120.

167. Wang, X.; Sheng, Y.; Chang, R.; Lee, J.; Zhou, Y.; Li, S.; Chen, T.; Huang, H.; Porter, B.; Bhaskaran, H. et al. Chemical Vapor Deposition Growth Of Two-Dimensional Monolayer Gallium Sulfide Crystals Using Hydrogen Reduction Of Ga_2S_3. *ACS Omega* **2018**, *3*, 7897-7903.

168. Buscema, M.; Island, J.; Groenendijk, D.; Blanter, S.; Steele, G.; van der Zant, H.; Castellanos-Gomez, A. Photocurrent Generation With Two-Dimensional Van Der Waals Semiconductors. *Chemical Society Reviews* **2015**, *44*, 3691-3718.

169. Xie, C.; Mak, C.; Tao, X.; Yan, F. Photodetectors Based On Two-Dimensional Layered Materials Beyond Graphene. *Advanced Functional Materials* **2016**, *27*, 1603886.

170. Wang, J.; Fang, H.; Wang, X.; Chen, X.; Lu, W.; Hu, W. Recent Progress On Localized Field Enhanced Two-Dimensional Material Photodetectors From Ultraviolet-Visible To Infrared. *Small* **2017**, *13*, 1700894.

171. Soref, R. Silicon-Based Optoelectronics. *Proceedings of the IEEE* **1993**, *81*, 1687-1706.

172. Rogalski, A. Hgcdte Infrared Detector Material: History, Status And Outlook. *Reports on Progress in Physics* **2005**, *68*, 2267-2336.

173. Choi, W.; Choudhary, N.; Han, G.; Park, J.; Akinwande, D.; Lee, Y. Recent Development Of Two-Dimensional Transition Metal Dichalcogenides And Their Applications. *Materials Today* **2017**, *20*, 116-130.

174. Ghatak, S.; Pal, A.; Ghosh, A. Nature Of Electronic States In Atomically Thin MoS_2 Field-Effect Transistors. *ACS Nano* **2011**, *5*, 7707-7712.

175. Fang, H.; Hu, W. Photogating In Low Dimensional Photodetectors. *Advanced Science* **2017**, *4*, 1700323.

176. Koppens, F.; Mueller, T.; Avouris, P.; Ferrari, A.; Vitiello, M.; Polini, M. Photodetectors Based On Graphene, Other Two-Dimensional Materials And Hybrid Systems. *Nature Nanotechnology* **2014**, *9*, 780-793.

177. Konstantatos, G.; Badioli, M.; Gaudreau, L.; Osmond, J.; Bernechea, M.; de Arquer, F.; Gatti, F.; Koppens, F. Hybrid Graphene–Quantum Dot Phototransistors With Ultrahigh Gain. *Nature Nanotechnology* **2012**, 7, 363-368.

178. Zhang, W.; Huang, J.; Chen, C.; Chang, Y.; Cheng, Y.; Li, L. High-Gain Phototransistors Based On A CVD MoS_2 monolayer. *Advanced Materials* **2013**, *25*, 3456-3461.

179. Frisenda, R.; Molina-Mendoza, A.; Mueller, T.; Castellanos-Gomez, A.; van der Zant, H. Atomically Thin P–N Junctions Based On Two-Dimensional Materials. *Chemical Society Reviews* **2018**, *47*, 3339-3358.

180. Zhang, W.; Chiu, M.; Chen, C.; Chen, W.; Li, L.; Wee, A. Role Of Metal Contacts In High-Performance Phototransistors Based On WSe_2 Monolayers. *ACS Nano* **2014**, *8*, 8653-8661.

181. Allain, A.; Kang, J.; Banerjee, K.; Kis, A. Electrical Contacts To Two-Dimensional Semiconductors. *Nature Materials* **2015**, *14*, 1195-1205.

182. Xu, Y.; Cheng, C.; Du, S.; Yang, J.; Yu, B.; Luo, J.; Yin, W.; Li, E.; Dong, S.; Ye, P. et al. Contacts Between Two- And Three-Dimensional Materials: Ohmic, Schottky, And P–N Heterojunctions. *ACS Nano* **2016**, *10*, 4895-4919.

183. Somvanshi, D.; Kallatt, S.; Venkatesh, C.; Nair, S.; Gupta, G.; Anthony, J.; Karmakar, D.; Majumdar, K. Nature Of Carrier Injection In Metal/2D-Semiconductor Interface And Its Implications For The Limits Of Contact Resistance. *Physical Review B* **2017**, *96*.

184. Tung, R. T. The Physics And Chemistry Of The Schottky Barrier Height. *Applied Physics Reviews* **2014**, *1*, 011304.

185. Liu, Y.; Guo, J.; Zhu, E.; Liao, L.; Lee, S.; Ding, M.; Shakir, I.; Gambin, V.; Huang, Y.; Duan, X. Approaching The Schottky–Mott Limit In Van Der Waals Metal–Semiconductor Junctions. *Nature* **2018**, *557*, 696-700.

186. Das, S.; Chen, H.; Penumatcha, A.; Appenzeller, J. High Performance Multilayer MoS_2 Transistors With Scandium Contacts. *Nano Letters* **2012**, *13*, 100-105.

187. Kim, C.; Moon, I.; Lee, D.; Choi, M.; Ahmed, F.; Nam, S.; Cho, Y.; Shin, H.; Park, S.; Yoo, W. Fermi Level Pinning At Electrical Metal Contacts Of Monolayer Molybdenum Dichalcogenides. *ACS Nano* **2017**, *11*, 1588-1596.

188. Schulman, D.; Arnold, A.; Das, S. Contact Engineering For 2D Materials And Devices. *Chemical Society Reviews* **2018**, *47*, 3037-3058.

189. Liu, Y.; Wu, H.; Cheng, H.; Yang, S.; Zhu, E.; He, Q.; Ding, M.; Li, D.; Guo, J.; Weiss, N. et al. Toward Barrier Free Contact To Molybdenum Disulfide Using Graphene Electrodes. *Nano Letters* **2015**, *15*, 3030-3034.

190. Yu, W.; Li, Z.; Zhou, H.; Chen, Y.; Wang, Y.; Huang, Y.; Duan, X. Vertically Stacked Multi-Heterostructures Of Layered Materials For Logic Transistors And Complementary Inverters. *Nature Materials* **2012**, *12*, 246-252.

191. Liu, Y.; Zhou, H.; Cheng, R.; Yu, W.; Huang, Y.; Duan, X. Highly Flexible Electronics From Scalable Vertical Thin Film Transistors. *Nano Letters* **2014**, *14*, 1413-1418.

192. McDonnell, S.; Addou, R.; Buie, C.; Wallace, R.; Hinkle, C. Defect-Dominated Doping And Contact Resistance In MoS_2. *ACS Nano* **2014**, *8*, 2880-2888.

193. Roy, T.; Tosun, M.; Kang, J.; Sachid, A.; Desai, S.; Hettick, M.; Hu, C.; Javey, A. Field-Effect Transistors Built From All Two-Dimensional Material Components. *ACS Nano* **2014**, *8*, 6259-6264.

194. Lee, K.; Shin, H.; Lee, J.; Lee, I.; Kim, G.; Choi, J.; Kim, S. Large-Scale Synthesis Of High-Quality Hexagonal Boron Nitride Nanosheets For Large-Area Graphene Electronics. *Nano Letters* **2012**, *12*, 714-718.

195. Haigh, S.; Gholinia, A.; Jalil, R.; Romani, S.; Britnell, L.; Elias, D.; Novoselov, K.; Ponomarenko, L.; Geim, A.; Gorbachev, R. Cross-Sectional Imaging Of Individual Layers And Buried Interfaces Of Graphene-Based Heterostructures And Superlattices. *Nature Materials* **2012**, *11*, 764-767.

196. Loan, P.; Zhang, W.; Lin, C.; Wei, K.; Li, L.; Chen, C. Graphene/Mos2heterostructures For Ultrasensitive Detection Of DNA Hybridisation. *Advanced Materials* **2014**, *26*, 4838-4844.

197. Yu, W.; Liu, Y.; Zhou, H.; Yin, A.; Li, Z.; Huang, Y.; Duan, X. Highly Efficient Gate-Tunable Photocurrent Generation In Vertical Heterostructures Of Layered Materials. *Nature Nanotechnology* **2013**, *8*, 952-958.

198. Britnell, L.; Ribeiro, R.; Eckmann, A.; Jalil, R.; Belle, B.; Mishchenko, A.; Kim, Y.; Gorbachev, R.; Georgiou, T.; Morozov, S. et al. Strong Light-Matter Interactions In Heterostructures Of Atomically Thin Films. *Science* **2013**, *340*, 1311-1314.

199. Georgiou, T.; Jalil, R.; Belle, B.; Britnell, L.; Gorbachev, R.; Morozov, S.; Kim, Y.; Gholinia, A.; Haigh, S.; Makarovsky, O. et al. Vertical Field-Effect Transistor Based On Graphene–WS_2 Heterostructures For Flexible And Transparent Electronics. *Nature Nanotechnology* **2012**, *8*, 100-103.

200. Cheng, R.; Li, D.; Zhou, H.; Wang, C.; Yin, A.; Jiang, S.; Liu, Y.; Chen, Y.; Huang, Y.; Duan, X. Electroluminescence And Photocurrent Generation From Atomically Sharp WSe_2/ MoS_2 Heterojunction P–N Diodes. *Nano Letters* **2014**, *14*, 5590-5597.

201. Tongay, S.; Fan, W.; Kang, J.; Park, J.; Koldemir, U.; Suh, J.; Narang, D.; Liu, K.; Ji, J.; Li, J. et al. Tuning Interlayer Coupling In Large-Area Heterostructures With CVD-Grown MoS_2 And WS_2 Monolayers. *Nano Letters* **2014**, *14*, 3185-3190.

202. Huo, N.; Kang, J.; Wei, Z.; Li, S.; Li, J.; Wei, S. Novel And Enhanced

Optoelectronic Performances Of Multilayer MoS_2-WS_2 heterostructure Transistors. *Advanced Functional Materials* **2014**, *24*, 7025-7031.

203. Gao, T.; Song, X.; Du, H.; Nie, Y.; Chen, Y.; Ji, Q.; Sun, J.; Yang, Y.; Zhang, Y.; Liu, Z. Temperature-Triggered Chemical Switching Growth Of In-Plane And Vertically Stacked Graphene-Boron Nitride Heterostructures. *Nature Communications* **2015**, *6*.

204. Song, X.; Gao, T.; Nie, Y.; Zhuang, J.; Sun, J.; Ma, D.; Shi, J.; Lin, Y.; Ding, F.; Zhang, Y. et al. Seed-Assisted Growth Of Single-Crystalline Patterned Graphene Domains On Hexagonal Boron Nitride By Chemical Vapor Deposition. *Nano Letters* **2016**, *16*, 6109-6116.

205. Okada, M.; Sawazaki, T.; Watanabe, K.; Taniguch, T.; Hibino, H.; Shinohara, H.; Kitaura, R. Direct Chemical Vapor Deposition Growth Of WS_2 Atomic Layers On Hexagonal Boron Nitride. *ACS Nano* **2014**, *8*, 8273-8277.

206. Zhang, X.; Zhang, F.; Wang, Y.; Schulman, D.; Zhang, T.; Bansal, A.; Alem, N.; Das, S.; Crespi, V.; Terrones, M. et al. Defect-Controlled Nucleation And Orientation Of WSe_2 On hBN: A Route To Single-Crystal Epitaxial Monolayers. *ACS Nano* **2019**, *13*, 3341-3352.

207. Wang, S.; Wang, X.; Warner, J. All Chemical Vapor Deposition Growth Of MoS_2:H-BN Vertical Van Der Waals Heterostructures. *ACS Nano* **2015**, *9*, 5246-5254.

208. Shi, Y.; Zhou, W.; Lu, A.; Fang, W.; Lee, Y.; Hsu, A.; Kim, S.; Kim, K.; Yang, H.; Li, L. et al. Van Der Waals Epitaxy Of MoS_2 Layers Using Graphene As Growth

Templates. *Nano Letters* **2012**, *12*, 2784-2791.

209. Bianco, G.; Losurdo, M.; Giangregorio, M.; Sacchetti, A.; Prete, P.; Lovergine, N.; Capezzuto, P.; Bruno, G. Direct Epitaxial CVD Synthesis Of Tungsten Disulfide On Epitaxial And CVD Graphene. *RSC Advances* **2015**, *5*, 98700-98708.

210. Gong, Y.; Lin, J.; Wang, X.; Shi, G.; Lei, S.; Lin, Z.; Zou, X.; Ye, G.; Vajtai, R.; Yakobson, B. et al. Vertical And In-Plane Heterostructures From WS_2/ MoS_2 Monolayers. *Nature Materials* **2014**, *13*, 1135-1142.

211. Zhou, X.; Zhou, N.; Li, C.; Song, H.; Zhang, Q.; Hu, X.; Gan, L.; Li, H.; Lü, J.; Luo, J. et al. Vertical Heterostructures Based On $SnSe_2$/MoS_2 For High Performance Photodetectors. *2D Materials* **2017**, *4*, 025048.

212. Han, G.; Rodríguez-Manzo, J.; Lee, C.; Kybert, N.; Lerner, M.; Qi, Z.; Dattoli, E.; Rappe, A.; Drndic, M.; Johnson, A. Continuous Growth Of Hexagonal Graphene And Boron Nitride In-Plane Heterostructures By Atmospheric Pressure Chemical Vapor Deposition. *ACS Nano* **2013**, *7*, 10129-10138.

213. Liu, L.; Park, J.; Siegel, D.; McCarty, K.; Clark, K.; Deng, W.; Basile, L.; Idrobo, J.; Li, A.; Gu, G. Heteroepitaxial Growth Of Two-Dimensional Hexagonal Boron Nitride Templated By Graphene Edges. *Science* **2014**, *343*, 163-167.

214. Zhao, M.; Ye, Y.; Han, Y.; Xia, Y.; Zhu, H.; Wang, S.; Wang, Y.; Muller, D.; Zhang, X. Large-Scale Chemical Assembly Of Atomically Thin Transistors And Circuits. *Nature Nanotechnology* **2016**, *11*, 954-959.

215. Zheng, C.; Zhang, Q.; Weber, B.; Ilatikhameneh, H.; Chen, F.; Sahasrabudhe, H.; Rahman, R.; Li, S.; Chen, Z.; Hellerstedt, J. et al. Direct Observation Of 2D

Electrostatics And Ohmic Contacts In Template-Grown Graphene/WS_2 Heterostructures. *ACS Nano* **2017**, *11*, 2785-2793.

216. Tang, H.; Chiu, M.; Tseng, C.; Yang, S.; Hou, K.; Wei, S.; Huang, J.; Lin, Y.; Lien, C.; Li, L. Multilayer Graphene–Wse2 Heterostructures For WSe_2 Transistors. *ACS Nano* **2017**, *11*, 12817-12823.

217. Chen, K.; Wan, X.; Wen, J.; Xie, W.; Kang, Z.; Zeng, X.; Chen, H.; Xu, J. Electronic Properties Of MoS_2–WS_2 Heterostructures Synthesized With Two-Step Lateral Epitaxial Strategy. *ACS Nano* **2015**, *9*, 9868-9876.

218. Heo, H.; Sung, J.; Jin, G.; Ahn, J.; Kim, K.; Lee, M.; Cha, S.; Choi, H.; Jo, M. Rotation-Misfit-Free Heteroepitaxial Stacking And Stitching Growth Of Hexagonal Transition-Metal Dichalcogenide Monolayers By Nucleation Kinetics Controls. *Advanced Materials* **2015**, *27*, 3803-3810.

219. Huang, C.; Wu, S.; Sanchez, A.; Peters, J.; Beanland, R.; Ross, J.; Rivera, P.; Yao, W.; Cobden, D.; Xu, X. Lateral Heterojunctions Within Monolayer $MoSe_2$–WSe_2 Semiconductors. *Nature Materials* **2014**, *13*, 1096-1101.

220. Gong, Y.; Lei, S.; Ye, G.; Li, B.; He, Y.; Keyshar, K.; Zhang, X.; Wang, Q.; Lou, J.; Liu, Z. et al. Two-Step Growth Of Two-Dimensional WSe_2/$MoSe_2$ Heterostructures. *Nano Letters* **2015**, *15*, 6135-6141.

221. Duan, X.; Wang, C.; Shaw, J.; Cheng, R.; Chen, Y.; Li, H.; Wu, X.; Tang, Y.; Zhang, Q.; Pan, A. et al. Lateral Epitaxial Growth Of Two-Dimensional Layered Semiconductor Heterojunctions. *Nature Nanotechnology* **2014**, *9*, 1024-1030.

222. Li, M.; Pu, J.; Huang, J.; Miyauchi, Y.; Matsuda, K.; Takenobu, T.; Li, L. Self-

Aligned And Scalable Growth Of Monolayer WSe_2- MoS_2 Lateral Heterojunctions. *Advanced Functional Materials* **2018**, *28*, 1706860.

223. Li, M.; Shi, Y.; Cheng, C.; Lu, L.; Lin, Y.; Tang, H.; Tsai, M.; Chu, C.; Wei, K.; He, J. et al. Epitaxial Growth Of A Monolayer WSe_2-MoS_2 Lateral P-N Junction With An Atomically Sharp Interface. *Science* **2015**, *349*, 524-528.

224. Wang, X.; Hooper, T.; Kumar, A.; Priest, I.; Sheng, Y.; Samuels, T.; Wang, S.; Robertson, A.; Pacios, M.; Bhaskaran, H.; Weller, A; Warner, J.. Oligomeric Aminoborane Precursors For The Chemical Vapour Deposition Growth Of Few-Layer Hexagonal Boron Nitride. *CrystEngComm* **2017**, *19*, 285-294.

225. Ramakrishna Matte, H.; Gomathi, A.; Manna, A.; Late, D.; Datta, R.; Pati, S.; Rao, C. MoS_2 And WS_2 Analogues Of Graphene. *Angewandte Chemie* **2010**, *122*, 4153-4156.

226. Huang, J.; Pu, J.; Hsu, C.; Chiu, M.; Juang, Z.; Chang, Y.; Chang, W.; Iwasa, Y.; Takenobu, T.; Li, L. Large-Area Synthesis Of Highly Crystalline WSe_2 monolayers And Device Applications. *ACS Nano* **2014**, *8*, 923-930.

227. Wang, X.; Gong, Y.; Shi, G.; Chow, W.; Keyshar, K.; Ye, G.; Vajtai, R.; Lou, J.; Liu, Z.; Ringe, E; Tay. B.; Ajayan, P.. Chemical Vapor Deposition Growth Of Crystalline Monolayer Mose2. *ACS Nano* **2014**, *8*, 5125-5131.

228. Mas-Ballesté, R.; Gómez-Navarro, C.; Gómez-Herrero, J.; Zamora, F. 2D Materials: To Graphene And Beyond. *Nanoscale* **2011**, *3*, 20-30.

229. Li, H.; Yin, Z.; He, Q.; Li, H.; Huang, X.; Lu, G.; Fam, D.; Tok, A.; Zhang, Q.; Zhang, H. Fabrication Of Single- And Multilayer MoS_2 Film-Based Field-Effect

Transistors For Sensing NO At Room Temperature. *Small* **2011**, *8*, 63-67.

230. Geim, A.; Grigorieva, I. Van Der Waals Heterostructures. *Nature* **2013**, *499*, 419-425.

231. Sheng, Y.; Xu, W.; Wang, X.; He, Z.; Rong, Y.; Warner, J. Mixed Multilayered Vertical Heterostructures Utilizing Strained Monolayer WS_2. *Nanoscale* **2016**, *8*, 2639-2647.

232. Tsai, M.; Su, S.; Chang, J.; Tsai, D.; Chen, C.; Wu, C.; Li, L.; Chen, L.; He, J. Monolayer MoS_2 heterojunction Solar Cells. *ACS Nano* **2014**, *8*, 8317-8322.

233. Bertolazzi, S.; Krasnozhon, D.; Kis, A. Nonvolatile Memory Cells Based On MoS_2/Graphene Heterostructures. *ACS Nano* **2013**, *7*, 3246-3252.

234. Lee, G.; Yu, Y.; Cui, X.; Petrone, N.; Lee, C.; Choi, M.; Lee, D.; Lee, C.; Yoo, W.; Watanabe, K; Taneguchi, T.; Nuckolls, C.; Kim, P.; Hone, J.. Flexible And Transparent MoS_2 field-Effect Transistors On Hexagonal Boron Nitride-Graphene Heterostructures. *ACS Nano* **2013**, *7*, 7931-7936.

235. Zhang, W.; Chuu, C.; Huang, J.; Chen, C.; Tsai, M.; Chang, Y.; Liang, C.; Chen, Y.; Chueh, Y.; He, J.; Chou, M.; Li, L.. Ultrahigh-Gain Photodetectors Based On Atomically Thin Graphene- MoS_2 Heterostructures. *Scientific Reports* **2014**, *4*.

236. Roy, K.; Padmanabhan, M.; Goswami, S.; Sai, T.; Ramalingam, G.; Raghavan, S.; Ghosh, A. Graphene–MoS_2 Hybrid Structures For Multifunctional Photoresponsive Memory Devices. *Nature Nanotechnology* **2013**, *8*, 826-830.

237. Ling, Z.; Yang, R.; Chai, J.; Wang, S.; Leong, W.; Tong, Y.; Lei, D.; Zhou, Q.; Gong, X.; Chi, D.; Ang, K.. Large-Scale Two-Dimensional MoS_2 Photodetectors

By Magnetron Sputtering. *Optics Express* **2015**, 23, 13580.

238. Schmidt, H.; Wang, S.; Chu, L.; Toh, M.; Kumar, R.; Zhao, W.; Neto, A. H. C.; Martin, J.; Adam, S.;Ozyilmaz, B.; Eda, G.Transport Properties of Monolayer MoS_2 Grown by Chemical Vapor Deposition *Nano Lett.* **2014**, 14, 1909– 1913

239. Ago, H.; Endo, H.; Solís-Fernández, P.; Takizawa, R.; Ohta, Y.; Fujita, Y.; Yamamoto, K.; Tsuji, M. Controlled Van Der Waals Epitaxy Of Monolayer MoS_2 triangular Domains On Graphene. *ACS Applied Materials & Interfaces* **2015**, *7*, 5265-5273.

240. Chen, C.; Feng, Z.; Feng, Y.; Yue, Y.; Qin, C.; Zhang, D.; Feng, W. Large-Scale Synthesis Of A Uniform Film Of Bilayer MoS_2 on Graphene For 2D Heterostructure Phototransistors. *ACS Applied Materials & Interfaces* **2016**, *8*, 19004-19011.

241. Wang, S.; Pacios, M.; Bhaskaran, H.; Warner, J. Substrate Control For Large Area Continuous Films Of Monolayer MoS_2 by Atmospheric Pressure Chemical Vapor Deposition. *Nanotechnology* **2016**, *27*, 085604.

242. Feng, H.; Wang, X.; Wu, D. Fabrication Of Spirocyclic Phosphazene Epoxy-Based Nanocomposites With Graphene Via Exfoliation Of Graphite Platelets And Thermal Curing For Enhancement Of Mechanical And Conductive Properties. *Industrial & Engineering Chemistry Research* **2013**, *52*, 10160-10171.

243. Park, C.; Zhao, Y.; Kim, H.; Shon, Y.; Kim, E. Resistivity Peaks And Magnetic Properties Of An Annealed Graphene. *Chem. Commun.* **2014**, *50*, 12930-12932.

244. Yang, M.; Cheng, X.; Li, Y.; Ren, Y.; Liu, M.; Qi, Z. Anharmonicity Of

Monolayer Mos2, Mose2, And Wse2: A Raman Study Under High Pressure And Elevated Temperature. *Applied Physics Letters* **2017**, *110*, 093108.

245. Buscema, M.; Steele, G.; van der Zant, H.; Castellanos-Gomez, A. The Effect Of The Substrate On The Raman And Photoluminescence Emission Of Single-Layer MoS_2. *Nano Research* **2014**, *7*, 561-571.

246. Yang, L.; Cui, X.; Zhang, J.; Wang, K.; Shen, M.; Zeng, S.; Dayeh, S.; Feng, L.; Xiang, B. Lattice Strain Effects On The Optical Properties Of MoS_2 Nanosheets. *Scientific Reports* **2014**, *4*.

247. Wan, W.; Li, X.; Li, X.; Xu, B.; Zhan, L.; Zhao, Z.; Zhang, P.; Wu, S.; Zhu, Z.; Huang, H.; Zhou, Y.; Cai, W.. Interlayer Coupling Of A Direct Van Der Waals Epitaxial MoS_2/Graphene Heterostructure. *RSC Adv.* **2016**, *6*, 323-330.

248. Tongay, S.; Suh, J.; Ataca, C.; Fan, W.; Luce, A.; Kang, J.; Liu, J.; Ko, C.; Raghunathanan, R.; Zhou, J.; Ogletree, F.; Li, J,; Grossman, J.; Wu, J.. Defects Activated Photoluminescence In Two-Dimensional Semiconductors: Interplay Between Bound, Charged, And Free Excitons. *Scientific Reports* **2013**, *3*.

249. Conley, H.; Wang, B.; Ziegler, J.; Haglund, R.; Pantelides, S.; Bolotin, K. Bandgap Engineering Of Strained Monolayer And Bilayer Mos2. *Nano Letters* **2013**, 13, 3626-3630.

250. Tan, H.; Fan, Y.; Zhou, Y.; Chen, Q.; Xu, W.; Warner, J. Ultrathin 2D Photodetectors Utilizing Chemical Vapor Deposition Grown WS_2 with Graphene Electrodes. *ACS Nano* **2016**, *10*, 7866-7873.

251. Tan, H.; Fan, Y.; Rong, Y.; Porter, B.; Lau, C.; Zhou, Y.; He, Z.; Wang, S.;

Bhaskaran, H.; Warner, J. Doping Graphene Transistors Using Vertical Stacked Monolayer WS_2 heterostructures Grown By Chemical Vapor Deposition. *ACS Applied Materials & Interfaces* **2016**, *8*, 1644-1652.

252. Yunus, R.; Endo, H.; Tsuji, M.; Ago, H. Vertical Heterostructures Of MoS_2 and Graphene Nanoribbons Grown By Two-Step Chemical Vapor Deposition For High-Gain Photodetectors. Phys. Chem. Chem. Phys. **2015**, 17, 25210-25215.

253. Kim, C.; Kim, S.; Shin, D.; Kang, S.; Kim, J.; Jang, C.; Joo, S.; Lee, J.; Kim, J.; Choi, S.; Hwang, E.. High Photoresponsivity In An All-Graphene P–N Vertical Junction Photodetector. *Nature Communications* **2014**, *5,* 3249.

254. Tsai, D.; Liu, K.; Lien, D.; Tsai, M.; Kang, C.; Lin, C.; Li, L.; He, J. Few-Layer MoS_2 with High Broadband Photogain And Fast Optical Switching For Use In Harsh Environments. *ACS Nano* **2013**, *7*, 3905-3911.

255. Lin, Y.; Lu, N.; Perea-Lopez, N.; Li, J.; Lin, Z.; Peng, X.; Lee, C.; Sun, C.; Calderin, L.; Browning, P.; Bresnehan, M.; Kim, M.; Mayer, T.; Terrones, M.; Robinson, J.. Direct Synthesis Of Van Der Waals Solids. *ACS Nano* **2014**, *8*, 3715-3723.

256. Partoens, B.; Peeters, F. M. From Graphene to Graphite: Electronic Structure around the K Point. *Phys. Rev. B* **2006**, *74*, 075404.

257. Tan, Y.-W.; Zhang, Y.; Bolotin, K.; Zhao, Y.; Adam, S.; Hwang, E. H.; Sarma, S. D.; Stormer, H. L.; Kim, P. Measurement of Scattering Rate and Minimum Conductivity in Graphene. *Phys. Rev. Lett.* **2007**, *99*, 246803.

258. Chang, R.-J.; Wang, X.; Wang, S.; Sheng, Y.; Porter, B.; Bhaskaran, H.; Warner,

J. H. Growth of Large Single-Crystalline Monolayer Hexagonal Boron Nitride by Oxide-Assisted Chemical Vapor Deposition. *Chem. Mater.* **2017**, *29*, 6252–6260.

259. Li, L.; Yu, Y.; Ye, G. J.; Ge, Q.; Ou, X.; Wu, H.; Feng, D.; Chen, X. H.; Zhang, Y. Black Phosphorus Field-Effect Transistors. *Nat. Nanotechnol.* **2014**, *9*, 372–377.

260. Xia, F.; Wang, H.; Jia, Y. Rediscovering Black Phosphorus as an Anisotropic Layered Material for Optoelectronics and Electronics. *Nat. Commun.* **2014**, *5*, 4458.

261. Shaw, J. C.; Zhou, H.; Chen, Y.; Weiss, N. O.; Liu, Y.; Huang, Y.; Duan, X. Chemical Vapor Deposition Growth of Monolayer $MoSe_2$ Nanosheets. *Nano Res.* **2014**, *7*, 511–517.

262. Manzeli, S.; Ovchinnikov, D.; Pasquier, D.; Yazyev, O. V.; Kis, A. 2D Transition Metal Dichalcogenides. *Nat. Rev. Mater.* **2017**, *2*, 17033.

263. Liu, Z.; Ma, L.; Shi, G.; Zhou, W.; Gong, Y.; Lei, S.; Yang, X.; Zhang, J.; Yu, J.; Hackenberg, K. P.; Babakhani, A.; Idrobo, J.-C.; Vajtai, R.; Lou, J.; Ajayan, P. M. In-Plane Heterostructures of Graphene and Hexagonal Boron Nitride with Controlled Domain Sizes. *Nat. Nanotechnol.* **2013**, *8*, 119–124.

264. Ye, M.; Zhang D.; Yap, Y.K. Recent Advances in Electronic and Optoelectronic Devices Based on Two-Dimensional Transition Metal Dichalcogenides. *Electronics* **2017**, *6*, 43.

265. Ponraj, J. S.; Xu, Z. Q.; Dhanabalan, S. C.; Mu, H.,; Wang, Y.; Yuan, J.; Li, P.; Thakur, S.; Ashrafi, M.; Mccoubrey, K.; Zhang, Y.; Li, S.; Zhang, H.; Bao, Q. Photonics and optoelectronics of two-dimensional materials beyond

graphene. *Nanotechnology.* **2016**, *27*, 462001.

266. Dhanabalan, S. C.; Ponraj, J. S.; Zhang, H.; & Bao, Q. Present perspectives of broadband photodetectors based on nanobelts, nanoribbons, nanosheets and the emerging 2D materials. *Nanoscale*, **2016,** *12*, 6410-6434.

267. Dhanabalan, S. C.; Ponraj, J. S.; Guo, Z.; Li, S.; Bao, Q.; Zhang, H. Emerging trends in phosphorene fabrication towards next generation devices. *Adv. Sci.* **2017***, 4*, 1600305.

268. Jariwala, D.; Marks, T. J.; Hersam, M. C. Mixed-dimensional van der Waals heterostructures. *Nat. Mater.*, **2017**, *16*, 170.

269. Xie, C.; Wang, Y.; Zhang, Z. X.; Wang, D.; Luo, L. B. Graphene/semiconductor hybrid heterostructures for optoelectronic device applications. *Nano Today*. **2018**, *19,* 41-83

270. Deng, Y.; Luo, Z.; Conrad, N. J.; Liu, H.; Gong, Y.; Najmaei, S.; Ajayan, P. M.; Lou, J.; Xu, X.; Ye, P. D. Black phosphorus–monolayer MoS2 van der Waals heterojunction p–n diode. *ACS nano* **2014**, *8*, 8292-8299.

271. Zhou, Y.; Tan, H.; Sheng, Y.; Fan, Y.; Xu, W.; Warner, J. H. Utilizing Interlayer Excitons in Bilayer WS_2 for Increased Photovoltaic Response in Ultrathin Graphene Vertical Cross-Bar Photodetecting Tunneling Transistors. *ACS Nano* **2018**, *12*, 4669–4677.

272. Levendorf, M. P.; Kim, C.-J.; Brown, L.; Huang, P. Y.; Havener, R. W.; Muller, D. A.; Park, J. Graphene and Boron Nitride Lateral Heterostructures for Atomically Thin Circuitry. *Nature* **2012**, *488*, 627–632.

273. Gong, Y.; Lin, J.; Wang, X.; Shi, G.; Lei, S.; Lin, Z.; Zou, X.; Ye, G.; Vajtai, R.; Yakobson, B. I.; Terrones, H.; Terrones, M.; Tay, B. K.; Lou, J.; Pantelides, S. T.; Liu, Z.; Zhou, W.; Ajayan, P. M. Vertical and in-Plane Heterostructures from WS_2 /MoS_2 Monolayers. *Nat. Mater.* **2014**, *13*, 1135–1142.

274. Tan, H.; Xu, W.; Sheng, Y.; Lau, C. S.; Fan, Y.; Chen, Q.; Tweedie, M.; Wang, X.; Zhou, Y.; Warner, J. H. Lateral Graphene-Contacted Vertically Stacked WS_2/MoS_2 Hybrid Photodetectors with Large Gain. *Adv. Mater.* **2017**, *29*, 1702917.

275. Shi, J.; Tong, R.; Zhou, X.; Gong, Y.; Zhang, Z.; Ji, Q.; Zhang, Y.; Fang, Q.; Gu, L.; Wang, X.; Liu, Z.; Zhang, Y. Temperature-Mediated Selective Growth of MoS_2/WS_2 and WS_2/MoS_2 Vertical Stacks on Au Foils for Direct Photocatalytic Applications. *Adv. Mater.* **2016**, *28*, 10664–10672.

276. Li, H.; Li, Y.; Aljarb, A.; Shi, Y.; Li, L.-J. Epitaxial Growth of Two-Dimensional Layered Transition-Metal Dichalcogenides: Growth Mechanism, Controllability, and Scalability. *Chem. Rev.* **2017**, *118*, 6134–6150.

277. Lan, C.; Li, C.; Yin, Y.; Liu, Y. Large-Area Synthesis of Monolayer WS_2 and Its Ambient-Sensitive Photo-Detecting Performance. *Nanoscale* **2015**, *7*, 5974–5980.

278. He, Z.; Sheng, Y.; Rong, Y.; Lee, G.-D.; Li, J.; Warner, J. H. Layer-Dependent Modulation of Tungsten Disulfide Photoluminescence by Lateral Electric Fields. *ACS Nano* **2015**, *9*, 2740–2748.

279. Fan, Y.; Zhou, Y.; Wang, X.; Tan, H.; Rong, Y.; Warner, J. H. Photoinduced Schottky Barrier Lowering in 2D Monolayer WS_2 Photodetectors. *Adv. Opt.*

Mater. **2016**, *4*, 1573–1581.

280. Chen, T.; Zhou, Y.; Sheng, Y.; Wang, X.; Zhou, S.; Warner, J. H. Hydrogen-Assisted Growth of Large-Area Continuous Films of MoS_2 on Monolayer Graphene. *ACS Appl. Mater. Interfaces* **2018**, *10*, 7304–7314.

281. Chang, R.-J.; Tan, H.; Wang, X.; Porter, B.; Chen, T.; Sheng, Y.; Zhou, Y.; Huang, H.; Bhaskaran, H.; Warner, J. H. High-Performance All 2D-Layered Tin Disulfide: Graphene Photodetecting Transistors with Thickness-Controlled Interface Dynamics. *ACS Appl. Mater. Interfaces* **2018**, *10* , 13002–13010.

282. Geim, A. Graphene: Status and Prospects. *Science* **2009**, *324*, 1530-1534.

283. Wang, S.; Rong, Y.; Fan, Y.; Pacios, M.; Bhaskaran, H.; He, K.; Warner, J. Shape Evolution of Monolayer MoS_2 Crystals Grown by Chemical Vapor Deposition. *Chem. Mater.* **2014**, *26*, 6371-6379.

284. Chang, Y.; Zhang, W.; Zhu, Y.; Han, Y.; Pu, J.; Chang, J.; Hsu, W.; Huang, J.; Hsu, C.; Chiu, M.; Takenobu, T.; Li, H.; Wu, C.; Chang, W.; Wee, A.; Li, L. Monolayer $MoSe_2$ Grown by Chemical Vapor Deposition for Fast Photodetection. *ACS Nano* **2014**, *8*, 8582-8590.

285. Zhao, W.; Ghorannevis, Z.; Chu, L.; Toh, M.; Kloc, C.; Tan, P.; Eda, G. Evolution of Electronic Structure in Atomically Thin Sheets of WS_2 and WSe_2. *ACS Nano* **2012**, *7*, 791-797.

286. Eichfeld, S.; Hossain, L.; Lin, Y.; Piasecki, A.; Kupp, B.; Birdwell, A.; Burke, R.; Lu, N.; Peng, X.; Li, J.; Azcatl, A.; McDonnell, S.; Wallace, R.; Kim, M.; Mayer,

T.; Redwing, J.; Robinson, J. Highly Scalable, Atomically Thin WSe_2 Grown via Metal–Organic Chemical Vapor Deposition. *ACS Nano* **2015**, *9*, 2080-2087.

287. Pandey, T.; Parker, D.; Lindsay, L. Ab initio Phonon Thermal Transport in Monolayer InSe, GaSe, GaS, and Alloys. *Nanotechnology* **2017**, *28*, 455706.

288. Mudd, G.; Svatek, S.; Ren, T.; Patanè, A.; Makarovsky, O.; Eaves, L.; Beton, P.; Kovalyuk, Z.; Lashkarev, G.; Kudrynskyi, Z.; Dmitriev, A. Tuning the Bandgap of Exfoliated InSe Nanosheets by Quantum Confinement. *Adv. Mater.* **2013**, *25*, 5714-5718.

289. Bandurin, D.; Tyurnina, A.; Yu, G.; Mishchenko, A.; Zólyomi, V.; Morozov, S.; Kumar, R.; Gorbachev, R.; Kudrynskyi, Z.; Pezzini, S.; Kovalyuk, Z.; Zeitler, U.; Novoselov, K.; Patanè, A.; Eaves, L.; Grigorieva, I.; Fal'ko, V.; Geim, A.; Cao, Y. High electron mobility, quantum Hall effect and Anomalous Optical Response in Atomically Thin InSe. *Nat. Nanotechnol* **2016**, *12*, 223-227.

290. Harvey, A.; Backes, C.; Gholamvand, Z.; Hanlon, D.; McAteer, D.; Nerl, H.; McGuire, E.; Seral-Ascaso, A.; Ramasse, Q.; McEvoy, N.; Winters, S.; Berner, N. C.; McCloskey, D.; Donegan, J. F,; Duesberg, G. S.; Nicolosi, V.; Coleman, J. N. Preparation of Gallium Sulfide Nanosheets by Liquid Exfoliation and Their Application as Hydrogen Evolution Catalysts. *Chem. Mater.* **2015**, *27*, 3483-3493.

291. Liu, L.; Feng, Y.; Shen, Z. Structural and Electronic Properties of h-BN. *Phys. Rev. B* **2003**, *68*. 104102

292. Song, L.; Ci, L.; Lu, H.; Sorokin, P.; Jin, C.; Ni, J.; Kvashnin, A.; Kvashnin, D.; Lou, J.; Yakobson, B. et al. Large Scale Growth and Characterization of Atomic Hexagonal Boron Nitride Layers. *Nano Lett.* **2010**, *10*, 3209-3215.

293. Zhang, C.; Park, S.; Ronan, O.; Harvey, A.; Seral-Ascaso, A.; Lin, Z.; McEvoy, N.; Boland, C.; Berner, N.; Duesberg, G. et al. Enabling Flexible Heterostructures for Li-Ion Battery Anodes Based on Nanotube and Liquid-Phase Exfoliated 2D Gallium Chalcogenide Nanosheet Colloidal Solutions. *Small* **2017**, *13*, 1701677.

294. Kim, Y.; Hone, J. Screen Printing of 2D Semiconductors. *Nature* **2017**, *544*, 167-168.

295. Meng, X.; Libera, J.; Fister, T.; Zhou, H.; Hedlund, J.; Fenter, P.; Elam, J. Atomic Layer Deposition of Gallium Sulfide Films Using Hexakis(Dimethylamido)Digallium and Hydrogen Sulfide. *Chem. Mater.* **2014**, *26*, 1029-1039.

296. Jung, C.; Shojaei, F.; Park, K.; Oh, J.; Im, H.; Jang, D.; Park, J.; Kang, H. Red-To-Ultraviolet Emission Tuning of Two-Dimensional Gallium Sulfide/Selenide. *ACS Nano* **2015**, *9*, 9585-9593.

297. Rashkeev, S.; Fleetwood, D.; Schrimpf, R.; Pantelides, S. Defect Generation by Hydrogen at The Si-SiO_2 Interface. *Phys. Rev. Lett.* **2001**, *87,* 165506.

298. Wimmer, Y.; El-Sayed, A.; Gös, W.; Grasser, T.; Shluger, A. Role Of Hydrogen in Volatile Behaviour Of Defects in SiO_2-Based Electronic Devices. *Proc. Royal Soc. A* **2016**, *472*, 20160009.

299. Conley, J.; Lenahan, P. Room Temperature Reactions Involving Silicon Dangling Bond Centers and Molecular Hydrogen in Amorphous SiO_2 thin Films on Silicon. *Appl. Phys. Lett.* **1993**, *62*, 40-42.

300. Wu, Z.; Ren, W.; Gao, L.; Zhao, J.; Chen, Z.; Liu, B.; Tang, D.; Yu, B.; Jiang, C.; Cheng, H. Synthesis of Graphene Sheets With High Electrical Conductivity and Good Thermal Stability by Hydrogen Arc Discharge Exfoliation. *ACS Nano* **2009**, *3*, 411-417.

301. Youn, D.; Han, S.; Kim, J.; Kim, J.; Park, H.; Choi, S.; Lee, J. Highly Active and Stable Hydrogen Evolution Electrocatalysts Based on Molybdenum Compounds on Carbon Nanotube–Graphene Hybrid Support. *ACS Nano* **2014**, *8*, 5164-5173.

302. Ibragimov, T.; Kurbanova, G.; Gorelik, V. Raman Scattering in Gallium Selenide and Sulfide Films. *Phys. Status Solidi B* **1989**, *155*, 113-116.

303. Freitag, M.; Martin, Y.; Misewich, J.; Martel, R.; Avouris, P. Photoconductivity of Single Carbon Nanotubes. *Nano Lett.* **2003**, *3*, 1067-1071.

304. Zhou, H.; Wang, C.; Shaw, J.; Cheng, R.; Chen, Y.; Huang, X.; Liu, Y.; Weiss, N.; Lin, Z.; Huang, Y. et al. Large Area Growth and Electrical Properties of P-Type WSe_2 Atomic Layers. *Nano Lett.* **2014**, *15*, 709-713.